Vetle Runestad Østerhus

Improving Quantification of Sigma and Chi Phases in SDSS with EBSD

June 2020

Master's thesis

Master's thesis

2020

Vetle Runestad Østerhus

NTNU
Norwegian University of
Science and Technology

NTNU
Norwegian University of
Science and Technology

NTNU
**Norwegian University of
Science and Technology**

Improving Quantification of Sigma and Chi Phases in SDSS with EBSD

Vetle Runestad Østerhus

Preface

The present thesis and experimental work are submitted to the Norwegian University of Science and Technology (NTNU), Department of Materials Science and Engineering (IMA) and is a part of TMT4505 Materials Technology, Master's Thesis. This thesis is a direct continuation of a project done in Fall 2019, and some parts have been reused. The thesis is conducted according to the regulations for the completion of a Master's thesis at NTNU. The author hopes that the work presented will contribute to the field of materials science.

15 June 2020
Trondheim, Norway
Vetle Runestad Østerhus

Abstract

Super duplex stainless steels (SDSS) are due to their combination of high corrosion resistance and good mechanical properties used in industries where these material properties are needed, e.g. in the oil and gas industry. A problem with SDSS is their susceptibility to formation of intermetallic sigma (σ) and chi (χ)-phase at elevated temperatures. The formation leads to reduced mechanical properties and lower corrosion resistance for the material. A way to characterize the intermetallic phases is by using a scanning electron microscope (SEM), where electron backscatter diffraction (EBSD) is an often used technique for studying crystallographic microstructures. The well established Hough indexing (HI) approach is frequently used for EBSD pattern indexing. However, HI often face problems when indexing EBSD patterns from σ and χ-phase regions due to low pattern quality. The newer dictionary indexing (DI) approach has proven itself capable of obtaining enhanced results when compared to HI. When indexing using the DI approach, dictionary patterns for a phase is matched against the experimental EBSD patterns of a data set. The dictionary patterns are simulated using a physics-based forward model.

In the specialization project this thesis is a continuation of, DI was proven to give better results compared to HI. This was the case both when indexing EBSD data sets containing ferrite (α) and austenite (γ)-phases, and α, γ and σ-phases. However, when including χ-phase in the DI, mis-indexing of χ was occurring. However, testing of multiple EBSD pattern processing recipes for DI was not performed. Therefore, the main motivation for this thesis was to optimize the processing parameters for the indexing of all present phases. The aim was to find a pattern processing recipe causing a lower mis-indexing rate. Also, new samples were studied and the EBSD results were compared to backscatter electron images (BEI) and Electron Probe Micro Analysis (EPMA) X-ray maps.

By changing the EBSD pattern processing recipe for DI, a more optimal processing was found. In addition to a preceding static and dynamic background subtraction, a processing using a gaussian high-pass filtering of low impact (high-pass filtering parameter $w = 1/8$) and an adaptive histogram equalization (AHE) of four tiles (AHE number of regions parameter $n = 2$) was considered to cause the least amount of mis-indexing. The pattern processing reduced the mis-indexing of χ-phase significantly, but was still capable of index the α, γ, σ and χ-phases correct. The EBSD results were in general in agreement with the obtained results of BEI and EPMA. For DI, when performing testing regarding the dynamic background subtraction, the high-pass filtering and the AHE processing steps, tuning the AHE was causing the largest differences in the obtained results. A mild AHE processing was giving the best results. An AHE of too many tiles gave poorer results as the χ-phase got favored over the other three phases.

Sammendrag

Super duplex rustfrie stål (SDSS) blir på grunn av deres kombinasjon av høy korrosjonsmotstand og gode mekaniske egenskaper brukt i industrier hvor disse materialegenskapene er nødvendige, f.eks. i olje- og gassindustrien. Et problem med SDSS er formasjon av intermetallisk sigma (σ)- og chi (χ)-fase ved økte temperaturer. Fasetransformasjonen fører til svekkede mekaniske egenskaper og forringet korrosjonsmotstand hos materialet. En måte å karakterisere de intermetalliske fasene på er ved bruk av scanning-elektron-mikroskop (SEM), hvor «electron backscatter diffraction» (EBSD) er en hyppig brukt teknikk for å studere krystallografiske mikrostrukturer. Den veletablerte Hough-indekseringsteknikken (HI) er ofte brukt for EBSD-mønsterindeksering. Problemet til HI er at teknikken ofte støter på problemer når EBSD-mønstre fra σ- og χ-faseregioner skal indekseres grunnet lav møsnterkvalitet hos disse fasene. Den nyere «dictionary»-indekseringsteknikken (DI) har vist seg å være i stand til å oppnå forbedrede resultater sammenlignet til HI. Når man indekserer ved bruk av DI blir «dictionary»-mønstre for en gitt fase sammenlignet mot de eksperimentelle EBSD-mønstrene i et datasett. «dictionary»-mønstrene blir simulert ved bruk av en «physics-based forward»-modell.

I spesialiseringsprosjektet denne oppgaven er en videreførelse av, ble det vist at DI ga bedre resultater sammenlignet til HI. Dette var tilfelle både da indeksering av EBSD-datasett som inneholdt ferritt (α)- og austenitt (γ)-fasene ble testet, samt datasett som inneholdt α-, γ- og σ-fasene. Problemer oppstod derimot da χ-fasen skulle inkluderes i DI-teknikken, ettersom feilindeksering av χ-fase fant sted. Til tross for dette ble ikke flere enn en EBSD-mønsterprosesseringsoppskrift testet ut for DI. Av den grunn var hovedmotivasjonen bak denne oppgaven å optimalisere prosesseringsparameterne for indeksering av alle tilstedeværende faser. Målet var å finne en mønsterprosesseringsoppskrift som ville føre til en lav feilindekseringsrate. Nye prøver ble også studert og EBSD-resultatene ble sammenlignet mot «backscatter electron»-bilder (BEI) og «Electron Probe Micro Analysis» (EPMA)-røntgenkart.

Ved å endre på EBSD-mønsterprosesseringsoppskriften for DI ble en mer optimal prosessering funnet. I tillegg til en forløpende statisk- og dynamisk bakgrunnsubtraksjon ble en prosessering hvor en lav-korreksjons gaussisk «high-pass»-filtrering («high-pass»-filtreringsparameter $w = 1/8$) og en «adaptive histogram equalization» (AHE) med fire ruter (AHE tallparameter $n = 2$) brukt. Denne prosesseringsoppskriften ble vurdert som den som ga minst feilindeksering. Den ga en signifikant reduksjon i feilindeksert χ-fase, men var likevel i stand til å indeksere α-, γ-, σ- og χ-fasene rett. EBSD-resultatene var på generell basis ikke i strid med resultatene fra BEI og EPMA. Da testing knyttet til den dynamiske bakgrunnsubtraksjonen, «high-pass»-filtreringen og AHE-prosesseringen ble utført for DI, førte justeringer knyttet til AHE til størst endringer i resultatene. En mild AHE-prosessering ga de beste resultatene. En AHE med for stor ruteoppdeling ga dårligere resultater siden χ-fasen ble favorisert over de andre tre fasene.

Abbreviations

Abbreviation	Explanation
AHE	Adaptive Histogram Equalization
AM	Additive Manufacturing
BCC	Body Centered Cubic
BEI	Backscatter Electron Image
CI	Confidence Index
DI	Dictionary Indexing
DP	Dot Product
EBSD	Electron Backscatter Diffraction
EBSP	Electron Backscatter Diffraction Pattern
EPMA	Electron Probe Micro Analysis
FCC	Face Centered Cubic
FG	Fine Grinding
GMAW	Gas Metal Arc Welding
HAZ	Heat Affected Zone
HI	Hough Indexing
IPF	Inverse Pole Figure
IQ	Image Quality
MIG	Metal Inert Gas (welding)
OSM	Orientation Similarity Map
P	Polishing Step
PG	Plane Grinding
PM	Phase Map
PREN	Pitting Resistance Equivalent Number
SDSS	Super Duplex Stainless Steel
SEM	Scanning Electron Microscope
TCP	Topologically Close-Packed
TTT	Time Temperature Transformation (diagram)
WAAM	Wire Arc Additive Manufacturing

Abbreviations used for DI pattern processing recipes	
S	Static Background Subtraction
D	Dynamic Background Subtraction
H	High-pass Filtering
A	Adaptive Histogram Equalization
G	Gamma Correction

Symbols

Symbol	Explanation
α	Ferrite phase
γ	Austenite phase
η	Near match similarity index
σ	Sigma phase
χ	Chi phase
B_{iso}	Debye-Waller factor
DP	Dot product value
f	Site occupation parameter
n	Adaptive histogram equalization number of regions parameter
w	High-pass filtering parameter

Contents

1   Introduction

Super duplex stainless steels (SDSS) are widely used in e.g. chemical and petrochemical industries, and in offshore constructions since they posses both good corrosion resistance and mechanical properties. The excellent properties are achieved by adding high amounts of allying elements to the steels. However, these amounts make SDSS susceptible to embrittlement when heat treated at elevated temperatures ($325 - 900\,$°C). Causes leading to the embrittlement are e.g. formation of intermetallic σ and χ-phases. [1, 2]

A way to characterize and quantify the intermetallic phases formed is with Electron Backscatter Diffraction (EBSD) in the Scanning Electron Microscope (SEM). EBSD is suitable for crystallograpic analysis, e.g. determination of orientation of individual grains, phase identification and characterization of grain boundaries [3]. In addition to the well established and conventional Hough-based indexing (HI) approach, the newer dictionary indexing (DI) approach provides a powerful alternative to HI. The DI approach is capable of getting enhanced results compared to HI, especially for EBSD patterns which are of poor quality [4]. Previous studies show that the intermetallic σ- and χ-phases often have poor pattern quality and therefore are problematic to index correctly using the Hough-based approach [5–7].

The aim of this thesis is to successfully index the four phases α, γ, σ and χ for EBSD pattern files from SDSS samples using the dictionary indexing approach. Only a partial success toward this goal was achieved in the specialization project this thesis is a continuation of [8]. Studying the effect of making changes to the pattern processing recipe for DI, in order to potentially find a more suitable processing, is therefore performed. In order to verify the results, the EBSD results are also compared to backscatter electron images and EPMA X-ray maps of the same samples.

In section 2, theory covering e.g. SDSS, intermetallic phases, the HI and DI approaches and EBSD pattern processing is included. In section 3, information about the sample preparation and parameters used for the characterization techniques is presented. Required information in how the HI and DI approaches are performed is also included. In section 4, the results from the pattern processing recipe tuning for DI and results from all characterization techniques used are presented. These topics are further discussed in section 5. A summary of the most central findings are given in section 6. Proposals to further work of study are presented in section 7. In the appendix a more in-depth guide in performing the EMsoft dictionary indexing is given.

2   Theory

In this chapter is relevant theory presented. Theory about additive manufacturing, duplex stainless steels and the secondary phases sigma (σ), chi (χ) and chromium nitrides is presented. In addition is an introduction to scanning electron microscopy (SEM) and electron backscatter diffraction (EBSD) given. The two EBSD pattern indexing approaches, Hough indexing and dictionary indexing are also covered. In the end is theory about the used EBSD pattern processing steps given.

2.1   Additive Manufacturing

Additive manufacturing (AM), originally called 3D-printing, is currently one of the engineering topics of high interest for its promising scientific and industrial results over the last decade. In AM parts or structures are assembled by adding material layer upon layer. For metals the process can be considered as a welding technique, where the structure is created by adding molten filler metal layer by layer in the vertical direction. However, for AM to be used in larger scale in the industry, e.g. in the oil and gas industry, more research is needed. AM still needs reliable commercial acceptability to compete with other manufacturing processes. Despite still having its challenges, AM has multiple advantages. One of them is the freedom of design AM provides. Compared to casting methods, the layer by layer deposition allows production of customized engineering components directly from the design. The final part can also be built in one piece, which reduces the production time compared to other production methods. Reduction of waste is also possible compared to commercial production methods being used today [9–11].

Various welding techniques may be used for additive manufacturing of metal parts. One approach is the use of metal powder and a laser or an electron beam as the heat source. By using AM with metal powder, complex shapes and even hollow parts may be produced. However, the drawbacks are the high cost of powder and the low build-up rate. In other words do the economic factors limits the maximum achievable size and thickness of this technique. An other welding method applied for AM is the use of a wire as the additive material and an electric arc as the heat source. This describes the method called wire arc additive manufacturing (WAAM). An arc welding technique used for WAAM is the gas metal arc welding (GMAW) process, also called metal inert gas (MIG) welding. WAAM has a high deposition rate, which makes it possible to produce large scale parts in reasonable time. With deposition rates ranging from 1kg/h to 4kg/h for aluminium and steel, most parts can be manufactured within a single working day [9–12].

2.2   Duplex Stainless Steel (DSS)

Normal carbon steels possess favorable mechanical properties when still being inexpensive. This makes carbon steels attractive materials. However, plain-carbon steels have poor corrosion resistance, and further protection are for many applications necessary. A method available is to alloy the steel with Cr. When the Cr level in steels exceeds ~10.5 wt.%, Cr protects the steel by forming a passive layer, which leads to reduced corrosion rates [13, 14]. Stainless steels are further classified into four groups, based on composition and crystal structure: ferritic, austenitic, martensitic and duplex stainless steels [13]. Duplex stainless steels consists of a two phase structure of ferrite and austenite, where at least 25-30% of the lesser phase is present [1]. This structure is achieved by adding various phase stabilizing elements. In DSS, ferrite has good corrosion resistance, while austenite improves the mechanical properties. The result is a favorable combination between corrosion resistance and mechanical properties [13].

2.2.1   Microstructure

As previously mentioned, Duplex Stainless Steels consists of a balance between ferrite and austenite which gives good corrosion resistance, and a high yield strength and toughness in the wide temperature range between -50 °C and 250 °C [15]. Ferrite has the Body Centered Cubic (BCC) lattice structure and austenite has the Face Centered Cubic (FCC) lattice structure. The content of each phase should be close to 50% in order to obtaining the combined phase benefits for the current material [16].

The ternary phase diagram for Fe-Cr-Ni is important in understanding the metallurgical behavior of duplex stainless steels. A section of the ternary phase diagram is shown in Figure 2.1 [17]. The evolution of the duplex structure from the melt can be described by equation (1) [2, 17]:

$$L \rightarrow L + \alpha \rightarrow \alpha \rightarrow \alpha + \gamma_2 \tag{1}$$

, where L is the liquid phase, α is ferrite and γ_2 is secondary austenite. In Table 2.1 is the difference between primary, secondary and tertiary austenite explained [2].

Table 2.1: Types of austenite formation in duplex steels [2]

γ type	Formation mechanism	Reaction
Primary	Formation from liquid phase	$L \rightarrow \alpha + \gamma_1$
Secondary	Solid state transformation from ferrite	$\alpha \rightarrow \gamma_2$
Tertiary	Eutectoid transformation of ferrite	$\alpha \rightarrow \gamma_3 + \sigma$

When cooling from the melt, the alloy first precipitates as α. Some of the α is by further cooling transformed into γ_2. γ_2 first precipitates at the grain boundaries of α, and further growth follows favorable crystallographic orientations inside the α-grains. By controlling

the cooling, a microstructure of 50-50 ferrite and austenite can be achieved [13, 17]. The structure may be described as a matrix of ferrite containing austenite islands [16].
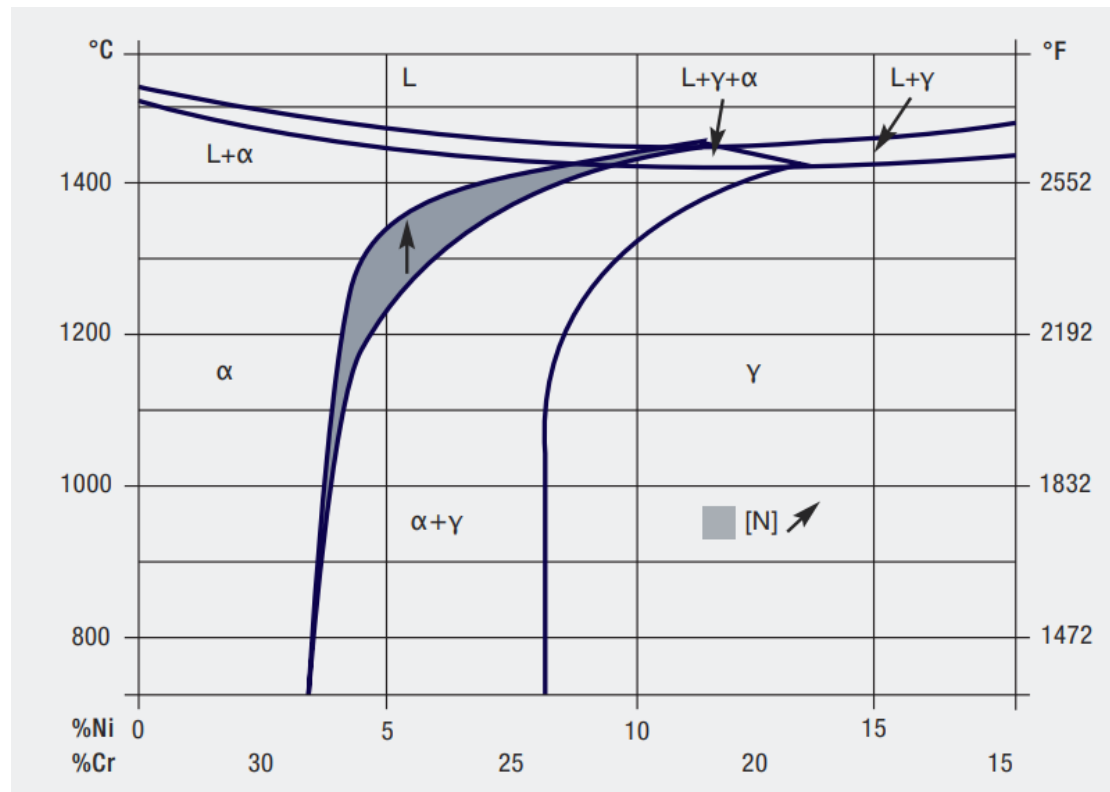
Figure 2.1: Pseudo-binary section through the Fe-Cr-Ni ternary phase diagram at 68% iron. The shaded area containing a labeled arrow indicates qualitatively how an increase in the N composition affects the phase boundary $\alpha/(\alpha + \gamma)$ [17]

2.2.2   Alloying Elements

The most important alloying elements in duplex stainless steels are chromium, molybdenum, nickel and nitrogen. Cr and Mo are ferrite stabilizers while Ni and N are austenite stabilizers. Cr is necessary when forming the passive film, which protects against atmospheric corrosion. Cr also increase the oxidizing resistance at elevated temperatures. A Cr content of at least 20% is needed in duplex steels. Mo is added to increase the pitting corrosion resistance of duplex steels. Duplex stainless steels are usually restricted in containing a maximum of 4% Mo since the element promote formation of intermetallic phases (see section 2.3). N additions increase the pitting and crevice corrosion resistance of duplex steels. N also has the function of being a solid solution strengthener. Since N is a low cost alloying element, and both N and Ni are austenite stabilizers, N can be added to replace some of the more-expensive Ni. Both N and Ni have the effect of delaying the formation of intermetallic phases. N is suprisingly reported to reduce the risk of nitride formation. The explanation is the reduced austenite island spacing as the austenite fraction increases with increasing N content. It also suppresses austenite

dissolution and promotes austenite reformation in the HAZ. These effects also suppress chromium nitride formation (see section 2.3.3). Mn, which is a third austenite stabilizer, can also be added to replace some Ni. However, in DSS mixed results have been obtained when using Mn as a austenite stabilizer. The current understanding is that Mn has a low effect on the ferrite-austenite balance. However, Mn additions have the effect of increased abrasion and wear resistance. The tensile properties are also increased without loss of ductility. The Ni content in duplex stainless steels is normally in the range from 1.5 to 7%. Excessive Ni contents should be avoided as it increase the fraction of austenite phase well above 50 %. This leads to a ferrite enriched in Cr and Mo which enhance the formation of intermetallic phases. Cu may be added for improved corrosion resistance in non-oxidizing solutions. However, the Cu content should be kept below ∼2.5% in order to prevent reduced hot ductility [17–19]. Some duplex steels also contains tungsten additions up to 2 %. W has the effect of increasing the pitting and crevice corrosion resistance. W has its drawback of promoting the intermetallic phase formation in the 700-1000°C temperature range [19]. The carbon content in DSS is usually kept very low ($< 0.03\%$), and for that reason the harmful effects of carbides are normally not present in DSS [13, 17].

Pitting corrosion resistance of duplex steels may be evaluated by the pitting resistance equivalent number (PREN), given by

$$PREN = \%Cr + 3.3\%Mo + k\%N, \tag{2}$$

where $k = 16 - 30$ [20]. The PREN number can be used to classify the DSS into the following four categories: lean duplex (25-26), standard duplex (35-36), super duplex (40-42) and hyper duplex (>45). The higher PREN value, the better pitting corrosion resistance. However, PREN does not consider the influence of phase morphology and microstructure inhomogenity. PREN is therefore not suitable in the precise definition of the pitting resistance of a heat-treated DSS [13, 21]. Due to the increased alloy element contents in super duplex stainless steels, these alloys also exhibit higher strength than the standard duplex alloys [15].

2.3   Secondary Phases in DSS

When duplex steels are subject to temperatures in the range $300 - 900$ °C, various phase transformations may occur in the material. These phase transformations are normally unwanted since they typically cause embrittlement and loss of corrosion resistance. Causes behind the reduced duplex steel properties are formation of intermetallic sigma (σ) and chi (χ) phases, precipitation of nitrides (Cr_2N) and spinodal decomposition (formation of α') [1, 2, 21]. The time-temperature-transformation diagram (TTT-diagram) for UNS S31803 duplex stainless steel is shown in Figure 2.2. It displays at what temperature and at which holding durations the phase transformations typically occur in duplex steels [22].
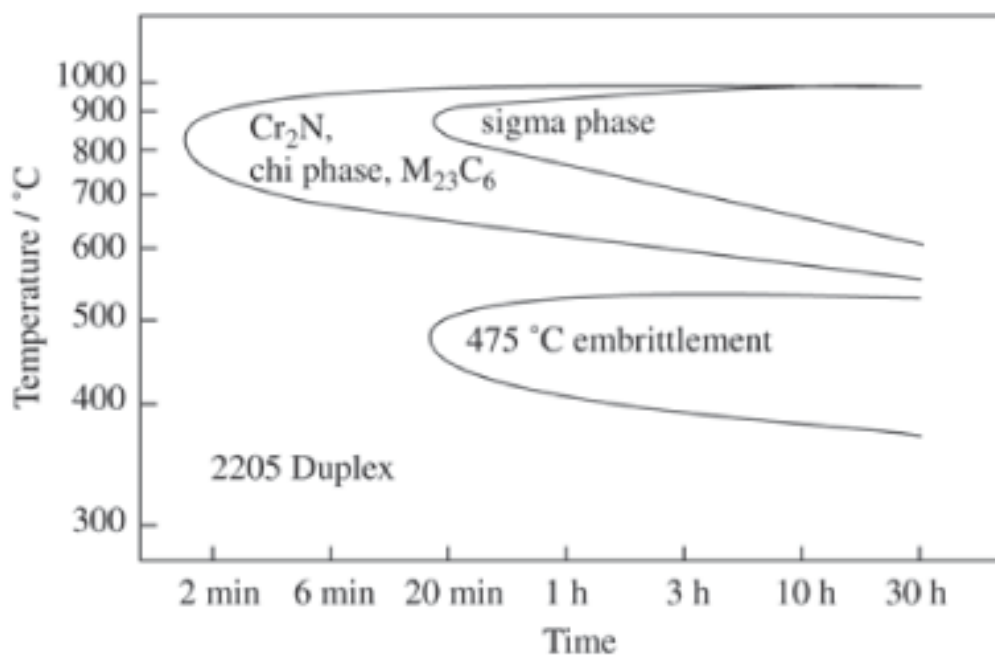
Figure 2.2: TTT-diagram fo UNS S31803 Duplex Stainless Steel [22]

2.3.1   Sigma Phase (σ)

The σ phase has a tetragonal crystal structure with 32 atoms per unit cell [23]. The phase contains about 30% Cr, 4% Ni and 7% Mo [18]. The phase is a thermodynamic stable phase which has its origin from Fe-Cr system. In the pseudo-binary phase diagram of Fe–Cr–Ni, shown in Figure 2.3, the σ phase forms on the Cr rich side of the diagram.

The σ phase is typically formed in the temperature range $600 - 1000$ °C, where α is transformed into σ and γ_3, given by equation (3) [2].

$$\alpha \rightarrow \gamma_3 + \sigma \tag{3}$$
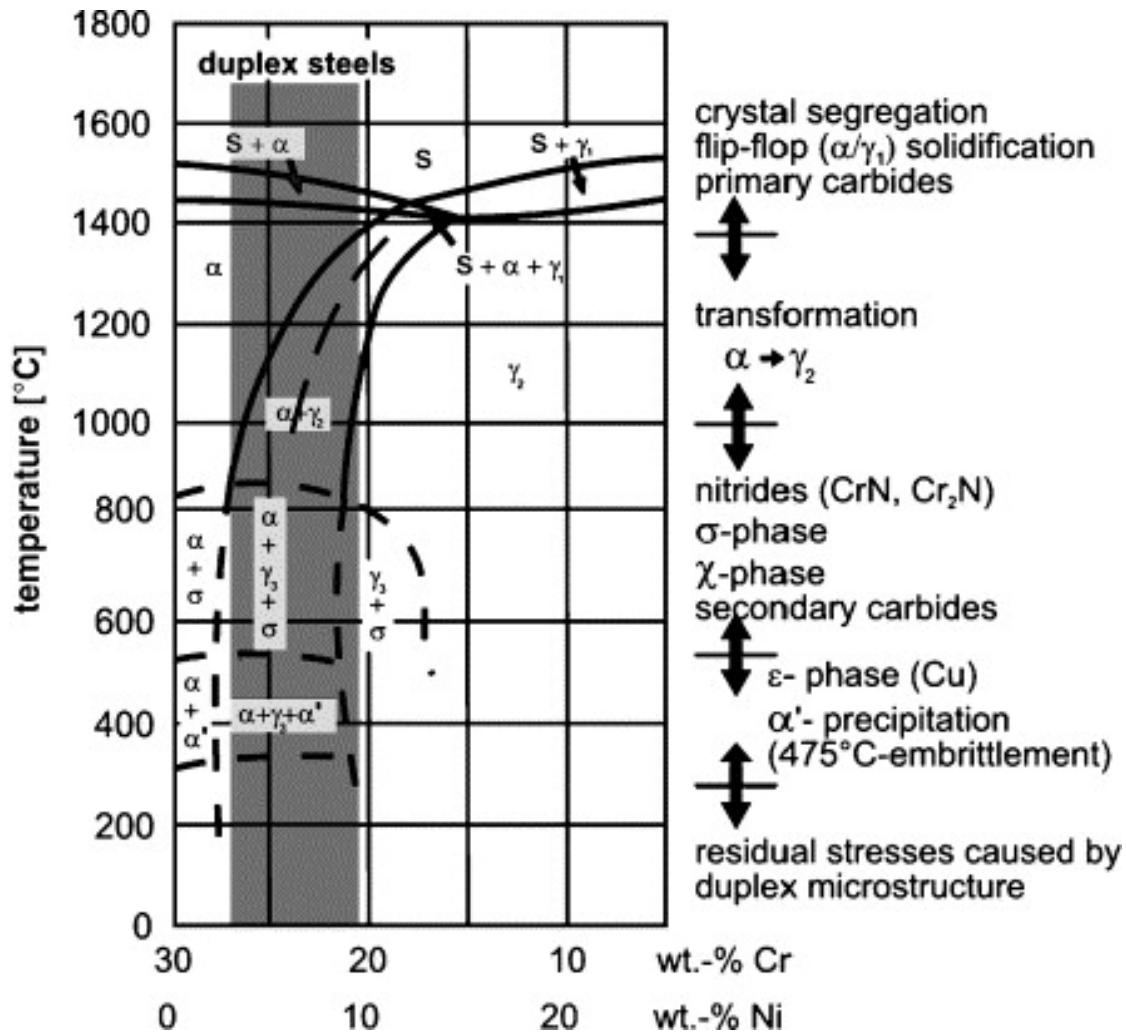
Figure 2.3: Pseudo-binary section through the Fe-Cr-Ni ternary phase diagram at 70% iron. The typical duplex steel composition range is shaded in the diagram. On the right side various precipitation zones are labeled in accordance to their temperature range where they may occur in duplex steels [2]

Sigma phase preferably nucleates at the $\alpha - \alpha$ and $\alpha - \gamma$ grain boundaries. The further growth occurs in the adjacent α grains. Cr, Mo and Si, which all are ferrite stabilizers, also promote the σ phase formation. As the growth of σ phase occurs, Mo and Cr in the α phase diffuse to the σ phase and deplete α for these elements. α, which also has some amounts of dissolved γ-stabilizers will, due to the loss of ferrite stabilizers become unstable and is transformed into γ_3 [18]. Since the remaining α phase and newly formed γ_3 is depleted for Cr and Mo, the corrosion resistance of these phases is reduced [21].

2.3.2   Chi Phase (χ)

The χ-phase has been less studied than the σ-phase [24]. Some sources claim it has a topologically close-packed (TCP) crystal structure [23] while other references give it a BCC crystal structure [18]. However, a much more detailed description of the χ structure

was given by Kasper (1954) [25], which is used as reference for the chi crystal structure file in this thesis. Beside Fe the χ phase contains about 25% Cr, 3% Ni and 14% Mo. χ forms at $700 - 900$ °C, but it is metastable and will after prolonged aging transform into σ [18]. χ-phase precipitates at the α/α-grain boundary and is formed at lower temperature and in smaller amounts than σ-phase [24]. According to Kleppen (2018) [26] is it also possible for χ to precipitate inside the grains of the material, probably at heterogeneous positions. χ- and σ-phase often coexist. This make it in many cases challenging to study their individual impact on duplex steels [23].

2.3.3 Chromium Nitrides, Cr_2N & CrN

As previous mentioned, nitrogen is important in duplex stainless steels for stabilizing the austenite and to achieve preferred ferrite-austenite ratios. During welding the HAZ typically undergoes ferritization, due to the elevated temperature it is exposed to. When the austenite dissolves the ferrite also dissolves the nitrogen present in austenite. Ferrite has a low solubility of nitrogen at lower temperatures and the nitrogen is mainly present in austenite. By slow cooling austenite will be reformed from ferrite and lowers the N fraction in ferrite. However, if the HAZ undergoes rapid cooling after welding, the formation of austenite is suppressed. This suppression leads to a ferrite supersaturated in nitrogen, and chromium nitrides may be formed instead of austenite. If austenite or chromium nitride is formed, is a function of the chemical composition, cooling rate and ferrite grain size [27, 28].

Two types of chromium nitrides are found in SDSS, Cr_2N and CrN. They nucleates at dislocations, inclusions and grain boundaries (both α/α and α/γ boundaries) [28]. Cr_2N forms rod-shaped particles and which have a trigonal crystal structure with space group P$\bar{3}$1m. CrN is observed to form film-like regions and has a cubic crystal structure with space group Fm$\bar{3}$m [27, 29]. For high cooling rates both CrN and Cr_2N are observed to be formed, but for lower cooling rates only Cr_2N is seen. As example, in Pettersson et al. (2015) [27] a plate material of super duplex alloy UNS S32750 was heated at 1250 °C and cooled both with 50 and 100 °C/s using a dilatometer. For the cooling rate of 100 °C/s, Cr_2N and CrN were observed to coexist. For the sample cooled using 50 °C/s only Cr_2N was found. A rapid cooling also lead to a higher Cr_2N fraction and larger particles. Further thermodynamic calculations in the study predict Cr_2N to be the only thermodynamic stable nitride phase out of the two [27].

In Pettersson et al. (2015) [27] it is not measured any reduction in toughness in the samples where Cr_2N was formed. Only an air cooled sample, where sigma phase instead of nitrides was formed had a reduction in toughness. However, in Hereñú et al. (2014) [30] Cr_2N is reported to have a detrimental effect on the low-cycle fatigue life when formed in duplex steels. Formation of Cr_2N may also reduce the corrosion resistance in duplex steels as it depletes the surrounding material for Cr and N. Only a small reduction in the pitting corrosion resistance was measured in Pettersson et al. (2015)

[27] in the samples where Cr_2N was formed. However, larger Cr_2N-particles are argued for having a more significant effect on the pitting corrosion resistance compared to the smaller particles [27].

2.4   Scanning Electron Microscopy (SEM)

Scanning electron microscopes (SEM) are important instruments in material characterization. The instrument may be used for characterization of heterogeneous materials and -surfaces on micro scale. In the SEM a thin electron beam is created and focused onto the surface of the specimen which is analysed. When the electron beam hits the specimen, various signals are created, e.g. secondary electrons, backscattered electrons and characteristic X-rays (see Figure 2.4). The signals can amongst other things give information about the topography, phase composition and crystallography of the specimen [31].
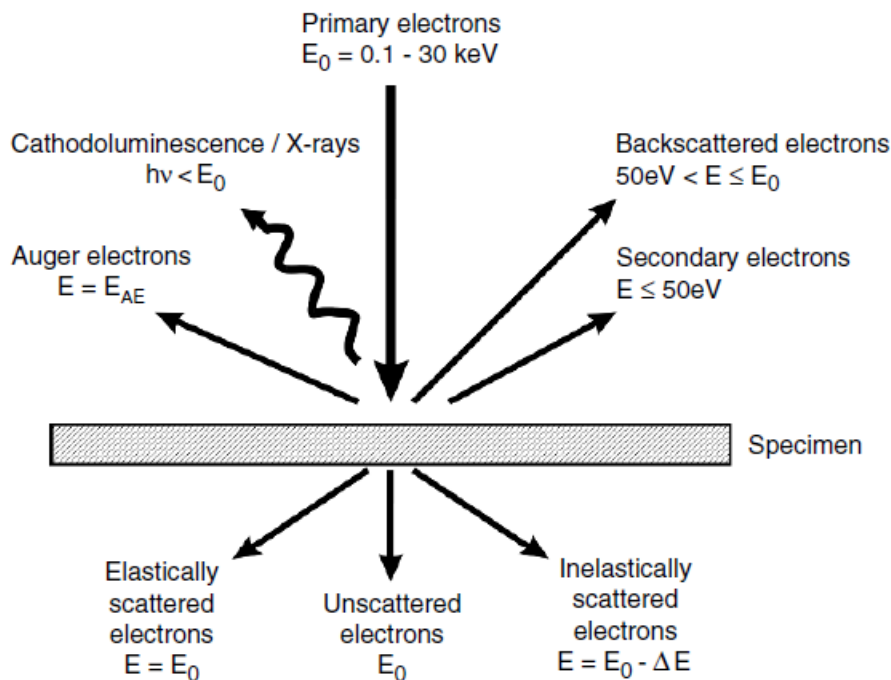
Figure 2.4: Different signals created in SEM [32]

Among the most important parts in an SEM are the electron gun, electron lenses (objective and condenser lenses), apertures and detectors. The electron gun further consists of an anode, a cathode and a Wehnelt cylinder. The gun produces a steady flow of electrons. The condenser lens determines the final electron current which interact with the specimen, while the objective lens determine the electron beam cross section [31, 32]. The acceleration voltage used for SEM microscopy is between 0.5 and 30 kV. A resolution of $0.5 - 1.0$ nm may be achieved in a modern instrument [32].

2.5   Electron Backscatter Diffraction (EBSD)

Electron backscatter diffraction (EBSD) is an characterization technique available in combination with an SEM, which make use of backscattered electrons in the analysis of the examined sample. It may be used to give information of grain orientation, local texture, and phase identification and -distribution on the surface of a sample. The typical setup of the electron source, sample and EBSD detector is shown in Figure 2.5. When running EBSD pattern acquisition of a sample, a high energy electron beam is pointed at the surface of the sample. The primary electrons will penetrate into the surface of the specimen and diffraction may occur in the lattice planes for electrons which fulfills Bragg's law:

$$2d\sin\theta = n\lambda, \tag{4}$$

where d is the lattice plane spacing, θ is the Bragg angle, n is the order of reflection and λ is the wavelength of the electrons in the beam. The sample is normally tilted to approximately 70° relative to the electron gun. This increase the amount of backscattered electrons which leave the sample [3].
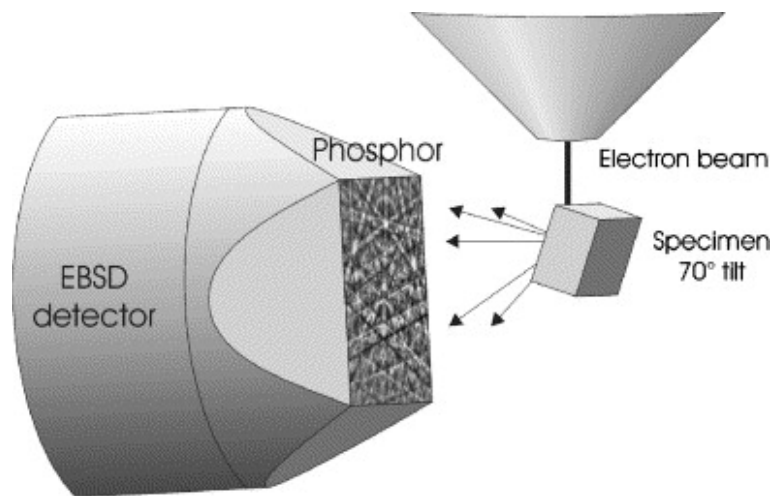
Figure 2.5: Schematic of the EBSD setup [33]

Upon leaving the sample the backscattered electrons are intended to hit the detector, which is positioned close to the sample. The detector has a flat phosphor screen on its surface. The backscattered electrons give rise to multiple bright bands on the otherwise dark background on the screen. The bands are called Kikuchi bands, and the total pattern is called a Kikuchi pattern, also called an EBSD Pattern (EBSP). A Kikuchi band can be interpreted as a projection of a crystal lattice plane onto the phosphor screen. The center of the Kikuchi band represent the lattice plane and the band width is a result of scattering of the backscattered electrons about a small angle. The width of the bands are proportional to twice the value of the Bragg angle. The angle between two Kikuchi

bands corresponds to the interplanar angle of the crystallographic planes the bands origin from. The geometry of a Kikuchi pattern is dependent on the crystal structure and the crystal lattice orientation of the examined crystal. The Kikuchi patteren can therefore be used to determine which phase the pattern is origin from and which orientation the examined sample point has, if theoretical information about the bands and patterns already is available [3, 34].

2.6 Hough Indexing (HI)

Indexing of EBSP by using the Hough transform, Hough Indexing (HI), is well understood and widely implemented by various vendors in commercial EBSD packages [4]. In Figure 2.6 is the Hough transform illustrated. When applying HI the Hough transform reduce the problem of locating Kikuchi bands in the pattern to locating individual points in Hough space. A line in the diffraction pattern may be characterized by a (ρ, θ) coordinate in the Hough space. Here ρ is the normal going from the line to a defined origin in the diffraction pattern. θ is the angle between the x-axis and ρ. When the Hough transform of a line is calculated, multiple points on the line are examined. For each point all possible ρ-values for θ ranging from 0 to 180° are calculated. This produce a sinusoidal curve for each examined point when ρ is plotted against θ. The curves will intersect at a point (ρ_l, θ_l) which corresponds to the ρ and θ values of the line [3, 35]. When the band normals are determined, the angle between the bands can further be found. The angles are compared to a pre-computed list of angles based on known sample crystallography. This results in the indexing of individual bands and subsequently, the determination of the orientation of the crystal lattice and which phase the pattern matches [4].
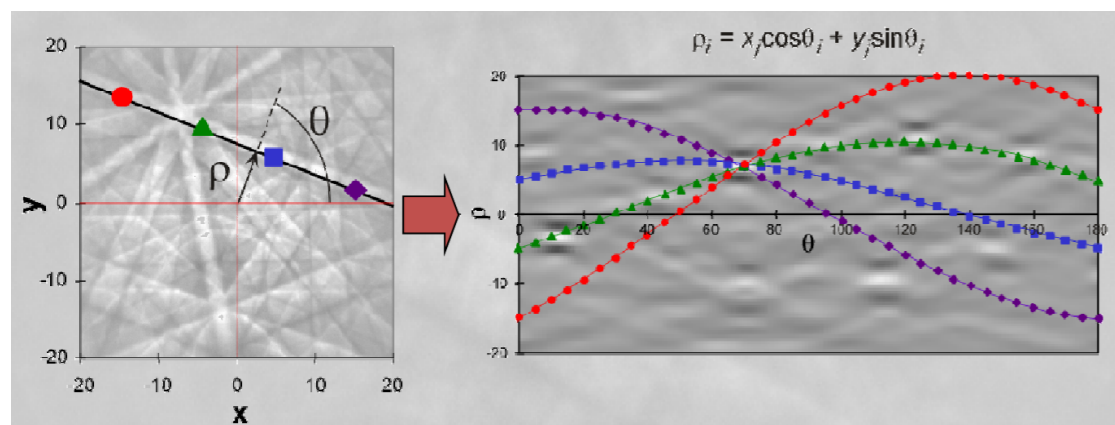

Figure 2.6: The Hough transform approach of a Kikuchi band illustrated [35]

2.7 Dictionary Indexing (DI)

A newer indexing approach which still is in development is dictionary indexing (DI). In DI the entire pattern of a phase is simulated by the use of a physics-based forward model. This simulated pattern is called the *master pattern* of the phase. When running dictionary indexing sections of the master pattern, called dictionary patterns, are compared to the experimental pattern. The patterns may be represented as vectors and the vector dot product is used to rank the dictionary patterns by how good match they have to the experimental pattern. The vectors must be normalized, and the dot product each dictionary pattern receives is then in the range [-1, 1]. The formula used for calculating the dot product, also called the normalized inner product is given by equation (5) [36]:

$$\rho(Y, \phi_i) = \frac{(Y, \phi_i)}{||Y|| \, ||\phi_i||},\tag{5}$$

, where ρ is the dot product, Y is the experimental EBSD pattern and ϕ_i is a dictionary element. Depending on the settings used when generating the master pattern file, multiple master patterns are generated, each for an unique energy interval. The energy intervals are called energy bins and are set by the user. The number of energy bins required is determined by the upper and lower backscatter electron energy, set by the user when creating the master pattern file [4]. The master pattern of an energy bin may be visualized as an image, which makes it possible to study them.

Compared to the HI approach, DI is less affected by noise in the EBSP. DI will therefore better handle rapidly acquired low-quality patterns as well as patterns from structures with more diffuse EBSPs. In practice is the DI approach's accuracy only limited by the precision in determining the detector geometry [4]. However, DI has its drawback in being much more time consuming to run compared to HI.

2.7.1 EMsoft

EMsoft is the software used for dictionary indexing, which is among other developed by Marc De Graef, who is one of the developer of the dictionary indexing approach. EMsoft is a package for simulation of electron microscopy imaging and diffraction modalities. It further consists of a library with core routines for e.g. crystallography, symmetry and dynamical scattering simulation. It also has a series of programs for different imaging and diffraction modalities. EMsoft is an open source software where the steps and services it provides are well documented, both in the literature and in the scripts used for running the calculations EMsoft provides. The software is under copyright (c) of Marc De Graef Research Group/Carnegie Mellon University. When writing this thesis EMsoft version 5.0 is the newest available version of the software. However, EMsoft is still under continuous further development [37–39].

2.8   EBSP Quality- and Indexing Accuracy Maps

In order to determine the quality of the experimental EBSPs obtained in an EBSD pattern acquisition run, there are maps which can be used to get an overview of the quality of the patterns. The pattern quality further affects the accuracy of the indexing. The indexing accuracy in TSL OIM, which uses the Hough transformation indexing, may be described using the confidence index (CI). The CI is defined as the number of Kikuchi bands which can be reproduced by different matching solutions. An orientation solution is derived from three intersecting Kikuchi bands. The solution with the highest number of votes is chosen as the solution. The CI is calculated with the formula

$$CI = \frac{V_1 - V_2}{V_{ideal}}, \tag{6}$$

where V_1 is the number of votes to the highest ranked solution, V_2 is the number of votes to the second highest solution and V_{ideal} is the total number of possible votes. The CI value of each pixel from an EBSD run can further be plotted to create a CI map. Low CI values are typical for regions with poor pattern quality, e.g. scratches or grain boundaries [40].

TSL OIM can also generate Image Quality (IQ) maps. The IQ parameter refers to how easy it is for the software to detect the Kikuchi bands through the Hough-transform approach. IQ is in TSL OIM defined as the average height of the detected peaks in the Hough-transforms multiplied by 5. The IQ is affected by a variety of factors, e.g. strain in the diffraction volume of the material, the presence of impurities, camera parameters, vacuum and coating conditions [40].

The dictionary approach does not focus on detecting individual bands and it therefore needs other definitions and approaches when determining the pattern quality and index accuracy. Confidence index maps are also possible to create for dictionary indexing. Here the CI is defined as the highest dot product achieved for the experimental pattern. Since the dot product value is normalized to the interval [-1, 1], the highest dot product also represent the highest confidence index [40].

Another quality map available from DI is orientation similarity maps (OSM). When running the DI approach not only the best matching dot product can be stored, but a sorted list of near-matches, e.g. 20 or 30. This list can further be compared to the four nearest neighbor patterns of the sampling point located at row r and column c, (r, c). If the order of near-matches for a given point (r, c) is written as a set $S_{r,c}$, the near match similarity index $\eta_{r,c}$ can be defined as the average value of the cardinalities (#) a sampling point has with the neighbouring sets (the average number of similar top rank values the sampling point has with its neighbors):

$$\eta_{r,c} = \frac{1}{4}\Big(\#(S_{r,c} \cap S_{r-1,c}) + \#(S_{r,c} \cap S_{r+1,c}) + \#(S_{r,c} \cap S_{r,c-1}) + \#(S_{r,c} \cap S_{r,c+1})\Big) \quad (7)$$

The OSM is generated when $\eta_{r,c}$ is plotted as a function of the sampling point locations. In locations where the neighboring sets $S_{r,c}$ are more different than in the grain interior, the OSM will be able to display the change in the $\eta_{r,c}$-value. This can e.g. be at grain or phase boundaries [40].

2.9 EBSD Pattern Processing

Upon acquiring EBSD patterns, the signal to noise ratio of the raw experimental patterns is poor. To increase the pattern quality is therefore an important tool in increasing the EBSD indexing success rate [3]. In this section the pattern processing steps used for the DI in this thesis is presented.

2.9.1 Static Background Correction

The EBSD patterns are superimposed on a background which typically has a 25 times higher intensity than the patterns themselves. The intensity distribution of the background is dependent on several factors. The local specimen density, the surface relief, variation in the probe current, drift in the alignment of the electron beam column, specimen charging and carbon contamination are all examples of such factors. By applying static background correction, also called flat fielding, the quality of the patterns are increased significantly. The correction normalizes the raw pattern to a recorded static background image. This image contains the image and image artifacts, e.g. defects in the phosphor screen, but no features of the Kikuchi patterns. A way to obtain a static background image is by scanning the beam over a large area containing multiple grains of various orientations. Another way is to create the static background image by averaging the recorded patterns. Static background correction should not be applied when very few grains are present in the region of interest. The Kikuchi pattern features could then end up being present in the static background image and hence weaken or remove the pattern features of the patterns [3]. The static background correction may be performed as a static background subtraction or division, where the static background image is subtracted or divided from each experimental pattern respectively.

2.9.2 Dynamic Background Correction

An other method which remove background noise from Kikuchi patterns is dynamic background correction, also termed "soft" flat fielding or dynamic flat fielding. As for the static background correction a background pattern is subtracted or divided from the experimental patterns. For the dynamic correction the background image is created from the pattern to be corrected itself. The background image is created by blurring

the pattern using a relatively large radius Gaussian convolution mask. The dynamic background correction has the advantage of still being effective to use in cases where it is difficult to obtain a static background image. However, dynamic pattern correction is unable to remove features caused by defects e.g. in the phosphor screen or in the CCD camera [41]. Although being different corrections, static and dynamic background correction may be used in combination on patterns. This could lead to a better end-result when indexing compared to just using one of the correction steps on the patterns [42, 43].

Another approach used which has a similar effect as the dynamic background correction method just described is by using a high-pass fast Fourier transform filtering on the patterns. A high-pass filtering removes low frequencies from the image. A low-pass filtered image represents a more blurred version of its raw image, but it still contains the large spatial extensions. By applying a high-pass filtering to the raw image, which is the opposite of running a low-pass filtering, the large spatial extensions are removed [4, 43]. The blurring effect of the dynamic background correction has in practice the same effect as a low-pass filtering. This does in practice mean that dynamic background correction and high-pass filtering are the same process.

2.9.3   Adaptive Histogram Equalization

The effect of adaptive histogram equalization (AHE) is shown in Figure 2.10. Pictures with a poor lighting may hide details due to lack of contrast in the images. This may also be true for Kikuchi patterns. A method used to increase the contrast in images is adaptive histogram equalization. When applying AHE to an image the pixels are divided into a specific number of regions determined by the user. Within each region the intensity histogram of the pixels is calculated. Based on the histogram the grayscale of each pixel is re-scaled to get a more uniform intensity distribution and which also cover a wider intensity range. The problem with AHE is the potential blocking effect caused by a difference in the mapping between two neighbour regions. Two neighbour pixels having a relative close gray scale value could then end up getting mapped to significantly different grayscale values [44, 45].

2.9.4   Pattern Processing Step Examples

As various pattern processing steps now have been presented, it is time to show how an EBSD pattern looks like when applying the steps. A ferrite pattern of 120 x 120 pixels is in this section presented using one or multiple processing steps. The raw pattern is also shown. In Figure 2.7 is the effect of static background subtraction shown. In Figure 2.8 is the effect of running dynamic background subtraction shown. In Figure 2.9 is the effect of running high-pass filtering with various values for the high-pass filter parameter, w and with various pre-processing steps shown. In Figure 2.10 is the pattern after applying AHE to it shown. Static, dynamic and high-pass filtering corrections are applied prior to the AHE. Patterns with the AHE number of regions parameter, n ranging from 1 to 5 are shown. The actual number of AHE regions is the square of the n-value.

| (a) | (b) | (c) |
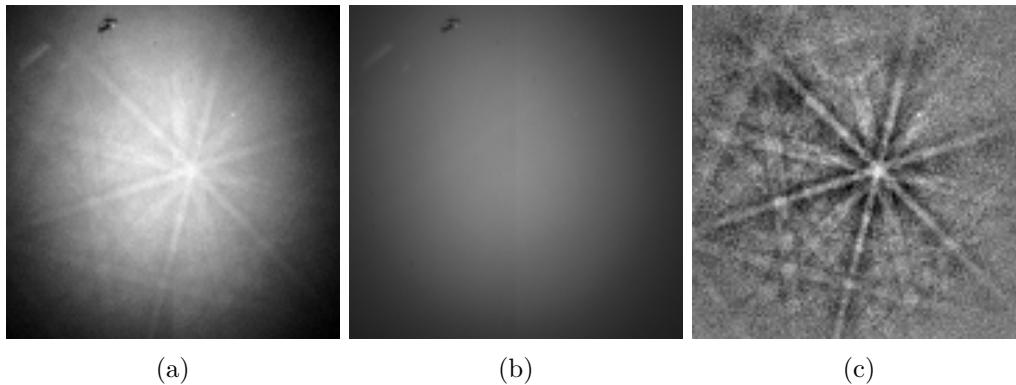
Figure 2.7: The impact of static background subtraction on a raw pattern. Beside flattening the intensity distribution from the center of the pattern to the edges, the observed defects in the phosphor screen are also removed. a) raw pattern, b) static background pattern and c) static background subtracted pattern

| (a) | (b) | (c) | (d) |
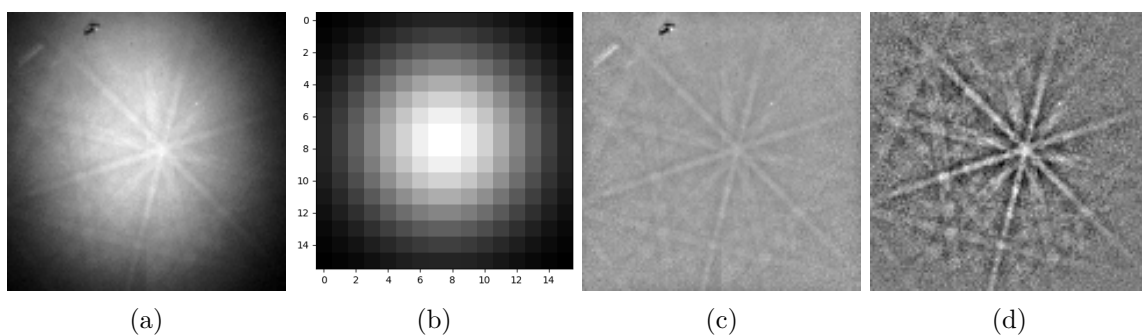
Figure 2.8: The impact of dynamic background subtraction. a) raw pattern, applied kernel for dynamic background subtraction, having a standard deviation of 4 and the size 16x16, c) dynamic background subtraction applied directly to the raw pattern and d) static background subtracting followed by dynamic background subtraction

High-pass filter parameter, w

| 1/128 | 1/64 | 1/32 | 1/16 | 1/8 | 1/4 | 1/2 |

(a) High-pass filtering only

(b) 1) static correction + 2) high-pass filtering

(c) 1) static correction + 2) dynamic correction + 3) high-pass filtering
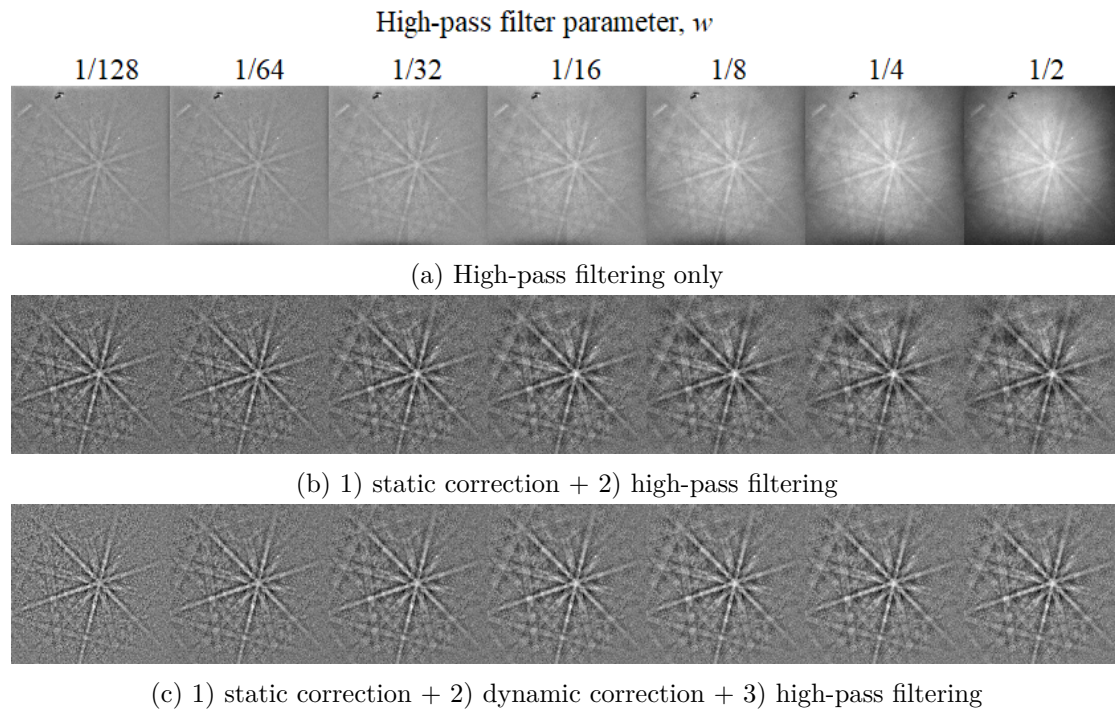
Figure 2.9: The effect of high-pass filtering using various values for the filter parameter w. In a) is the high-pass filtering applied directly to the raw patterns, in b) is static background subtraction performed before the high-pass filtering and in c) are both static and dynamic background subtraction performed before the high-pass filtering

AHE number of regions parameter, n

| No AHE | 1 | 2 | 3 | 4 | 5 |
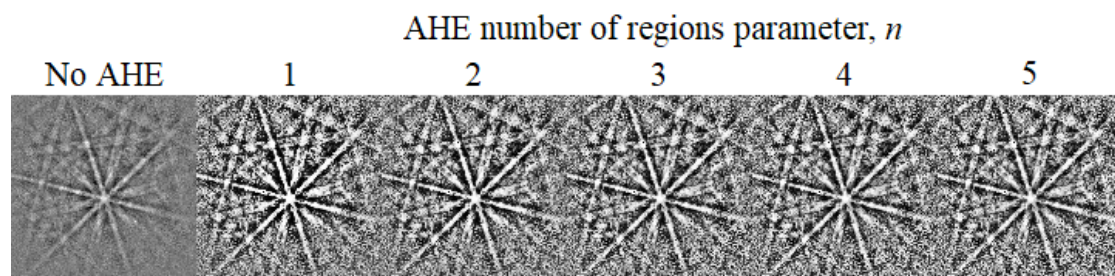
Figure 2.10: The effect of adaptive histogram equalization and varying its number of regions parameter, n visualized. 1) static background subtraction, 2) dynamic background subtraction and 3) high-pass filtering ($w = 1/8$) are applied to the pattern before the AHE is applied. The pattern to the left shows how it looks like before the AHE is applied. Although the AHE makes the Kikuchi features appear clearer, the same effect happens to the noise present in the pattern. The patterns are here rotated 90° clockwise compared to the patterns in Figure 2.7 to 2.9

3   Experimental

In this part is the experimental work which has been done presented. The parameters used for producing the samples, for optical microscope, scanning electron microscope, EBSD hardware & softwares and electron probe micro analysis are presented. The sample preparation for optical microscopy, SEM/EBSD and EPMA are also included.

3.1   Material

The samples studied in this thesis were received from Odd Akselsen at SINTEF. Three different samples have been studied. The first sample presented is the same sample studied in the specialization project this master thesis is based upon. This is an additive manufactured sample produced by WAAM. The sample consists of a SDSS base plate where multiple SDSS weld wires were added on top of each other onto the plate by use of MIG welding. This sample is referred to as *WAAM1*. The second sample studied was another WAAM produced sample with the same chemical composition for the base plate and weld wires as for the WAAM1 sample. However, for this sample the welding parameters are different. This sample is referred to as *WAAM2*. The last sample studied was a super duplex sample of the base plate material. This sample was heat treated at 750 °C for 2 hours and thereafter air cooled down to room temperature when being placed in a pile of sand. This sample is referred to as *SD750C*. The chemical compositions of the base plate and wires is given in Table 3.1. The welding parameters used for WAAM1 and WAAM2 are given in Table 3.2. The weld wall production data are given in Table 3.3. In Figure 3.1 the WAAM1 and WAAM2 samples are depicted as received from SINTEF.

Table 3.1: Chemical composition of base plate and weld wire

Alloy element	C	Si	Mn	P	S	Cr	Ni	Mo	Cu	N	W
Base plate wt%	0.020	0.32	0.85	0.023	0.0003	24.8	6.6	3.7	0.16	0.26	N/A
Wire wt%	0.018	0.3	0.7	0.02	0.001	25.0	9.5	3.7	0.6	0.23	0.6

Table 3.2: Parameters used in the MIG welding of the samples

Parameter	WAAM1	WAAM2
Average Current [A]	197	202
Average Voltage [V]	21	22
Travel speed [mm/s]	7.0	7.0
Wire feed rate [mm/s]	7.7	8.2
Heat input [kJ/mm]	0.59	0.63
Average interpass temperature [°C]	152	85
Average interpass time [s]	360	120
Polarity	DC+	DC+

Table 3.3: Wall production data for the weld samples

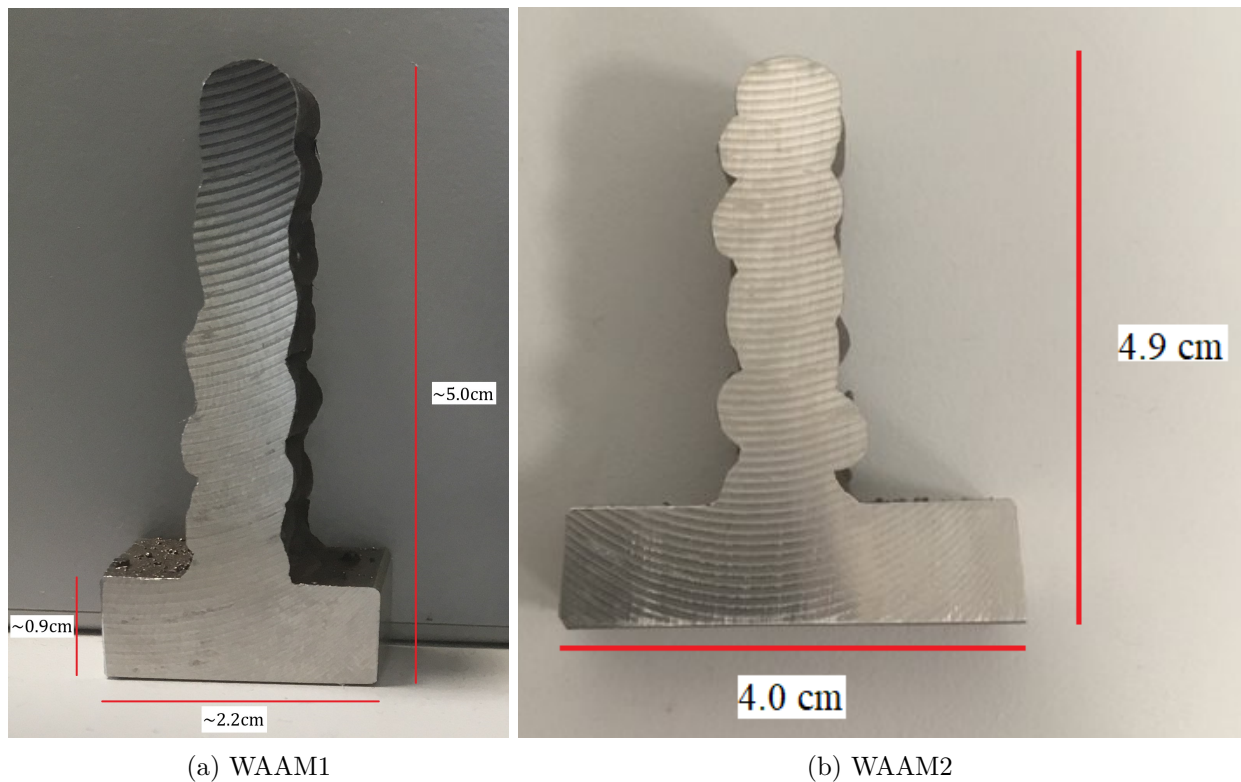| Parameter	WAAM1	WAAM2
Number of layers	16	16
Average layer height [mm]	2.6	2.1
Wall width [mm]	11.6	8.9
Wall length [mm]	230	230
Deposition time [min]	90.5	36.5

(a) WAAM1

(b) WAAM2

Figure 3.1: WAAM1 and WAAM2 samples as received from SINTEF with length scales

19

3.2   Sample Preparation

The sample preperation for the WAAM1 sample was covered in the specialization project [8]. However, the sample preparations used for optical microscopy (for WAAM2) and SEM/EBSD (for WAAM2 and SD750C) are in general the same. The only variation is the grit grinding steps used. In Table 3.4 the common preparation steps used for optical microscopy, SEM/EBSD and EPMA for the WAAM2 and SD750C samples are given. The samples were manually prepared. For the Fine Grinding (FG) and Polishing (P_1 and P_2) steps a Struers Tergamin-30 instrument was used. In between the steps the samples were rinsed in water, and after P_2 they were rinsed with both water and ethanol. After the FG step the samples should also be cleaned with soap and a sponge, to make sure the abrasive particles used in the FG step are not carried over to the P_1 step. However, this cleaning was only performed when preparing the SD750C sample.

Table 3.4: Parameters used in the grinding and polishing steps for the sample preparation of the WAAM2 and SD750C samples

Step	Surface[1]	Lub./Abrasive	Dosing[2]	Time [min]	RS [rpm]	Cooling
Grit 320	SiC foil	Water	On	N/A[3]	100-150	N/A
Grit 500	SiC foil	Water	On	N/A[3]	100-150	N/A
Grit 820	SiC foil	Water	On	N/A[3]	100-150	N/A
Grit 2000	SiC foil	Water	On	N/A[3]	100-150	N/A
Grit 4000	SiC foil	Water	On	N/A[3]	100-150	N/A
FG (9 μm)	MD-Largo	DiaPro All/Lar.9	7	5	150	Off
P_1 (3 μm)	MD-Dac	DiaPro Dac3	9	4	150	Off
P_2 (1 μm)	MD-Nap	DiaPro Nap-B1	10	3	150	Off

Lub. = Lubricant, RS = Roation speed
[1] The surfaces are produced by Struers.
[2] The dosing parameter is an option given by the Struers Tergamin-30 instrument.
[3] The time used in the grinding steps are determined by the time required to get the sample surface plane grinded or the time to remove the deformation of the previous grinding step.

The WAAM2 sample was first studied in optical microscopy. As the final preparation for optical microscopy the sample was electropolished externally with the steps given in Table 3.5. The acids were poured into a steel cup connected to the negative pole of a voltage source. The sample surface to be electropolished was submerged into the acid, when a wire connected to the positive pole was in contact with to the sample. The sample was held with a tong when performing the electropolishing. The sample was rinsed in water and ethanol after each electropolishing step.

Table 3.5: Parameters used in the electropolishing

Step	Electrolyte	Voltage [V]	Time [s]
1	10% Oxalic acid	3	3
2	60% HNO_3	1	15

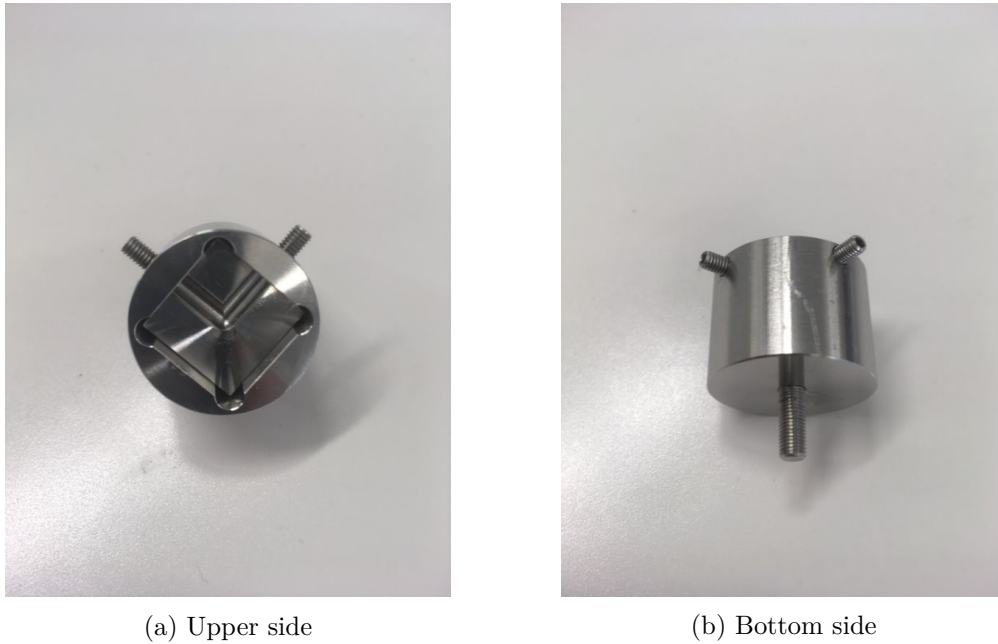(a) Upper side   (b) Bottom side

Figure 3.2: Sample holder used for manual grinding and polishing, and as inner sample holder for vibration polishing. The diameter of the sample holder is approximately 25 mm and the inner square has side lengths of about 16 mm. The screw on the bottom side is used to adjust the height of the square platform, where the sample is mounted into the sample holder. The screws on the side are used to fasten the sample to the sample holder

When preparing the WAAM2 sample for SEM/EBSD, the sample was first cut into smaller pieces which could fit into the sample holder shown in Figure 3.2. To remove the electropolished surface, the sample was re-polished with step P_1 and P_2. The WAAM2 and SD750C samples were after the P_2 step vibration polished by using a Buehler Vibromet 2 vibration polishing instrument. The samples were fastened in the sample holder shown in Figure 3.2, which was further mounted into a standard Vibromet sample holder. The samples were vibration polished for 24 hours with an amplitude of 70% and with a weight of 200 grams loaded onto the Vibromet sample holder, giving it additional mass. After the vibration polishing the samples were rinsed in an ultrasonic bath for 15 minutes. The samples were submerged in a beaker containing acetone for the ultrasonic rinsing. As the final preparation step the samples were plasma cleaned for 5 minutes with the instrument Fischione Model 1020. The plasma cleaning was performed shortly before the SEM/EBSD examinations.

For the Electron Probe Micro Analysis (EPMA) the WAAM2 sample was examined as prepared for SEM/EBSD. On the other hand, the SD750C sample was only prepared with the steps given in Table 3.4 followed by the ultrasonic rinsing and plasma cleaning previously described. The SD750C sample was vibration polished for SEM/EBSD after the EPMA analysis was completed.

In the specialization project the WAAM1 sample was cut into three parts before the

EBSD examinations. The upper part was referred to as the *upper sample* and the lower part was referred to as the *lower sample*. These parts were examined with EBSD. However, the part in the middle, now referred to as the *middle sample*, was not examined with EBSD. Figure 3.3 shows how the WAAM1 sample was cut and where the three sub-samples mentioned were origin from in WAAM1. Also, none of the three WAAM1 samples were studied using backscatter electron imaging in the specialization project. The *upper sample* and the *middle sample* were therefore studied with backscatter electron imaging for this master thesis. The *upper sample* was studied as prepared for optical microscopy and SEM/EBSD, having an electropolished surface. The *middle sample* was prepared with the grinding and polishing steps given in Table 3.4. Both samples were also ultrasonic rinsed and plasma cleaned before the backscatter electron imaging [8].
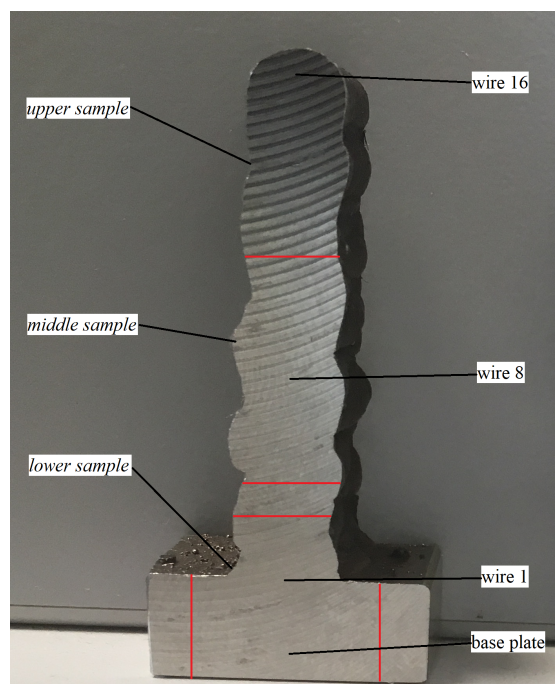

Figure 3.3: The WAAM1 sample shown before it was cut. The red lines shows approximately where the sample was cut. On the left side in the figure the location of the *upper*, *middle* and *lower sample* are labeled. On the right side the location of the base plate and the approximate site of some of the additive weld wires are labeled. The WAAM2 sample was cut in a similar way as WAAM1

3.3   Optical Microscopy

Optical microscopy was used to get a better overview of the structure in the WAAM2 sample. A Leica MEF4 instrument was used. The sample was studied and depicted in bright field and by using objective lenses of 50x and 100x magnification. The obtained images were photoshoped to increase the contrast and sharpness in the images.

3.4   SEM and EBSD Parameters

The SEM used to study the samples was a Zeiss Ultra 55 FESEM equipped with a NORDIF UF-1100 EBSD detector. The EBSD acquisition settings are selected using the NORDIF 3.1.2 software. In Table 3.6 the parameters used for the backscatter electron imaging are given. In Table 3.7 the parameters used for EBSD are given, which all are selected by operating the SEM. In Table 3.8 the parameters used in NORDIF 3.1.2 EBSD acquisition are shown. A specimen tilt angle of 70° was used for all EBSD runs. When analysing the WAAM1 sample in the specialization project a step size of 0.2 μm was used [8]. For the WAAM2 and SD750C samples a step size of 0.1 μm was instead used.

Table 3.6: SEM parameters used for backscatter electron imaging. Two value sets were used for the imaging

Parameter	Value set 1	Value set 2
Acceleration voltage [kV]	10	10
Working distance [mm]	~8.5	10.6
Aperture [μm]	300	120
High current mode	ON	ON
BSD Gain	Very High*	High
Contrast	50.0 %	50.0 %
Brightness	~26.7 %	15.3 %

BSD = Backscatter detector
* The actual BSD Gain used was not checked, but this input is believed to be applied

Table 3.7: SEM parameters used for EBSD

Parameter	Value
Acceleration voltage	20 kV
Working distance	25-27 mm
Magnification	200x / 300x
Aperture	300 μm
Specimen tilt angle	70°
High current mode	ON*
Dynamical focus	10 - 15 %

* The probe current of the instrument with the used settings has earlier been estimated to have a value of $60 - 70$ nA [26]

Table 3.8: Parameters used in NORDIF 3.1.2 software for EBSD

Parameter	Acquisition	Calibration
Averaging	4	5
Speed [fps]	400	140
Resolution [px]	120x120	160x160
Exposition time [μs]	2450	7092
Gain [dB]	4	1

3.5 EPMA Parameters

For EPMA a JXA-8500F Field Emission Electron Probe Microanalyzer instrument was used. The microanalyzer was operated by NTNU senior engineer Morten Peder Raanes. For the EPMA mapping an acceleration voltage of 10 kV and a beam current of 20 nA were used. The mapping was performed in spot mode.

3.6   Hough Indexing

The software EDAX TSL OIM Data Collection version 7.3.b was used for the Hough Indexing. The parameters used by Mona Haukali in her specialisation project after optimizing the Hough indexing for the sigma and chi phases were also used when indexing the EBSPs for this thesis. She also received new binary material (bmt) files from Dr. Rene de Kloe (applications specialist, EDAX) for the sigma and chi phase, which both were used for this thesis as well [5, 8]. In Table 3.9 the OIM Hough parameters are given. In Table 3.10 the image processing functions used on the experimental patterns and their order are shown. In Table 3.11 and 3.12 information about the phase parameters and applied reflectors in the bmt files for the four phases are given.

Table 3.9: OIM Data Collection Hough Parameters

Parameter	Value
Binned Pattern Size	96
Theta Step Size	0.5°
Rho Fraction	88
Max Peak Count	10
Min Peak Count	3
Hough Type	Classic
Hough Resolution	Low
Convolution Mask	7x7
Min Peak Magnitude	1
Min Peak Distance	10
Peak Symmetry	0.70
Vertical Bias	0%

Table 3.10: OIM Data Collection image processing recipe applied to the patterns

Image Processing Function	Applied order
Background Subtraction	1
Normalize Intensity Histogram	2
Dynamic Background Subtraction	3

Table 3.11: Phase parameters of the bmt files used in OIM Data Collection

Phase	Formula	Point Group	Lattice Parameters [nm]
Ferrite, α	Fe	Cubic (Oh) [m-3m]	$a = 0.287$
Austenite, γ	Fe	Cubic(Oh) [m-3m]	$a = 0.365$
Sigma, σ	FeCrMo	Tetragonal (D4h) [4/mmm]	$a = 0.917$ $c = 0.4741$
Chi, χ	$Cr_{12}Fe_{32}Mo_7Ni_7$	Cubic (Oh) [m-3m]	$a = 0.89$

Table 3.12: Reflectors applied in the indexing of the phases in OIM Data Collection

Band	Ferrite	Austenite	Sigma	Chi
0 -1 1	✕			
1 -1 -1		✕		
0 0 2			✕	
0 -2 0	✕	✕		
1 -2 -1	✕			
0 -2 2		✕		
2 0 2			✕	
2 1 2			✕	
2 2 2			✕	
0 -3 1	✕			
1 -3 -1		✕		
3 3 0			✕	✕
3 1 1			✕	
3 3 1			✕	
3 3 2				✕
4 4 4				✕
4 0 0				✕
0 0 4			✕	
4 1 1			✕	✕
4 1 3			✕	
4 -1 0			✕	
-4 7 2			✕	
-5 3 -2			✕	
6 6 0			✕	
7 2 0			✕	

3.7   EMsoft Dictionary Indexing

A detailed guide in how the dictionary indexing is executed is given in the appendix. In this section only the input for creating each crystal structure file for the four phases α, γ, σ and χ, and the used EBSD pattern processing recipe for the DI are presented.

In Table 3.13 to 3.16 the required input parameters used in creating the crystal structure files for α, γ, σ and χ are given. In Table 3.14 to 3.16 the asymmetric atom coordinates X, Y and Z of the given atom site as fraction of the lattice parameter *a*, *b* and *c* respectively are given. *f* is the site occupation parameter of the given element in the given asymmetric site. B_{iso} is the *Debye-Waller factor* of the element in the asymmetric site. According to Jackson et al. (2019) [4] a Debye-Waller factor value in the range $0.004 - 0.006$ nm^2 is almost always a reasonable choice if the actual value is unknown. All Debye-Waller factors for α, γ and σ are therefore set to $B_{iso} = 0.005$ nm^2 [4]. By running the *Monte Carlo BSE Simulation* and *EBSD Master Pattern Simulation* steps, where each of the four crystal structure files previously created are used, the simulated master patterns given in Figure 3.4 are obtained. The master pattern files were obtained in the specialization project this master thesis is based on. The files were obtained in collaboration with NTNU Ph.D. candidate Håkon W. Ånes [8].

Table 3.13: Phase parameters of the crystal structure files created in EMsoft [25, 46–48]

Phase	Formula	Symmetry	Space Group	Lattice Parameters [nm]
Ferrite, α	Fe	Cubic	229: Im-3m	a = 0.28665
Austenite, γ	Fe	Cubic	225: Fm-3m	a = 0.3595
Sigma, σ	FeCr	Tetragonal	136: P4$_2$/mnm	a = 0.87961
				c = 0.45605
Chi, χ	Fe$_{36}$Cr$_{15}$Mo$_7$	Cubic	217: I-43m	a = 0.8854

Table 3.14: Atom site occupation parameters used in the crystal structure file for ferrite (α) and austenite (γ) [46, 47]. The only differences between the crystal structure files for α and γ are the space group and the lattice parameter, as shown in Table 3.13

Site	Element	X	Y	Z	f	B_{iso} [nm^2]
Fe	Fe	0.0000	0.0000	0.0000	1	0.005

Table 3.15: Atom site occupation parameters used in the crystal structure file for sigma (σ) [48]

Site	Element	X	Y	Z	f	B_{iso} [nm^2]
M1	Fe	0.00000	0.00000	0.00000	0.825	0.005
M1	Cr	0.00000	0.00000	0.00000	0.125	0.005
M2	Fe	0.39875	0.39875	0.00000	0.265	0.005
M2	Cr	0.39875	0.39875	0.00000	0.735	0.005
M3	Fe	0.46351	0.13131	0.00000	0.350	0.005
M3	Cr	0.46351	0.13131	0.00000	0.650	0.005
M4	Fe	0.73921	0.06608	0.00000	0.825	0.005
M4	Cr	0.73921	0.06608	0.00000	0.175	0.005
M5	Fe	0.18274	0.18274	0.25166	0.350	0.005
M5	Cr	0.18274	0.18274	0.25166	0.650	0.005

Table 3.16: Atom site occupation parameters used in the crystal structure file for chi (χ) [25]

Site	Element	X	Y	Z	f	B_{iso} [nm^2]
M1	Fe	0.356	0.356	0.042	0.625	0.01
M1	Cr	0.356	0.356	0.042	0.375	0.01
M2	Fe	0.089	0.089	0.278	0.875	0.01
M2	Cr	0.089	0.089	0.278	0.125	0.01
Mo1	Mo	0.000	0.000	0.000	1	0.01
Mo2	Mo	0.317	0.317	0.317	1	0.01

Max. int.: 2.30   Mean int.: 0.72

(a) Ferrite (α)

Max. int.: 2.60   Mean int.: 0.74

(b) Austenite (γ)

Max. int.: 0.76   Mean int.: 0.32

(c) Sigma (σ)

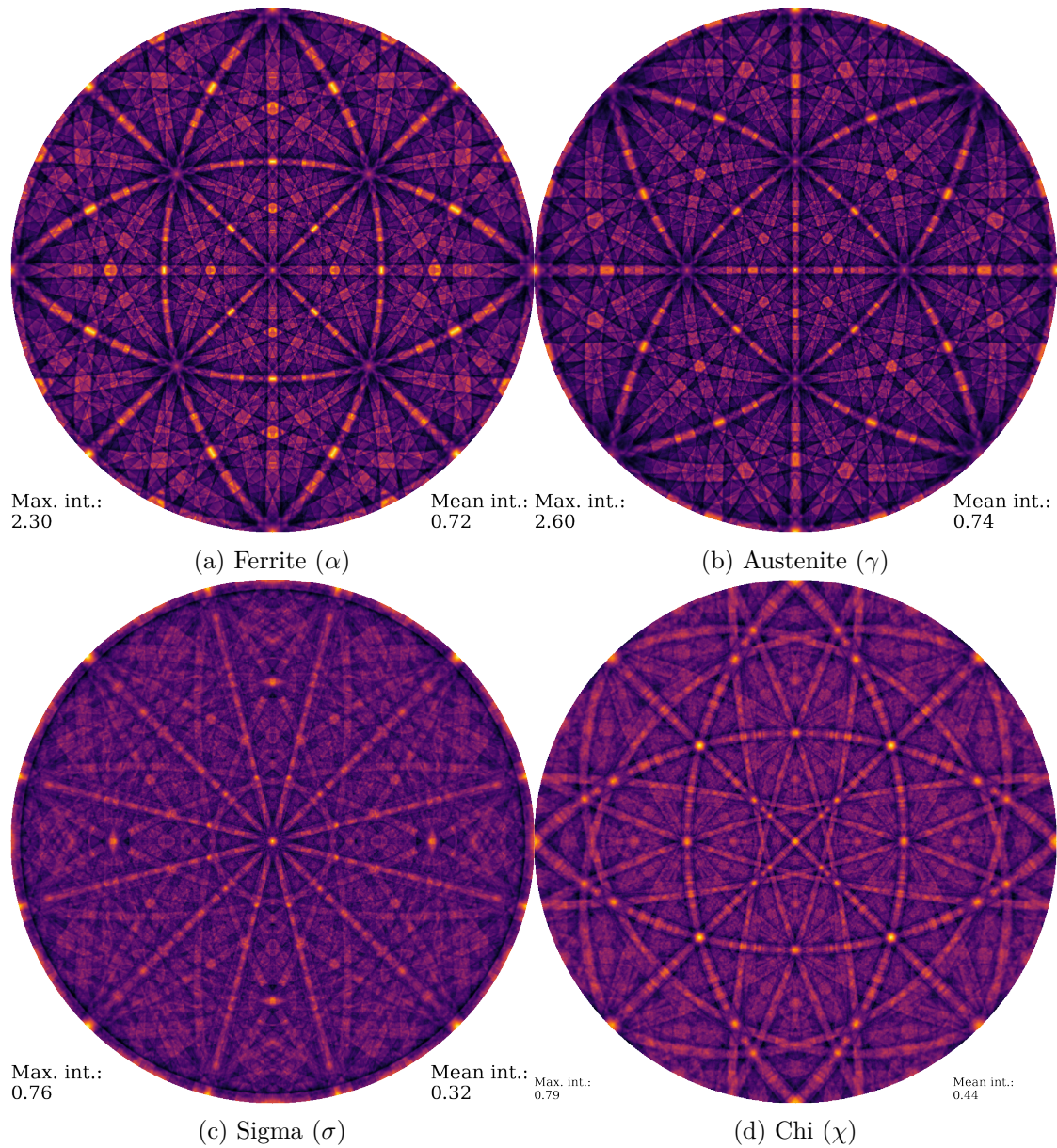Max. int.: 0.79   Mean int.: 0.44

(d) Chi (χ)

Figure 3.4: Simulated master patterns of the phases used in the dictionary indexing for energy bin 20 keV. Here the spherical projections of the northern hemisphere of the master patterns are shown. Maximum and mean intensity of the master patterns are also labeled

Before running the dictionary indexing, a pattern processing recipe was applied to the experimental patterns. In Table 3.17 and 3.18 the five processing steps used in this thesis are presented. The static and dynamic background corrections were executed in the open-source Python library *KikuchiPy* [49], where KikuchiPy version 0.1 was used. For the static background correction a static background image is subtracted from the experimental pattern. The static background image is acquired before the EBSD pattern acquisition is started. The static background image is recorded from an area which is larger than, but includes the area of the EBSD pattern acquisition. The static background correction is followed by the dynamic background correction. The processing input for the static and dynamic corrections used are given in Table 3.17. When indexing with EMsoft, high-pass filtering and adaptive histogram equalization (AHE) are also applied on the experimental pattern as well as on the simulated patterns. The AHE algorithm used by EMsoft is described in Pizer et al. (1987) [50]. The high-pass filtering is applied before the AHE. These processing steps can not directly be turned off, but each of them are controlled by a pre-processing parameter. The high-pass filtering has a parameter w and the AHE has a number of regions parameter n [4]. The high-pass gaussian filtering EMsoft is using is given by equation (8) [51]:

$$G_{highpass} = 1 - e^{-wr^2} \tag{8}$$

, where $G_{highpass}$ is the gaussian filter and r is the distance from the center of the spectrum. Various w and n values were tested to find which inputs were giving the best results when indexing with the α, γ, σ and χ-phases. Here, the best result is considered the parameters which leads to the lowest mis-indexing rate. This topic is covered more in detail in section 5. EMsoft also offers the user to use an intensity scaling mode on the simulated patterns. Here a gamma correction with a gamma value of 0.33 was always used, as recommended by Jackson (2019) [4]. Since multiple corrections steps are used with varying w and n-values, a notation is used to clearer show what pattern processing recipe is used for each case. The abbreviations of processing steps, given in Table 3.17 and 3.18, are placed inside a bracket to display the used processing steps. The applied w and n-values are some times given as a subscript after the H and A abbreviation respectively.

After the dictionary indexing runs were completed the obtained dot product files were always refined by running the *Orientation Refinement* step before the *Dot Product File Merge* was executed. Based on the refined dot product files, the dictionary patterns of best fit to each experimental pattern was simulated for the phases of interest. The dictionary indexing was in general done by using EMsoft version 5.0. EMsoft version 4.3 was only used for a few cases. If nothing else is stated, EMsoft version 5.0 was used. For the orientation refinement and pattern simulation EMsoft version 4.3 was always used. To illustrate the effect of the orientation refinement step, IPF maps from a pattern file

before and after the refinement is shown in Figure 3.5. In Figure 3.6 simulated patterns of best match to a experimental σ-pattern is shown both before and after the orientation refinement is performed.

When running EBSD on a sample, patterns from a relative large area were acquired. This was necessary to make sure regions where secondary phases potentially were formed would get covered in the pattern acquisition. These files could on the other hand get very big with respect to the dictionary indexing. Regions from the bigger files were therefore cropped out using either Nordif Extraction 1.0.15 or KikuchiPy. KikuchiPy version 0.2 was further used to create averaged EBSD patterns by manually selecting experimental patterns of the same orientations to create a pattern containing lesser background noise. The pattern intensity map seen in Figure 4.34d is also obtained from KikuchiPy. Each point in the map represent the intensity at the detector for the given point. Here, it is the default navigator map appearing when uploading the raw pattern file into KikuchiPy and using the plot function.

Table 3.17: Pattern processing steps executed in KikuchiPy

Pattern processing step	Processing input	Abbreviation
Static Background Correction	operation='subtract', relative=True	S
Dynamic Correction	operation='subtract', sigma=None*	D

* For sigma=None a standard deviation equal to ($EBSD\ pattern\ width$)/30 is applied for the gaussian kernel when using KikuchiPy v.0.1 [49]. Since an EBSD pattern width of 120 pixels is used for this thesis, $\sigma = 4$.

Table 3.18: Pattern processing steps and their parameters available through EMsoft

Pattern processing step	Pre-Processing parameter	Abbreviation
High-pass filtering	Hi-pass parameter, w	H
Adaptive Histogram Equalization	# regions parameter, n	A
Gamma Correction	Gamma factor	G

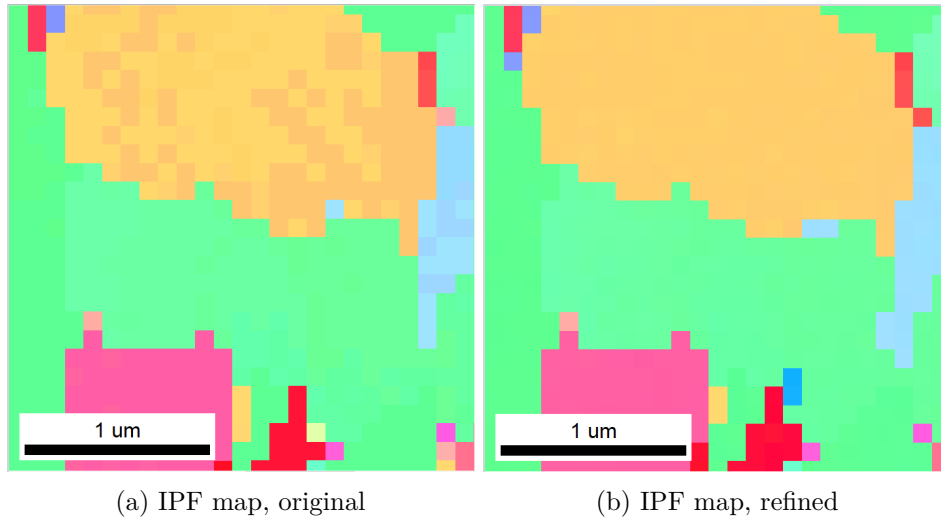(a) IPF map, original   (b) IPF map, refined

Figure 3.5: IPF maps showing the effect of the orientation refinement step. a) IPF map from original dot product files, b) IPF map from refined dot product files

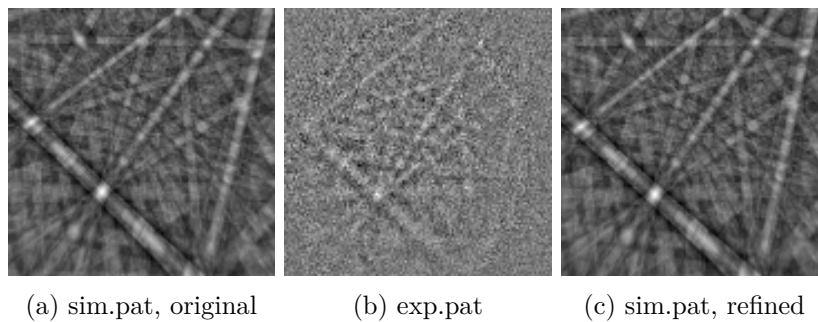(a) sim.pat, original   (b) exp.pat   (c) sim.pat, refined

Figure 3.6: Simulated pattern of best match from an original DP file (left) compared to the simulated pattern from the refined DP file (right). In the middle is the experimental pattern shown, having a [SD] pattern processing recipe. As the DP-file is refined the simulated pattern is slightly shifted, making the gap between the Kikuchi band and the right pattern edge in the top right corner larger

4 Results

In this section the obtained results are presented. In section 4.1 the results from the dictionary indexing pattern processing tuning of the WAAM1 sample are presented. BEIs of the WAAM1 sample are also included. In section 4.2 the results of the WAAM2 sample are presented. Optical microscopy images, BEIs, and the results from EPMA and further DI pattern processing tuning are included. A comparison of results from HI and DI is also included. In section 4.3 the results of the SD750C sample are presented. BEIs, obtained EPMA X-ray maps and results from even further pattern processing testing for DI are shown. A comparison of the results from HI and DI is also included here.

4.1 Characteriztion of WAAM1

The results from the specialization project showed that χ-phase was mis-indexed for all pattern files presented when included as a phase in the indexing [8]. It was therefore necessary to test what effect applying different pattern processing recipes/parameters would have on the dictionary indexing. In this section the work related to the re-indexing of the pattern files previous obtained in the specialization project from the WAAM1 sample is presented. BEIs from WAAM1 are also shown.

4.1.1 Pattern Processing, Vibration Polished Surface

The first pattern file being re-indexed using DI was the *Transition zone* file. This file contained EBSPs from the transition zone between the base plate and the first weld wire. The EBSPs are from a vibration polished surface. In the specialization project the pattern file was indexed applying a $[\text{SDH}_{1/40}\text{A}_5\text{G}]$ pattern processing, where the hi-pass filtering was set to $w = 1/40$ and the AHE number of regions parameter was set to $n = 5$ [8]. The pattern file was for this thesis initially re-indexed using two additional pattern processing recipes. For the first case a $[\text{SH}_{1/40}\text{A}_1\text{G}]$ processing recipe was used, where the dynamic background correction was not used and the AHE n-value was changed to $n = 1$. All the other parameters were unchanged. For the second case a $[\text{SDH}_{1/40}\text{A}_1\text{G}]$ pattern processing recipe was applied. Here the dynamic background correction and $n = 1$ were used. All the other parameters were unchanged. Since there were no indications of σ-phase being present in the pattern file, the re-indexings did not include this phase. This was done to save time. In Table 4.1 the phase fractions obtained form HI and DI (for the three different indexing runs) are presented. In Figure 4.2 to 4.4, phase maps, IQ or CI maps and IPF maps from HI and the three DI cases are shown. In Figure 4.5 and 4.6 two experimental pattern examples are shown. The first pattern is indexed as α for both $n = 1$ and 5. The second pattern is indexed as α when $n = 1$ is used, but as χ when $n = 5$ is used.

Table 4.1: Phase fractions of the transition zone pattern file of the WAAM1 sample. $w = 1/40$ was used for all patterns. Either $n = 5$ or $n = 1$ was used

Phase \ Fraction,%	HI*,**	DI [$SDH_{1/40}A_5G$]**	DI [$SH_{1/40}A_1G$]	DI [$SDH_{1/40}A_1G$]
Ferrite (α)	54.1	52.9	54.1	54.2
Austenite (γ)	45.5	44.3	45.9	45.8
Sigma (σ)	0.3	0.0	N/A	N/A
Chi (χ)	0.1	2.8	0.0	0.0

* An error in the rounding of the numbers leads to an uncertainty of $\pm 0.1\%$ in the HI data.
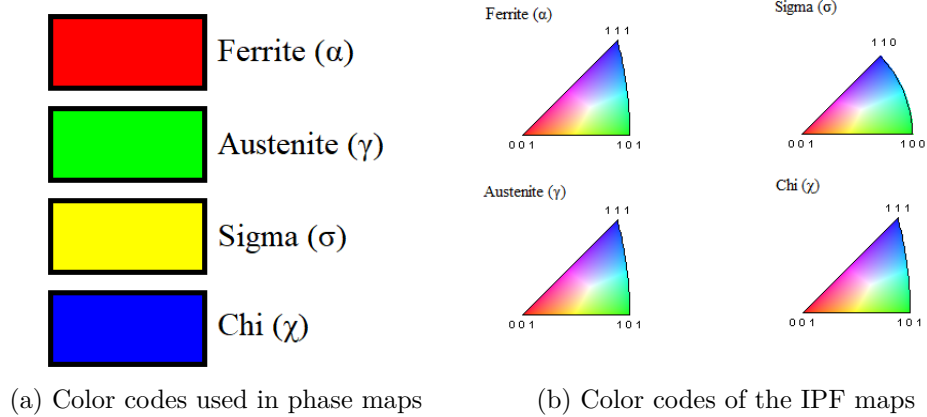** Values are acquired from the specialization project [8].

(a) Color codes used in phase maps   (b) Color codes of the IPF maps

Figure 4.1: Color codes used to describe a) phase maps and b) IPF maps

(a) PM, HI [8]

(b) PM, DI [SDH$_{1/40}$A$_5$G] [8]

(c) PM, DI [SH$_{1/40}$A$_1$G]

(d) PM, DI [SDH$_{1/40}$A$_1$G]
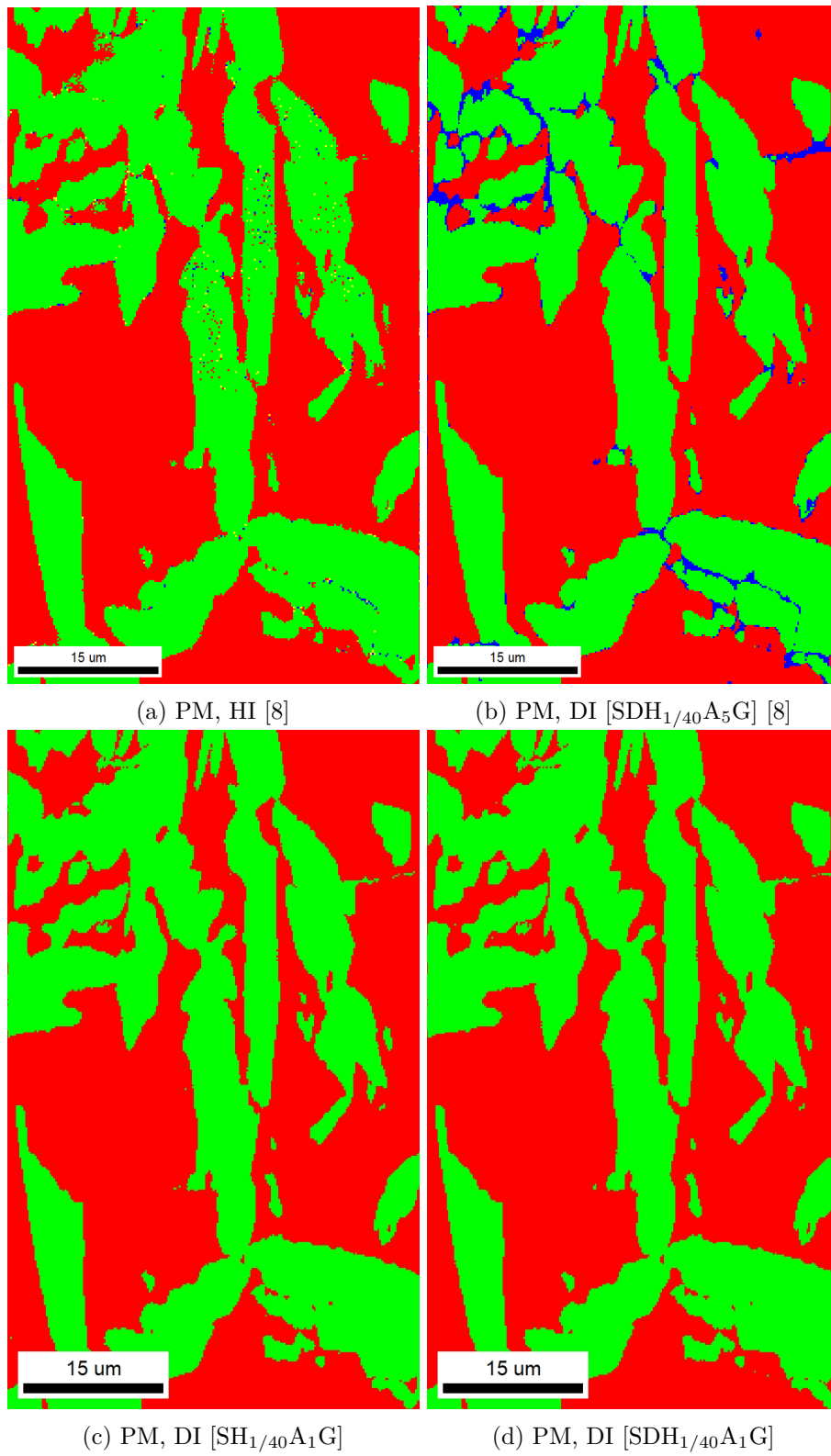
Figure 4.2: Phase maps of the WAAM1 transition zone, vibration polished

35

(a) IQ map, HI [8]

(b) CI map, DI [SDH$_{1/40}$A$_5$G] [8]

(c) CI map, DI [SH$_{1/40}$A$_1$G]

(d) CI map, DI [SDH$_{1/40}$A$_1$G]
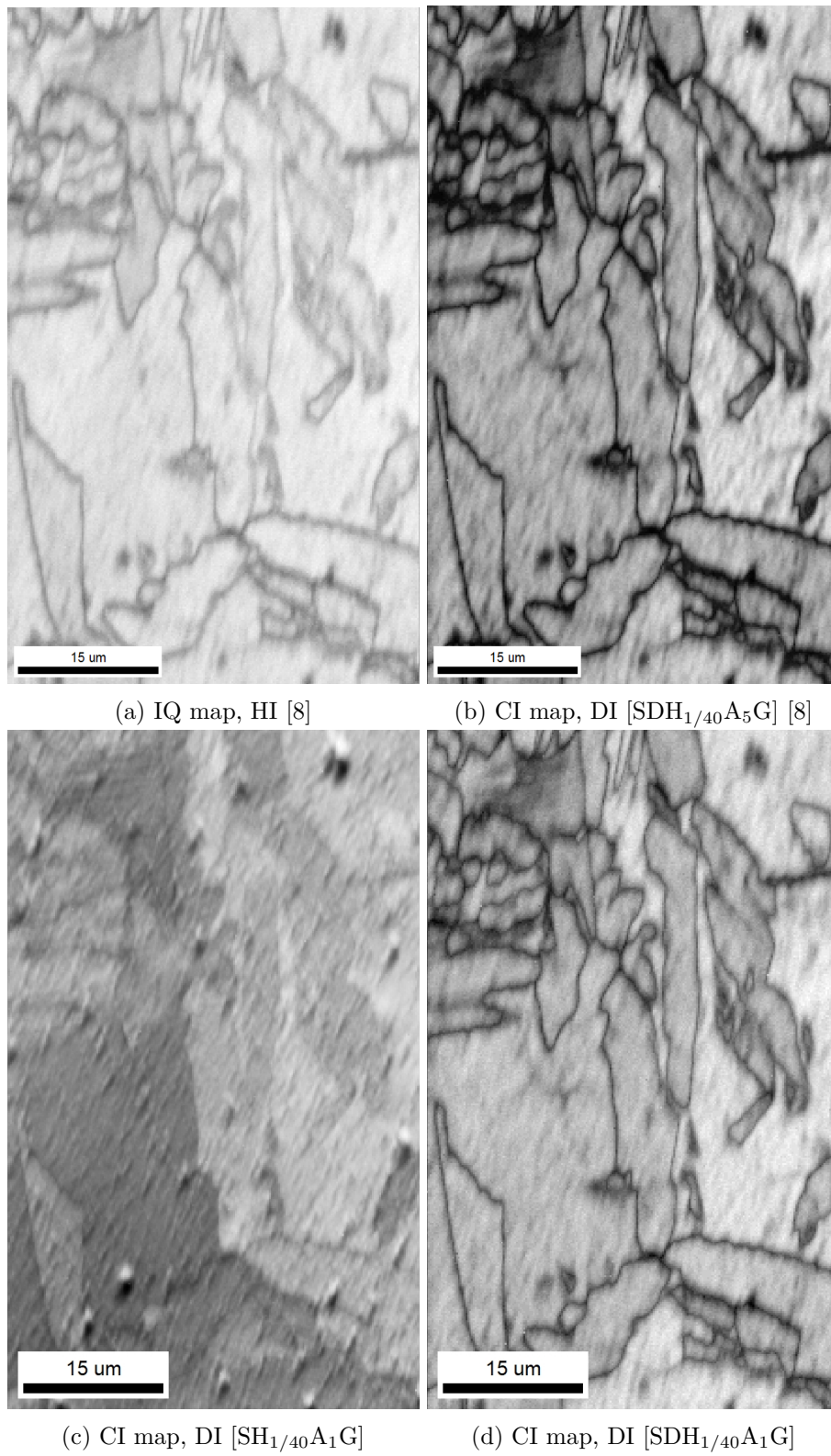
Figure 4.3: IQ or CI maps of the WAAM1 transition zone, vibration polished

(a) IPF map, HI [8]

(b) IPF map, DI [SDH$_{1/40}$A$_5$G] [8]

(c) IPF map, DI [SH$_{1/40}$A$_1$G]

(d) IPF map, DI [SDH$_{1/40}$A$_1$G]
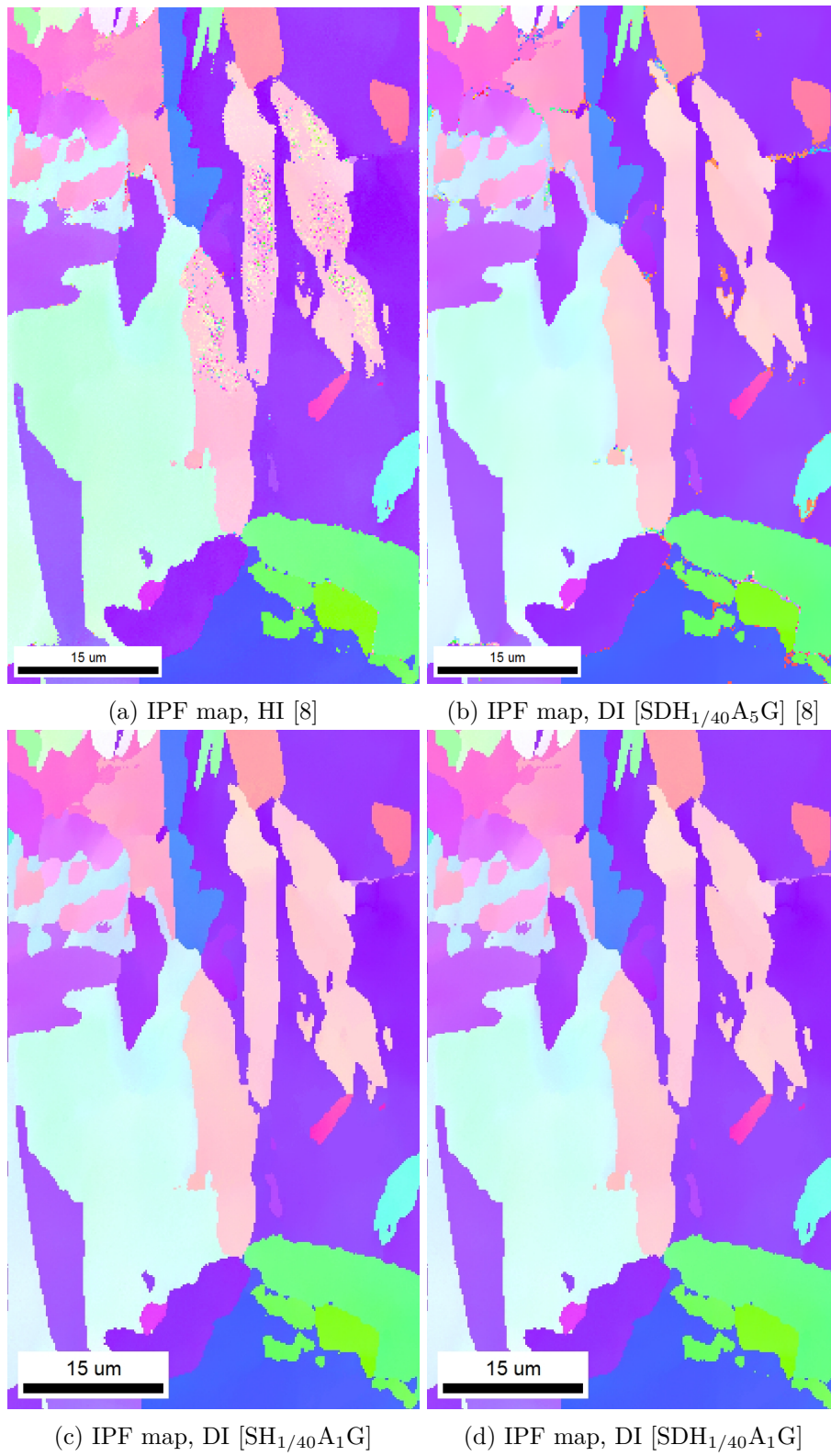
Figure 4.4: IPF maps of the WAAM1 transition zone, vibration polished

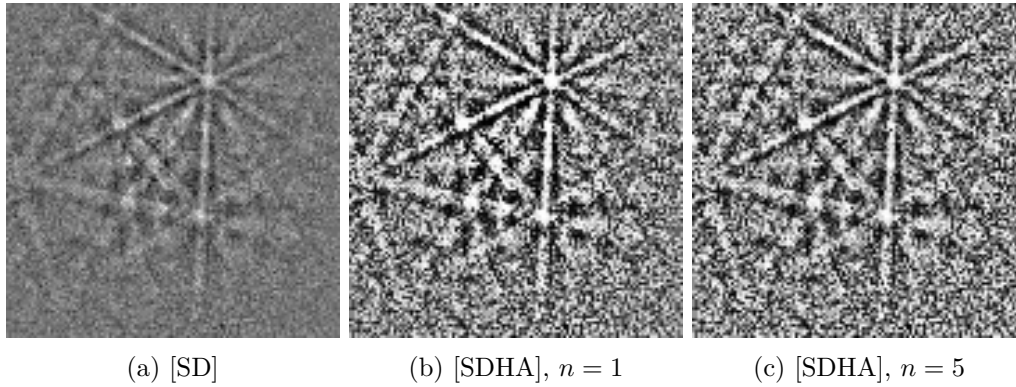(a) [SD]   (b) [SDHA], $n = 1$ (c) [SDHA], $n = 5$

Figure 4.5: Pattern indexed as α when using both $n = 1$ and $n = 5$. In a), b) and c) the experimental pattern is shown for different pattern processing recipes
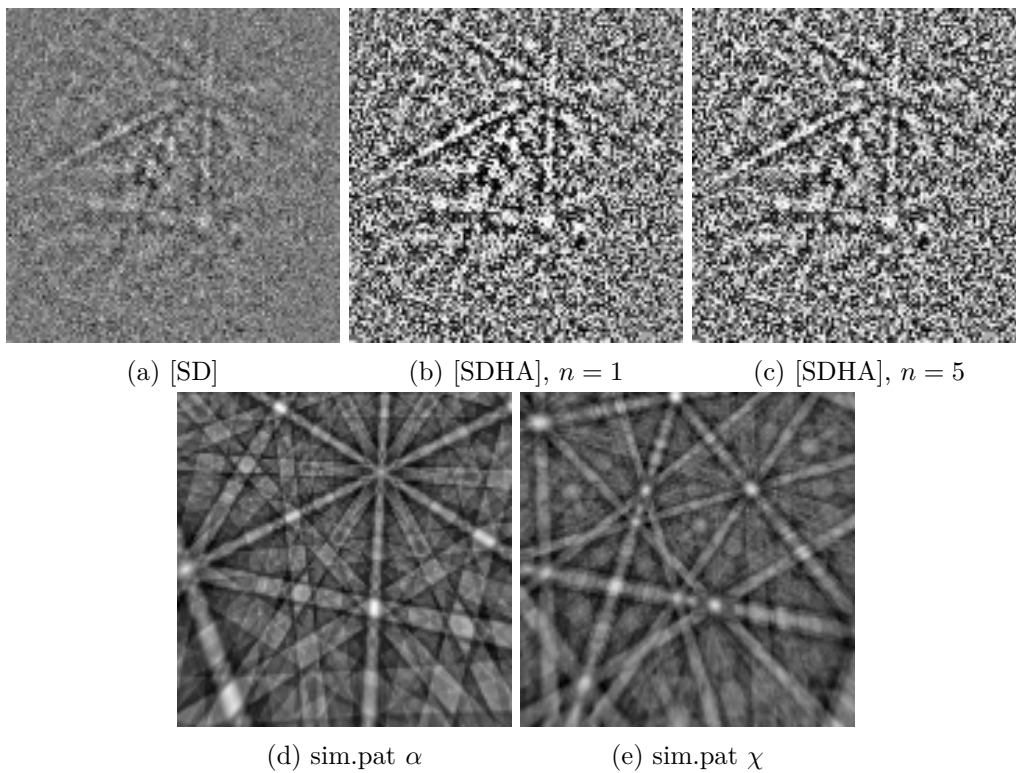

(a) [SD]   (b) [SDHA], $n = 1$ (c) [SDHA], $n = 5$

(d) sim.pat α (e) sim.pat χ

Figure 4.6: Pattern indexed as α when using $n = 1$, but indexed as χ when using $n = 5$. In a), b) and c) the experimental pattern is shown for different pattern processing recipes. In d) and e) the simulated patterns of α and χ of best match to the experimental pattern are shown respectively

As seen in Table 4.1 and in Figure 4.2, the two re-indexing runs do not index any χ-phase at all. Only α and γ are indexed. There are some minor differences between the phase maps (Figure 4.2c and 4.2d) and the IPF maps (Figure 4.4c and 4.4d) of the re-indexings. The most notable difference between the two re-indexings is seen in the CI maps in Figure 4.3c and 4.3d.

To better get an overview of what effect changing the high-pass w-value has, two additional re-indexing runs were performed. The pattern processing recipes [SH$_{1/8}$A$_1$G] and [SDH$_{1/8}$A$_1$G] were applied. In Table 4.2 the mean dot product data of the five dictionary indexing runs of the pattern file is presented. As the [SDH$_{1/8}$A$_1$G] pattern processing got the highest mean DP value among the four re-indexing runs, applying dynamic background subtraction to the patterns and setting $w = 1/8$ were mainly used for the rest of the thesis.

Table 4.2: Mean dot product data for the five dictionary indexing runs performed for the WAAM1 transition zone pattern file of a vibration polished surface
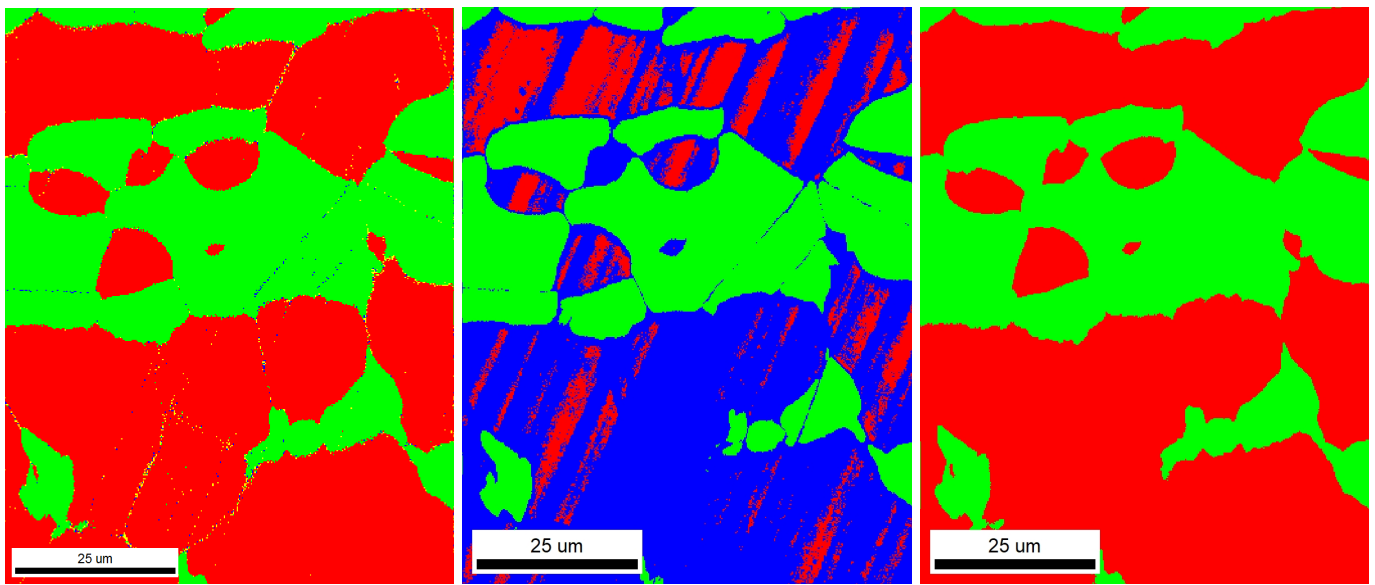
	Pattern processing	Mean DP value
Original Run	[SDH$_{1/40}$A$_5$G]	0.866
	[SH$_{1/40}$A$_1$G]	0.768
Re-indexing Runs	[SH$_{1/8}$A$_1$G]	0.750
	[SDH$_{1/40}$A$_1$G]	0.781
	[SDH$_{1/8}$A$_1$G]	0.783

4.1.2   Pattern Processing, Electropolished Surface

The transition zone of WAAM1 was also examined with EBSD when being prepared using electropolishing. The results from the specialization project showed that the used pattern processing recipe for DI caused a lot of mis-indexing of χ-phase for what was believed to be α-patterns. The electropolishing seemed to result in a poor α-pattern quality compared to the γ-patterns [8]. To test what effect changing the pattern processing recipe would have, the pattern file was re-indexed with DI using a $[\text{SDH}_{1/8}\text{A}_1\text{G}]$ processing. In Table 4.3 the phase fraction of the indexing runs using HI and DI are presented. In Figure 4.7 to 4.10 various EBSD maps for the three indexing runs are presented. In Figure 4.11 to 4.13 three experimental pattern examples are presented together with the simulated pattern of best match for the relevant phase(s).

Table 4.3: Phase fractions of the transition zone pattern file for the WAAM1 sample. The sample had an electropolished surface for this pattern acquisition. The obtained phase fractions for HI and the two DI runs using $n = 5$ and $n = 1$ are presented
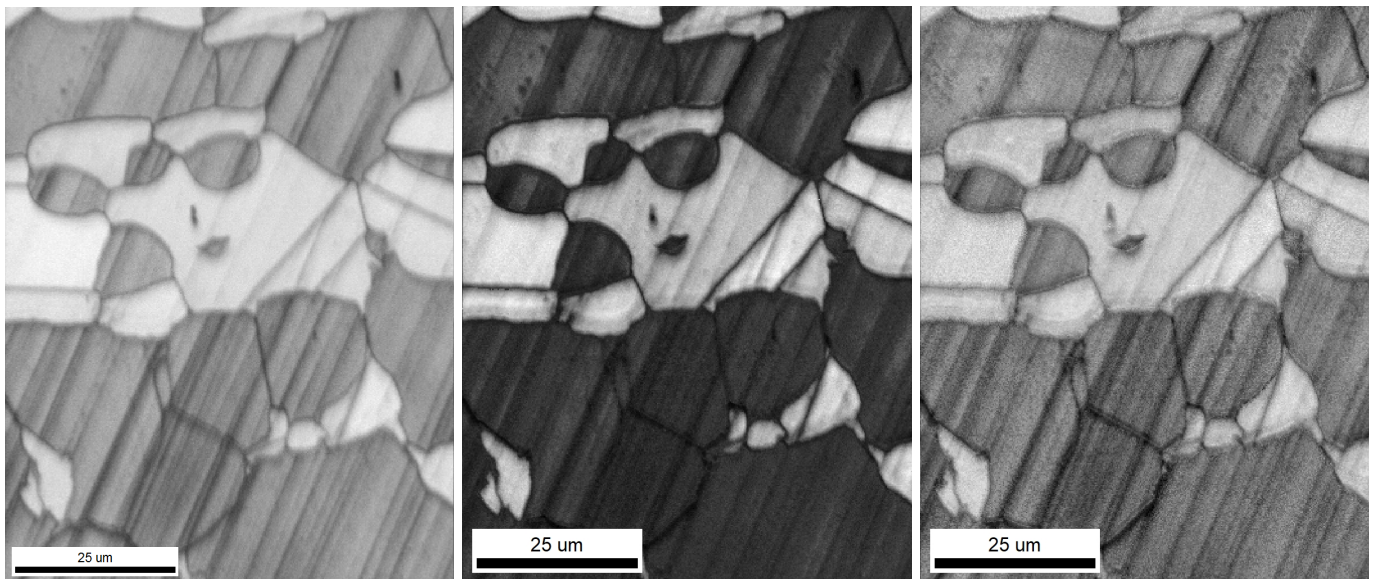
Phase \ Fraction,%	HI [8]	DI $[\text{SDH}_{1/8}\text{A}_5\text{G}]$	DI $[\text{SDH}_{1/8}\text{A}_1\text{G}]$
Ferrite (α)	63.9	13.7	64.2
Austenite (γ)	35.1	31.9	35.8
Sigma (σ)	0.7	0.0	0.0
Chi (χ)	0.3	54.4	0.0

(a) PM, HI [8] (b) PM, DI [SDH$_{1/8}$A$_5$G] (c) PM, DI [SDH$_{1/8}$A$_1$G]

Figure 4.7: PM for the transition zone of WAAM1, electropolished

(a) IQ map, HI [8] (b) CI map, DI [SDH$_{1/8}$A$_5$G] (c) CI map, DI [SDH$_{1/8}$A$_1$G]

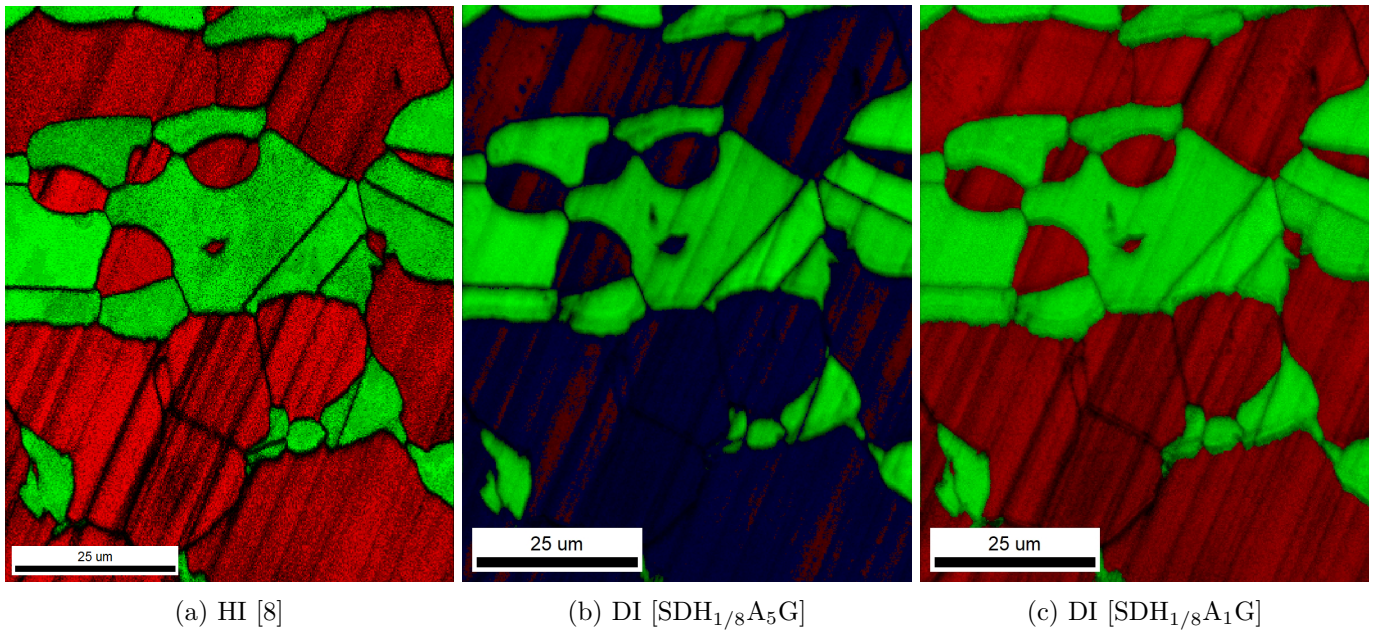Figure 4.8: IQ or CI maps for the transition zone of WAAM1, electropolished

(a) HI [8]   (b) DI [SDH$_{1/8}$A$_5$G]   (c) DI [SDH$_{1/8}$A$_1$G]

Figure 4.9: Phase maps with the CI value overlaid for the transition zone of WAAM1, electropolished

(a) IPF map, HI   (b) IPF map, DI [SDH$_{1/8}$A$_5$G]   (c) IPF map, DI [SDH$_{1/8}$A$_1$G]
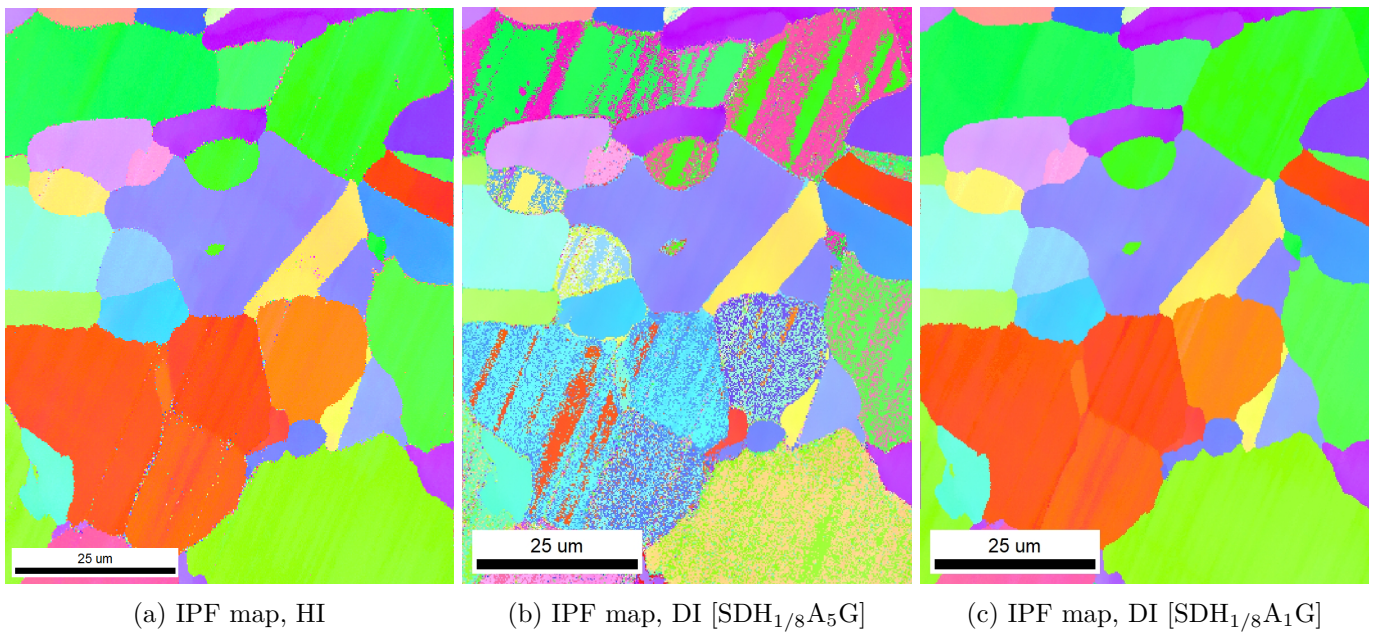
Figure 4.10: IPF maps for the transition zone of WAAM1, electropolished

(a) [SD]   (b) [SDHA], $n = 1$ (c) [SDHA], $n = 5$ (d) sim.pat γ
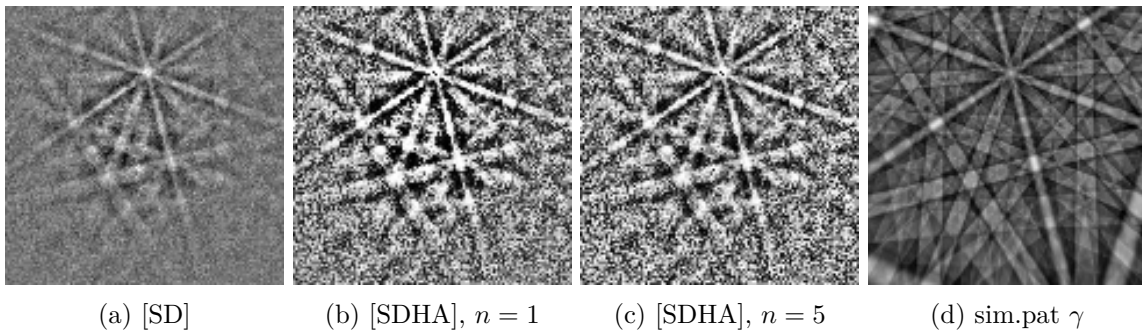
Figure 4.11: Pattern indexed as γ for both $n = 1$ and $n = 5$. In a), b) and c) the experimental pattern is shown for different pattern processing recipes. In d) the simulated pattern of best match for γ is shown
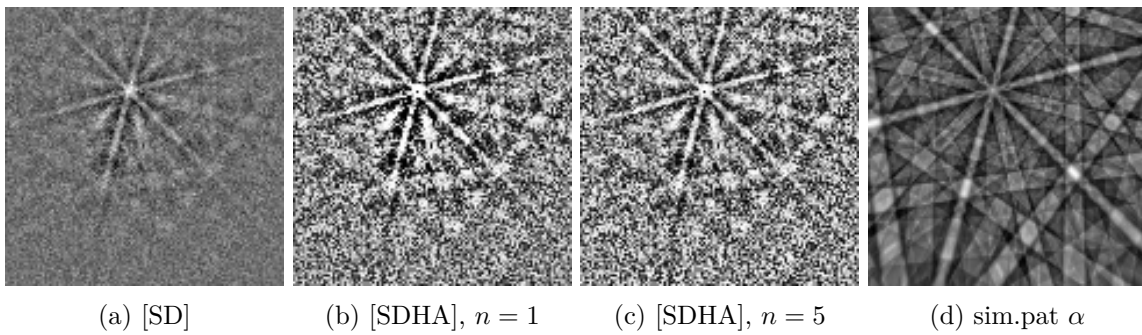

(a) [SD]   (b) [SDHA], $n = 1$ (c) [SDHA], $n = 5$ (d) sim.pat α

Figure 4.12: Pattern indexed as α for both $n = 1$ and $n = 5$. In a), b) and c) the experimental pattern is shown for different pattern processing recipes. In d) the simulated pattern of best match for α is shown

(a) [SD]   (b) [SDHA], $n = 1$ (c) [SDHA], $n = 5$

(d) sim.pat α (e) sim.pat χ

Figure 4.13: Pattern indexed as α for $n = 1$ but as χ for $n = 5$. In a), b) and c) the experimental pattern is shown for different pattern processing recipes. In d) and e) the simulated patterns of best match for α and χ are shown respectively
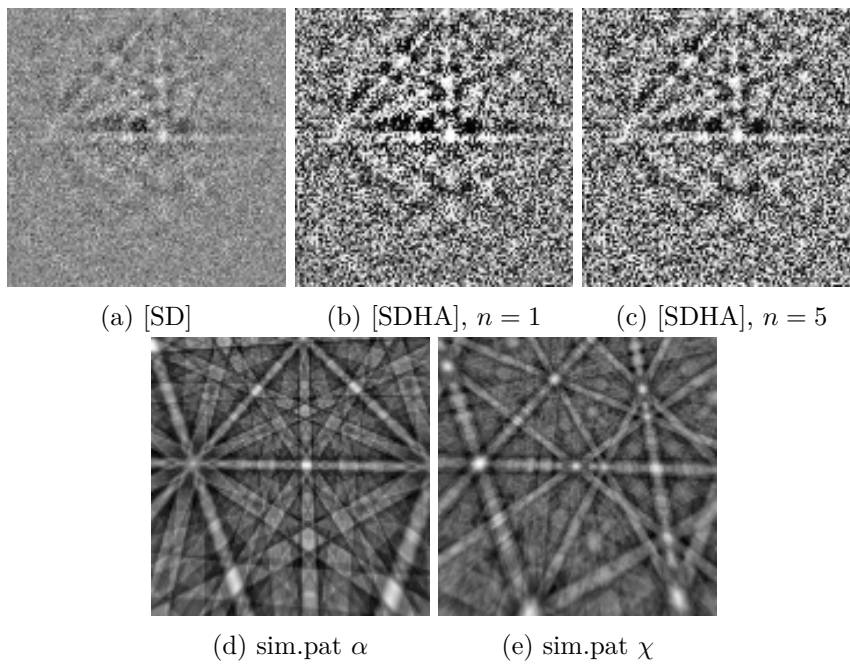
4.1.3 Electron Backscatter Images of WAAM1

The WAAM1 sample was not studied using Electron Backscatter Images (BEI) in the specialization project [8]. Although no σ or χ-phase was found in the sample regions studied with EBSD, other regions might contain them. In Figure 4.14 are BEIs of the WAAM1 sample shown. The regions shown in the images are believed to contain σ-phase in the bright zones present in the images, as this is seen in previous works [5, 7, 26].
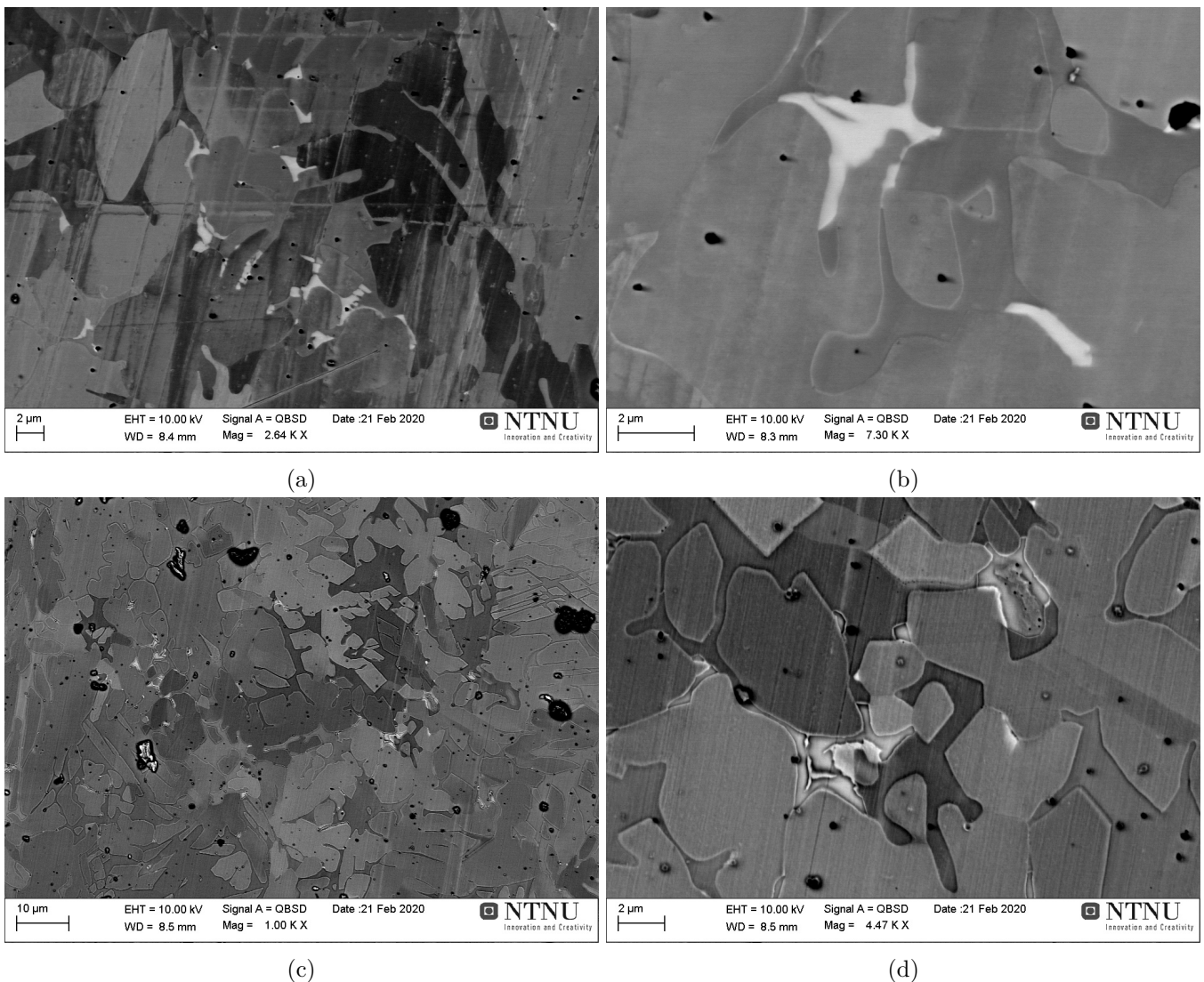

Figure 4.14: Electron backscatter images from the WAAM1 sample. Image a) and b) are from one of the intermediate weld wires located in the *middle sample*. The surface of the sample is polished down to 1 μm. Image c) and d) are from the 15th wire located in the *upper sample*. The sample has an electropolished surface

4.2 Characterization of WAAM2

As the WAAM1 sample, based on the EBSD and BEI result, probably only contained a low fraction of σ-phase and no evidence of χ-phase, the WAAM2 sample was next to be studied. The obtained results from optical microscopy, backscatter electron images, EPMA and EBSD are presented here.

4.2.1 Optical Microscopy of WAAM2

As for the WAAM1 sample, optical microscopy was first used to get an overview of the microstructure in the WAAM2 sample. Various regions were studied and in Figure 4.15 images from six regions in the sample are shown. In Figure 4.16 images from two of the regions presented in Figure 4.15 are shown, having increased magnification. In Figure 4.16a, showing the HAZ of the base plate, chromium nitrides are believed to be present in the structure. Multiple pits are observed in the α-grains and some of the grain boundaries appear different in this image compared to the grain boundaries seen in the image of the base plate. In Figure 4.16b, showing the 8th weld wire, σ-phase is believed to be present. Dark features appear along the grain boundaries for the 8th and 15th weld wires, which are not seen in the base plate. The appearance of the chromium nitride and σ-phase zones also match the reference images given in the electropolishing guide used.

(a) Base plate

(b) HAZ of the base plate

(c) Transition zone

(d) 1st weld wire

(e) 8th weld wire
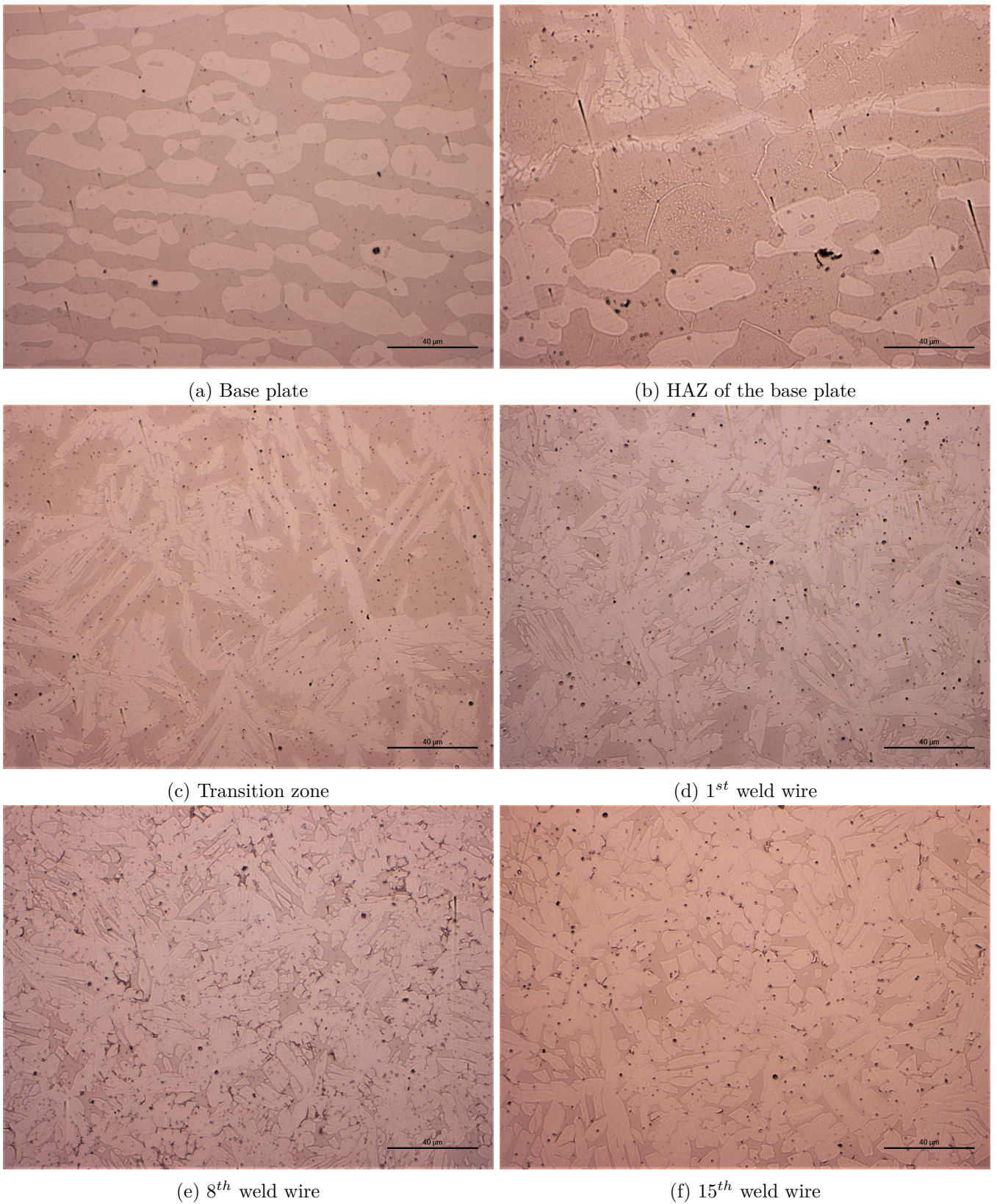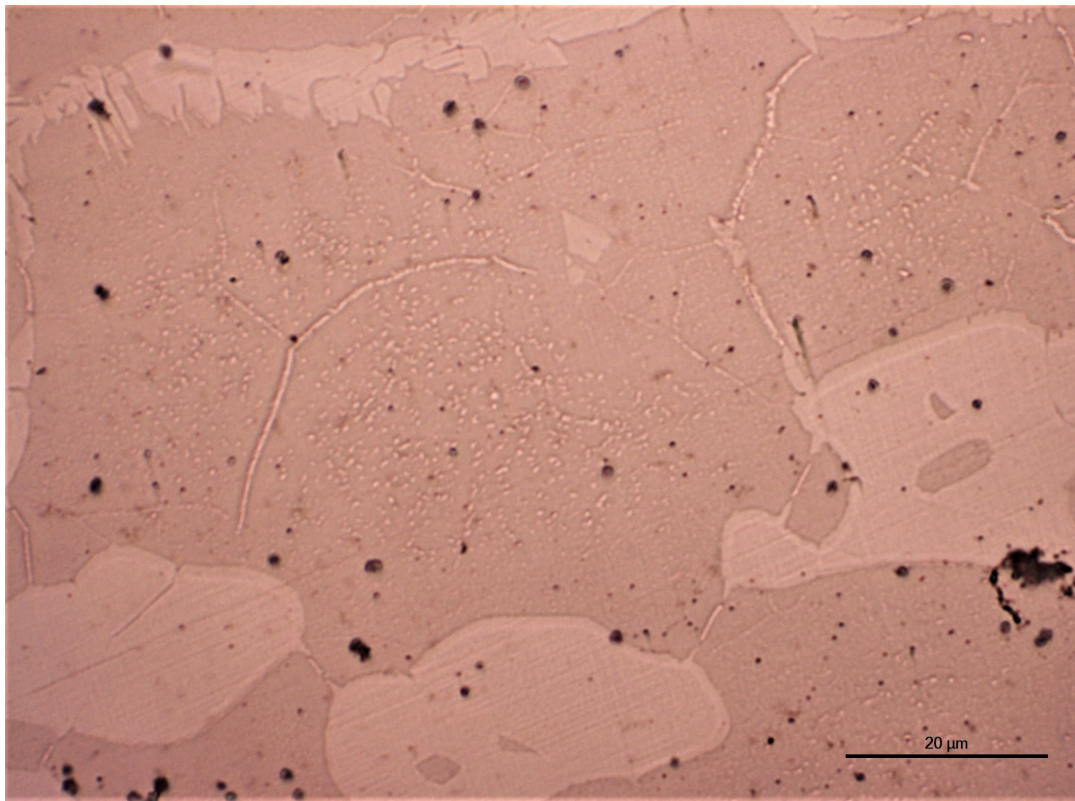

(f) 15th weld wire

Figure 4.15: Optical micrographs from various zones in the WAAM2 sample. All scale bars are 40 μm
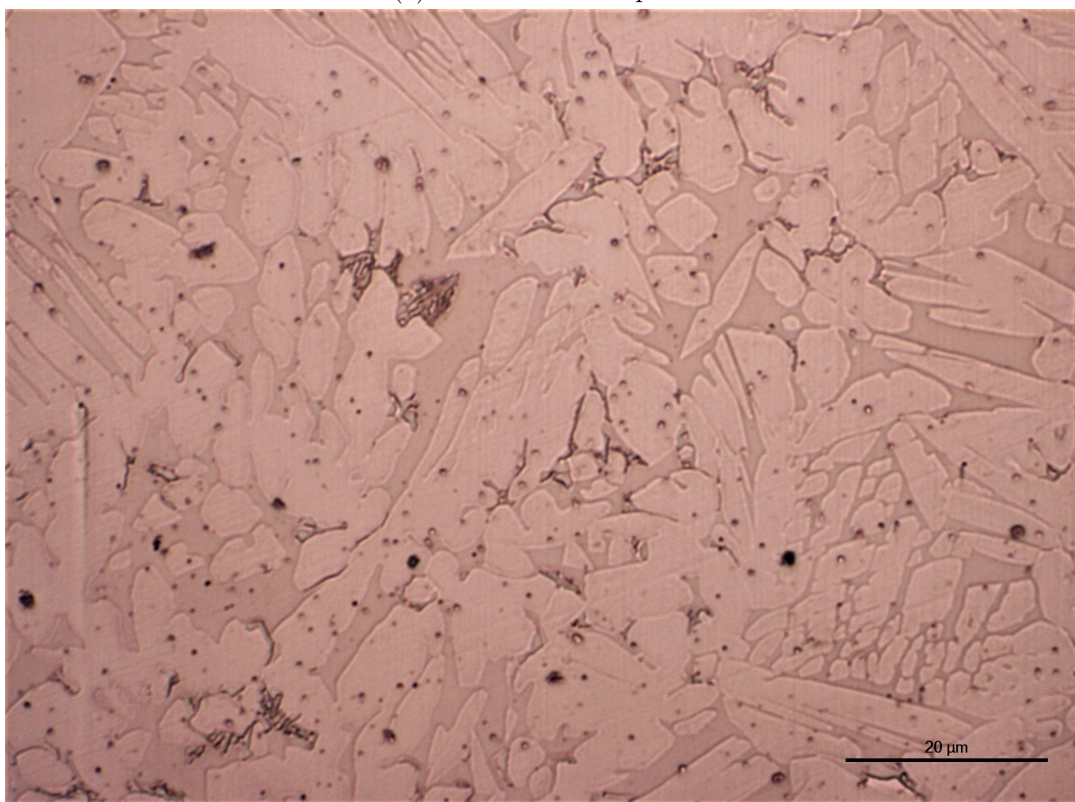
(a) HAZ of the base plate

(b) 8th weld wire

Figure 4.16: Optical micrographs from zones where secondary phases have been formed. a) chromium nitrides, b) intermetallic phases

4.2.2   BEI, EPMA and HI Phase Map, 8th Weld Wire

To further characterize the WAAM2 sample, SEM/EBSD and EPMA were used. An area in the 8th weld wire was examined using EBSD, backscatter electron imaging and EPMA. In Figure 4.17 both the BEI of the region and the phase map from HI are shown. The EBSD pattern file contains 997x1018 patterns (99.7x101.8 μm area size).

In Figure 4.18 the EPMA area measurement of the lower-left area in Figure 4.17a is shown. The measurement for Cr, Ni and Mo, and the BEI of the corresponding area are included. With respect to the BEI, some point intensity measurements for Mo were performed. In Table 4.4 intensity values for three areas are given. The brightest areas, believed to be χ-phase, gets the highest intensity values, despite being too small to completely cover the interaction volume of the incident beam. The sub-bright area measured, believed to be σ-phase, gets a lower value compared to the brightest regions in the BEI, but the intensity value is higher than in the phase appearing dark in the BEI. The dark phase is either α or γ-phase.
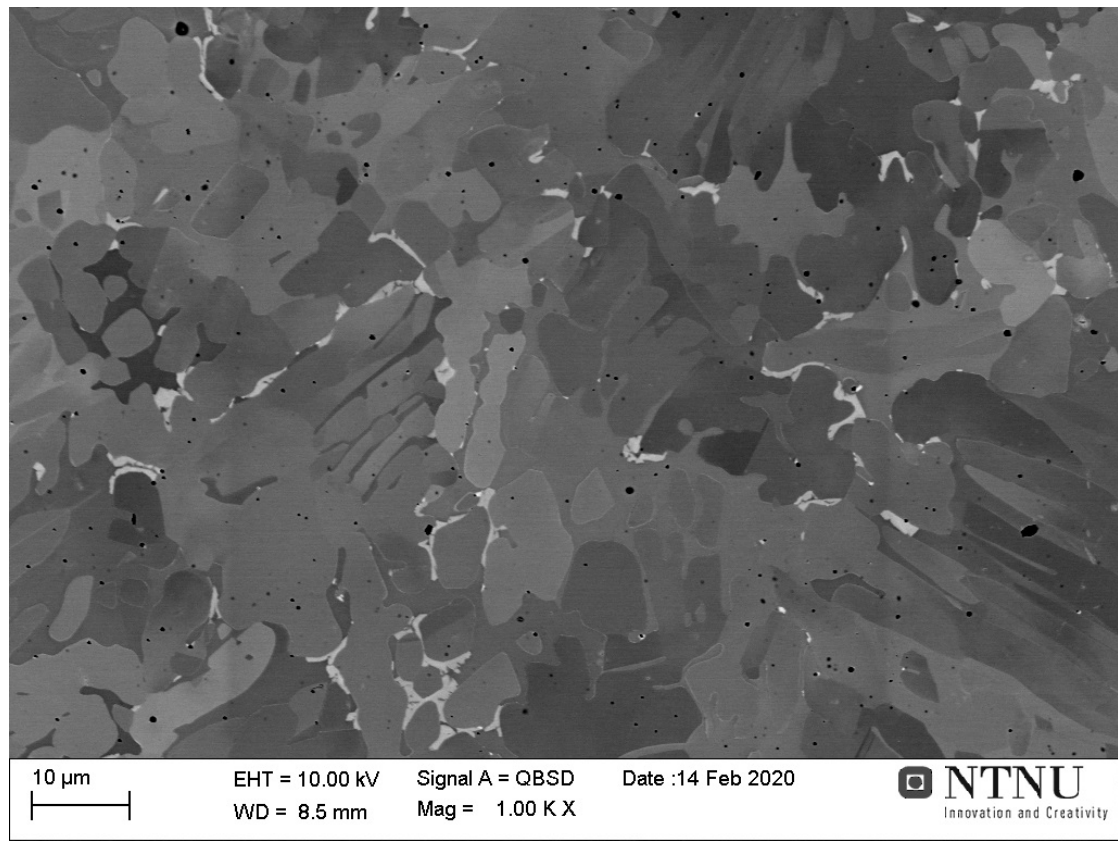
(a) Backscatter electron image
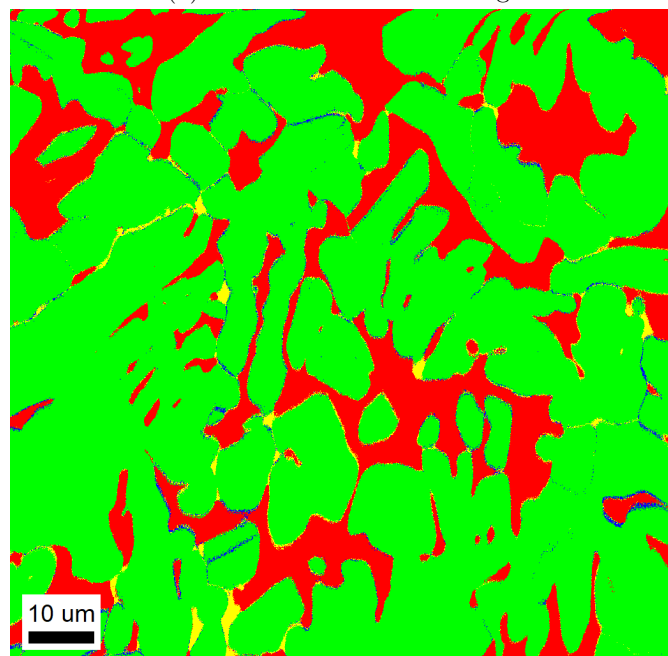
(b) Phase map, HI

Figure 4.17: The region in the 8th weld wire of WAAM2 examined. a) Backscatter electron image, b) EBSD phase map from HI
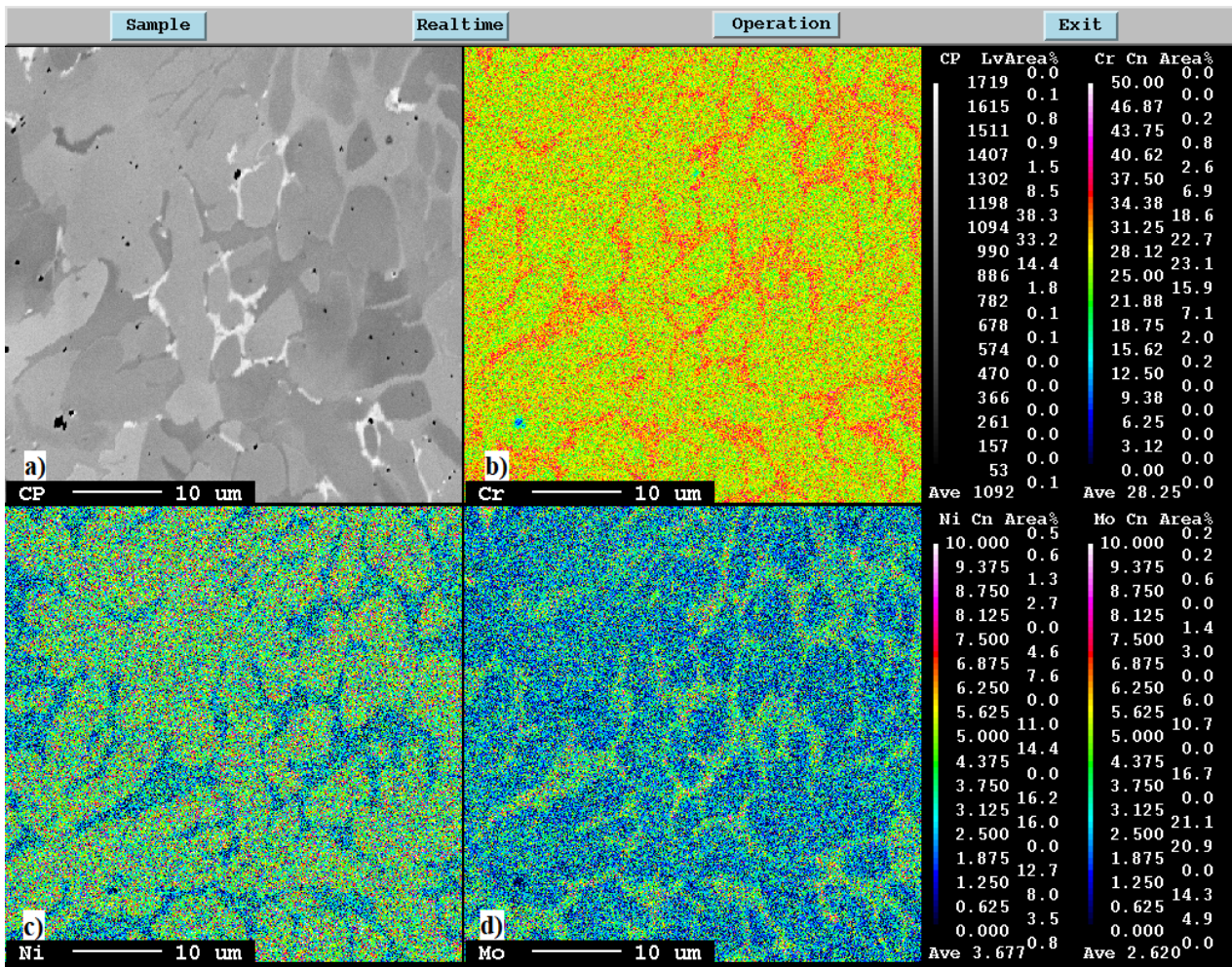
Figure 4.18: EPMA measurement of the 8th weld wire in the WAAM2 sample. a) Backscatter electron image, b) Chromium measurement, c) Nickel measurement, d) Molybdenum measurement

Table 4.4: Point measurements of the characteristic X-ray intensity of molybdenum performed on different phases observed in the backscatter electron image. The mean value and standard deviation (STD) are also given

Phases	Brightest phase (χ)*	Sub-bright phase (σ)	Dark phase $(\alpha$ or $\gamma)$
	510.0	252.7	140.1
	524.8	242.2	148.4
Intensity [#counts]	511.8	252.8	140.1
	499.2	260.3	148.9
	469.0	259.3	145.7
Mean value	503.0	253.5	144.6
STD	21.05	7.223	4.319

* The size of the brightest particles were too small to completely cover the interaction volume of the incident beam themselves. The measured intensity values thus have contribution from the surrounding phases

4.2.3   Pattern Processing Tuning, 8th Weld Wire

When moving on to the dictionary indexing of the acquired pattern file, it was necessary to do more testing with respect to the AHE n-parameter. However, performing multiple indexing runs on the whole pattern file would be too time consuming. Therefore, an area in the lower-left corner of the pattern file was cropped out. In Figure 4.19 IQ, phase and IPF maps from HI of the cropped area are shown. A BEI of the area is also included. The cropped pattern file contains 186x139 patterns (18.6x13.9 μm). Dictionary indexing runs when applying a [SDHAG] pattern processing recipe were executed. The cropped area was indexed six times using $n = 1 - 5$ and 10. $w = 1/8$ was used for all runs. In Figure 4.20 phase and IPF maps for DI using $n = 1 - 3$ and 5 are shown. In Table 4.5 the phase fraction from the six DI runs are given.

To further study the results of the six dictionary indexing runs, the dot product data for each phase was examined. In Figure 4.21 the dot product data is plotted as a function of the n-value for each phase. The mean, maximum and minimum DP data is plotted. The data is based on the pixels each phase gets the best match for only. This means there are no data for the χ-phase for $n = 1$ and 2 as χ does not get indexed for any pixel for these cases. In Figure 4.22 the minimum overall dot product data for each phase is plotted as a function of the n-value. The minimum overall DP data is the lowest DP value each phase gets when looking at all the patterns in the pattern file. In Figure 4.23 to 4.26 four pattern examples are presented.
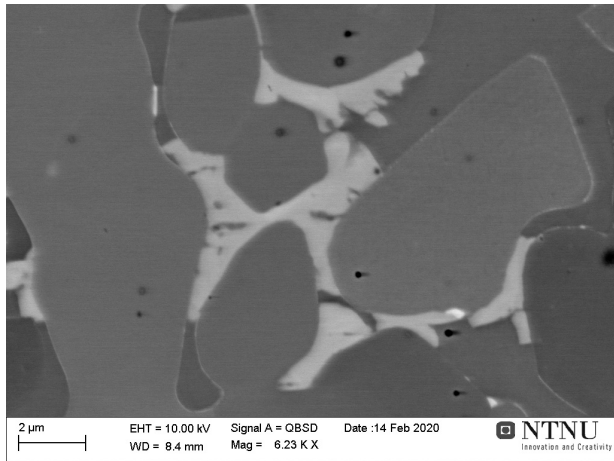
(a) Backscatter Electron Image
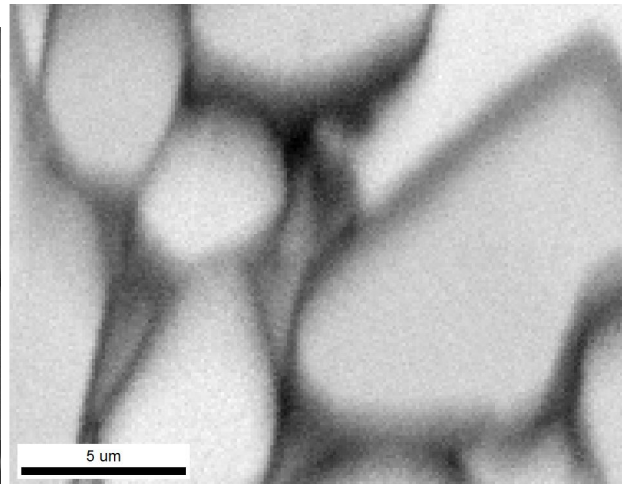
(b) IQ map, HI
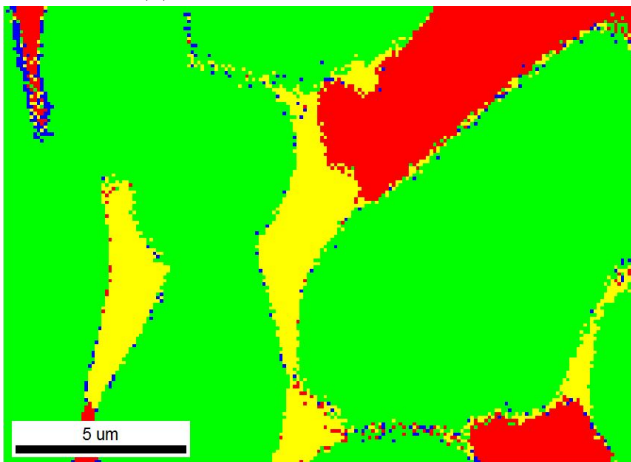
(c) Phase map, HI
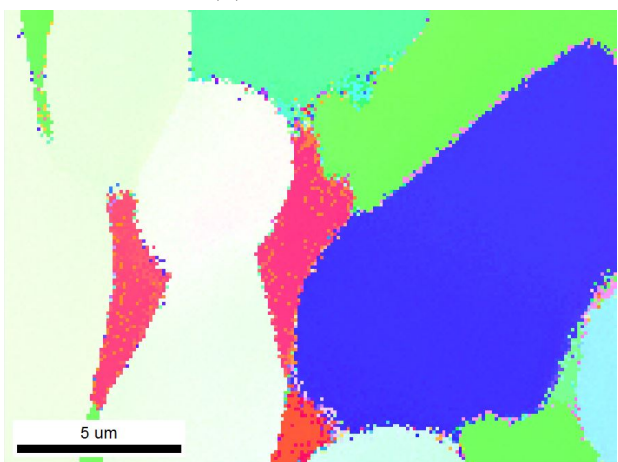
(d) IPF map, HI

Figure 4.19: BEI and EBSD maps from HI of the cropped region
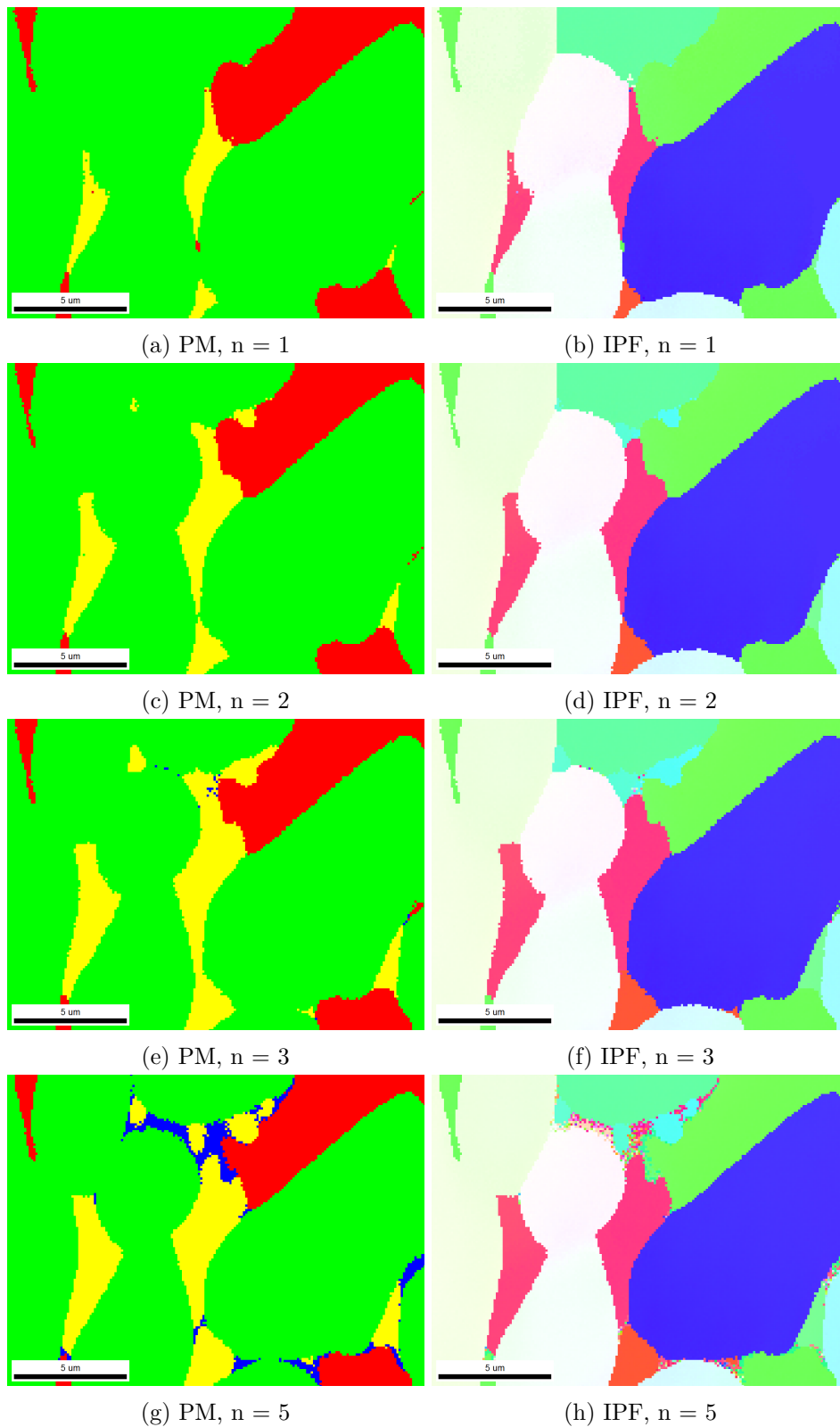
(a) PM, n = 1

(b) IPF, n = 1

(c) PM, n = 2

(d) IPF, n = 2

(e) PM, n = 3

(f) IPF, n = 3

(g) PM, n = 5

(h) IPF, n = 5

Figure 4.20: Phase and IPF maps from DI for multiple indexing runs of the same pattern file. A [SDHAG] pattern processing recipe is used, where $w = 0.125$ is applied for all indexing runs. The resulting maps from using $n = 1, 2, 3$ and 5 are presented here

Table 4.5: Phase fractions for the cropped pattern file of the 8th wire, WAAM2. Resulting phase fractions for various applied pattern processing are given. The indexing runs are differing in the n-value used only

n-value	Ferrite (α), %	Austenite (γ), %	Sigma (σ), %	Chi (χ), %
1	13.81	82.38	3.81	0.00
2	12.82	79.79	7.48	0.00
3	12.59	76.63	10.70	0.09
4	12.20	74.83	11.52	1.45
5	11.96	73.94	11.25	2.85
10	11.62	72.98	11.15	4.25

(a) Ferrite (α)

(b) Austenite (γ)

(c) Sigma (σ)

(d) Chi (χ)
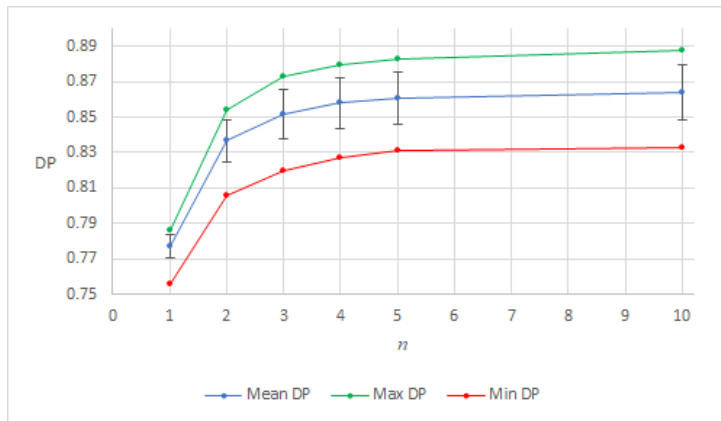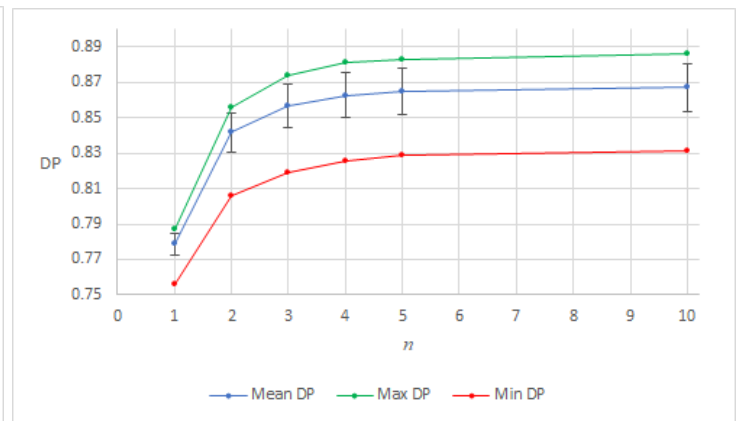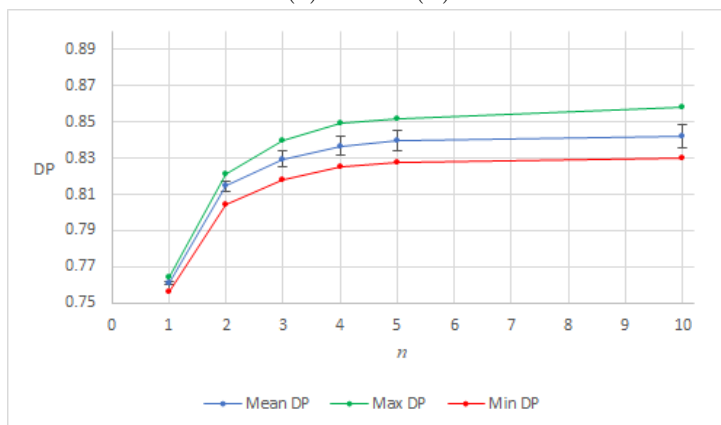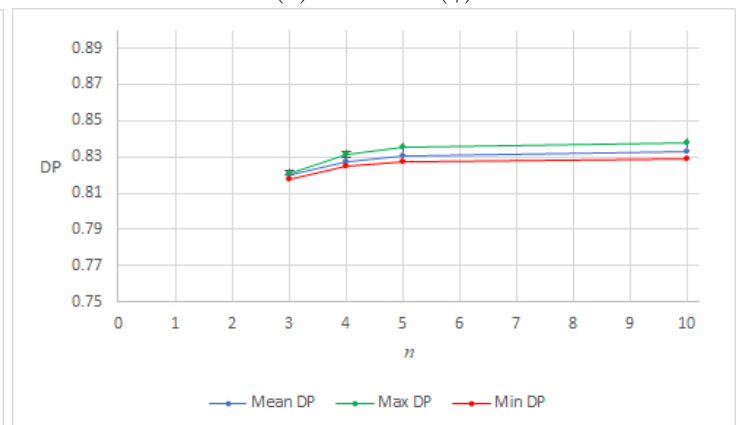
Figure 4.21: The dot product data for each phase plotted against the n-value. The mean, maximum and minimum DP-values for each of the four phases are shown. The data are from the pixels each of the phases got indexed for only
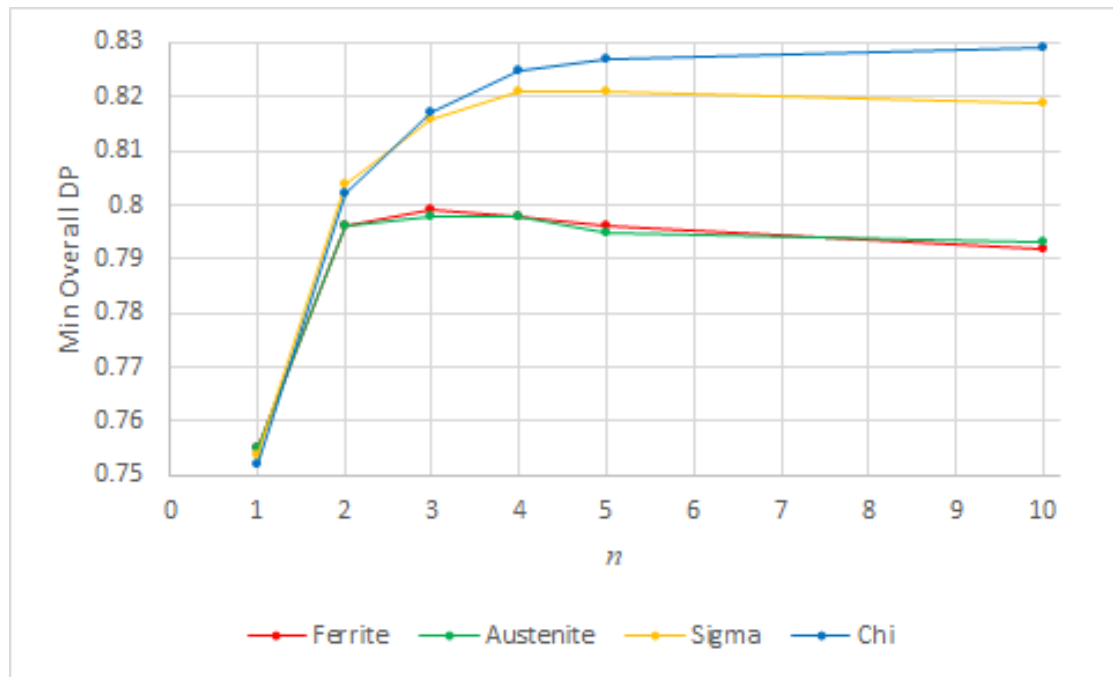
Figure 4.22: The minimum overall dot product value for each phase plotted against the AHE n-value

(a) [SD]   (b) [SDHA], $n = 2$ (c) sim.pat σ
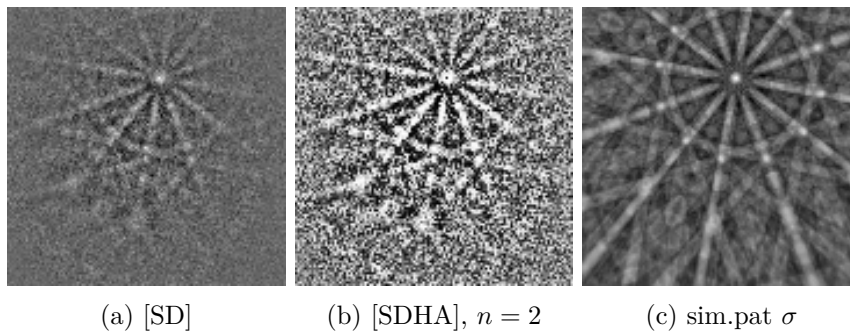
Figure 4.23: Pattern indexed as σ for $n = 1 - 5$. In a) and b) the experimental pattern is shown for different pattern processing recipes. In c) the simulated pattern of best match for σ is shown

(a) [SD]   (b) [SDHA], $n = 2$ (c) sim.pat γ (d) sim.pat σ
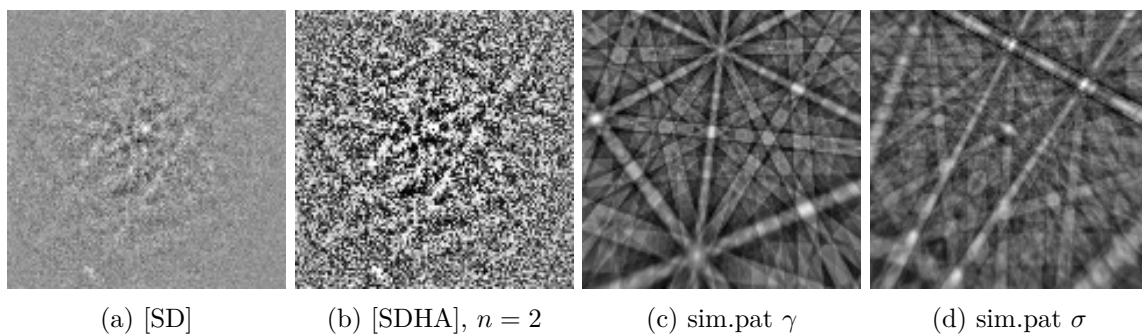
Figure 4.24: Pattern indexed as γ for $n = 1$ but as σ for $n = 2$. In a) and b) the experimental pattern is shown for different pattern processing recipes. In c) and d) the simulated patterns of best match for γ and σ are shown respectively

(a) [SD]   (b) [SDHA], $n = 2$

(c) sim.pat α (d) sim.pat σ (e) sim.pat γ
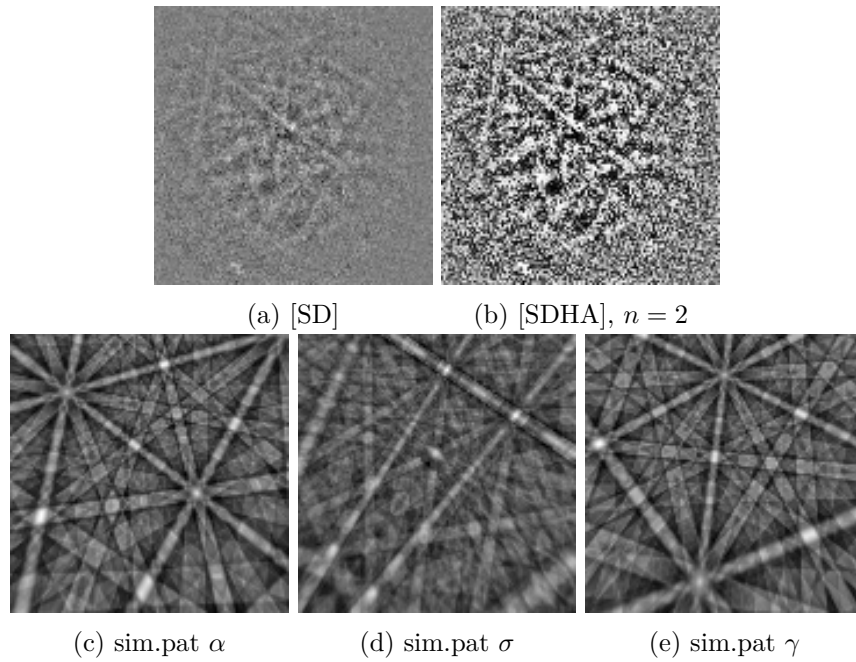
Figure 4.25: Pattern indexed as α for $n = 1$ and 2, but as σ for $n = 3$. In a) and b) the experimental pattern is shown for different pattern processing recipes. In c), d) and e) the simulated patterns of best match for α, σ and γ are shown respectively

(a) [SD]   (b) [SDHA], $n = 2$

(c) sim.pat γ (d) sim.pat σ (e) sim.pat χ
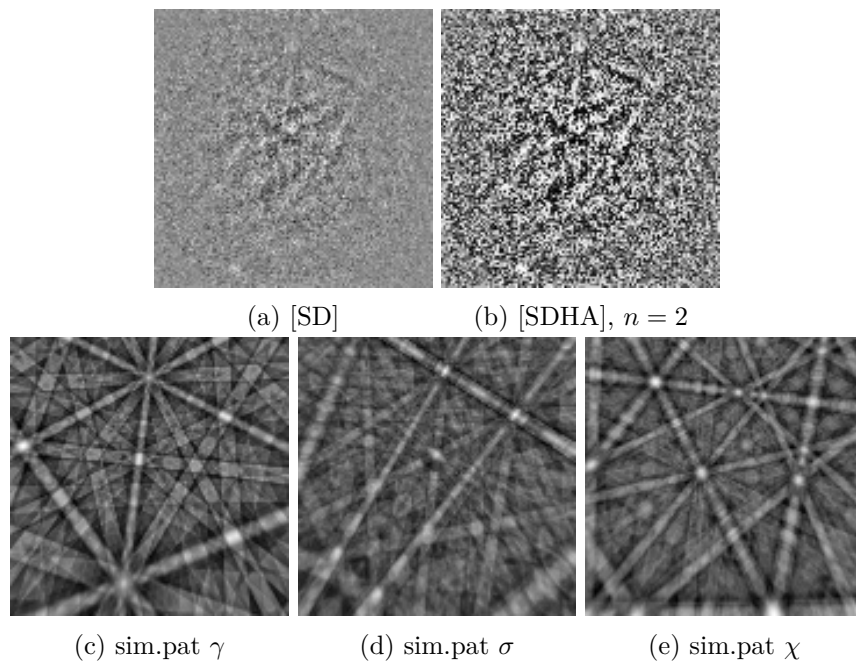
Figure 4.26: Pattern indexed as γ for $n = 1$, as σ for $n = 2$ and as χ for $n = 3$. In a) and b) the experimental pattern is shown for different pattern processing recipes. In c), d) and e) the simulated patterns of best match for γ, σ and χ are shown respectively

4.2.4   Comparison of HI and DI, 8th Weld Wire

To compare how the Hough indexing and dictionary indexing approaches perform, various EBSD maps from each approach are presented and compared here. The maps are from the 997x1018 pattern file of the WAAM2 sample. For the DI two pattern processing recipes have been used, where $n = 2$ and 3 were applied. $w = 1/8$ is used for both cases. In Table 4.6 the phase fractions from HI and DI are given. In Figure 4.27 the BEI of the ROI is shown. The EBSD maps are presented in Figure 4.28 and 4.29.

Table 4.6: Phase fractions of the pattern file from the WAAM2 sample. Phase fractions from HI and DI are presented. For DI, $n = 2$ and $n = 3$ have been used for the indexing. However, when indexing using $n = 3$, χ was not included

Index approach	Ferrite (α), %	Austenite (γ), %	Sigma (σ), %	Chi (χ), %
HI	22.8	74.2	1.9	1.1
DI, $n = 2$	20.4	79.3	0.3	0.0
DI, $n = 3$	23.6	75.4	1.0	N/A
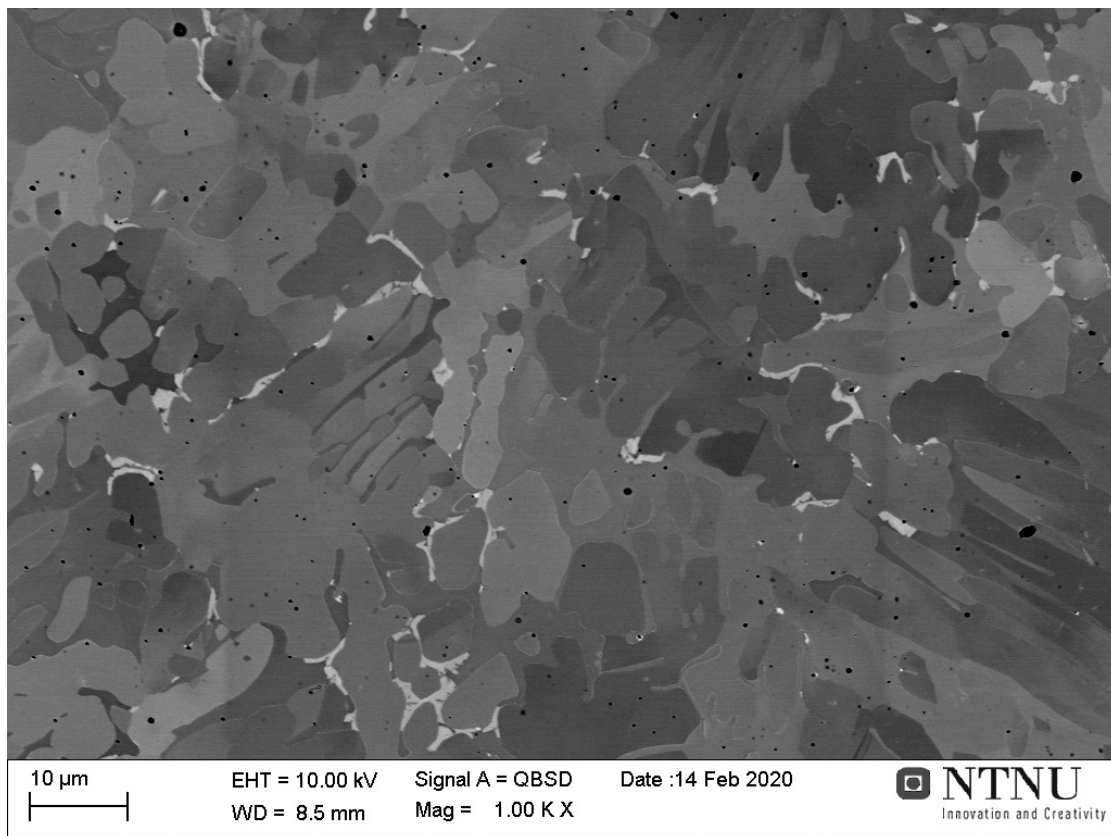
Figure 4.27: Backscatter electron image of the region studied with EBSD

(a) PM, HI

(b) HI

(c) PM, DI ($n = 2$)

(d) DI ($n = 2$)

(e) PM, DI ($n = 3$)

(f) DI ($n = 3$)
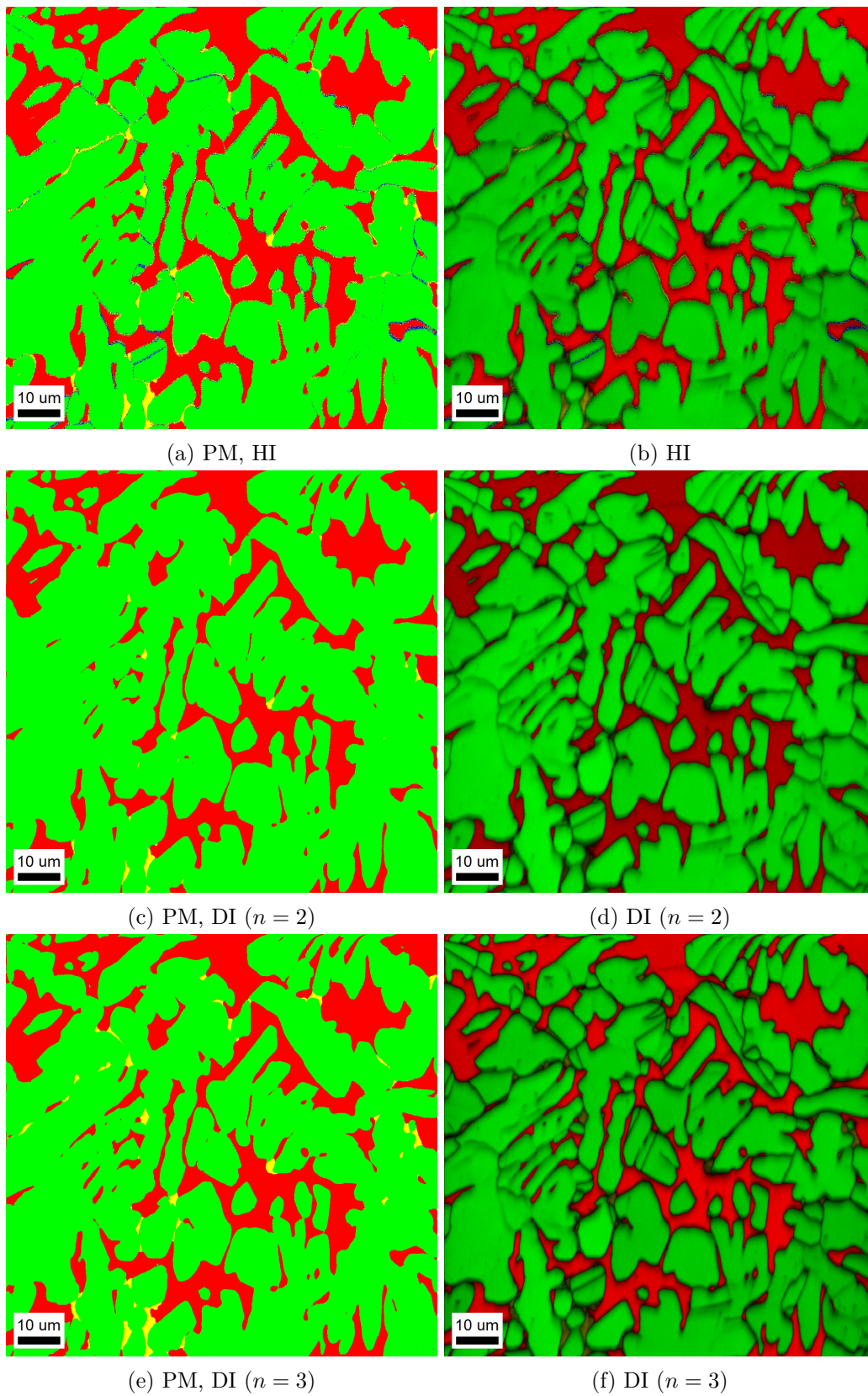
Figure 4.28: Left column showing phase maps and right column showing phase maps with CI overlaid for the WAAM2 sample. a, b) maps from HI, c, d) maps from DI ($n = 2$) and e, f) maps from DI ($n = 3$)

58

(a) IPF map, HI

(b) IQ map, HI

(c) IPF map, DI ($n = 2$)

(d) CI map, DI ($n = 2$)

(e) IPF map, DI ($n = 3$)

(f) CI map, DI ($n = 3$)
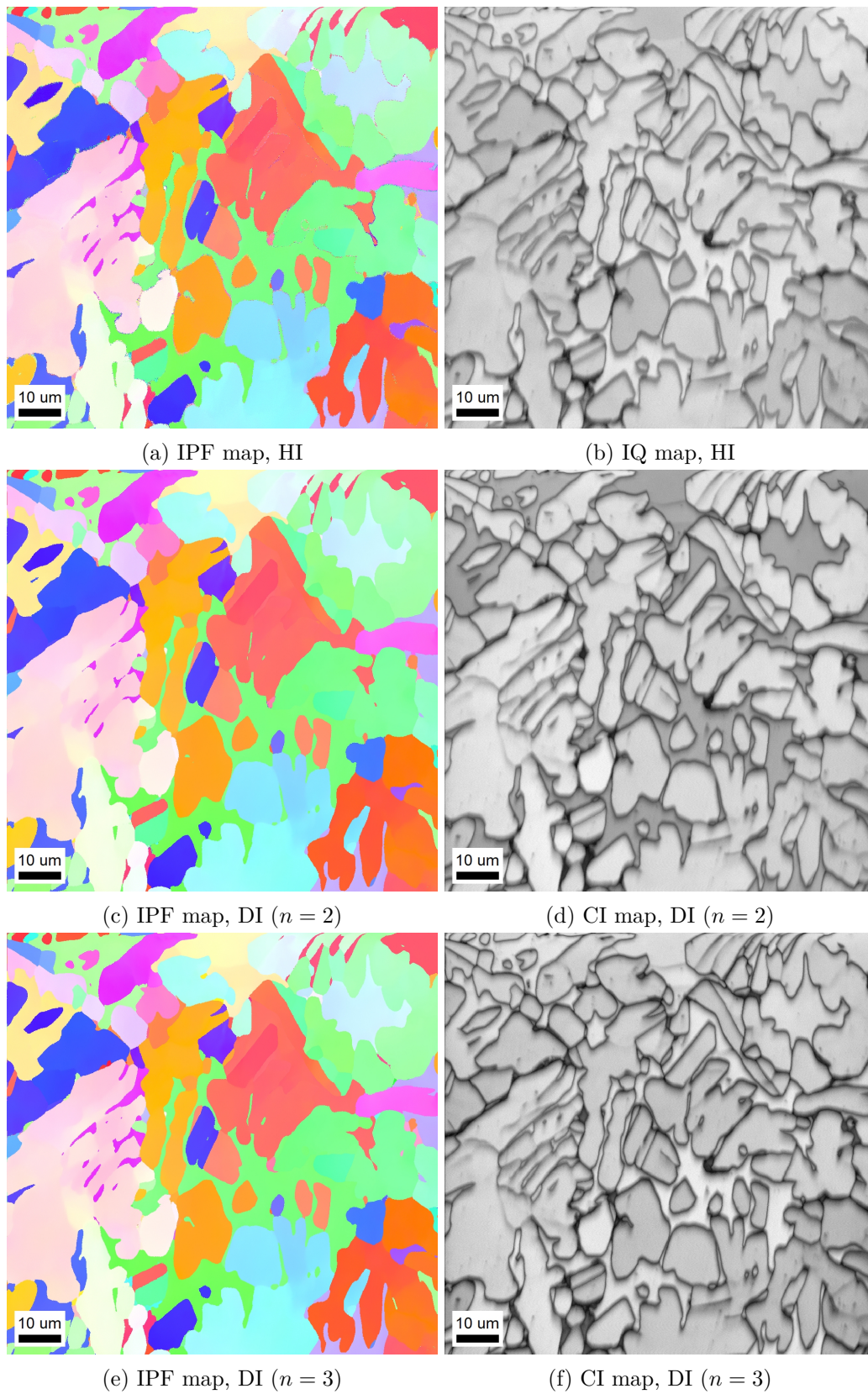
Figure 4.29: Left column showing IPF maps and right column showing pattern quality maps for the WAAM2 sample. a, b) maps from HI, c, d) maps from DI ($n = 2$) and e, f) maps from DI ($n = 3$)

59

4.2.5   Characterization of the HAZ, WAAM2

When studying the HAZ of the base plate in the optical microscope, what seemed to look like chromium nitrides were observed. This region was therefore further studied using backscatter electron imaging and EBSD. In Figure 4.30 two BEIs of the HAZ are shown. The same region shown in Figure 4.30b was further studied using EBSD. In Figure 4.31 the IQ and IPF maps from HI of the region are shown. No bmt file for any of the chromium nitride phases were available, therefore only α and γ were included in the indexing run. As the sample probably was not optimally prepared, larger particles where still present on the surface of the sample after the sample preparation. These particles cast shadows on the region studied (e.g. in the lower-right corner) and should be ignored. All the large grains observed in the IPF map are α-grains.
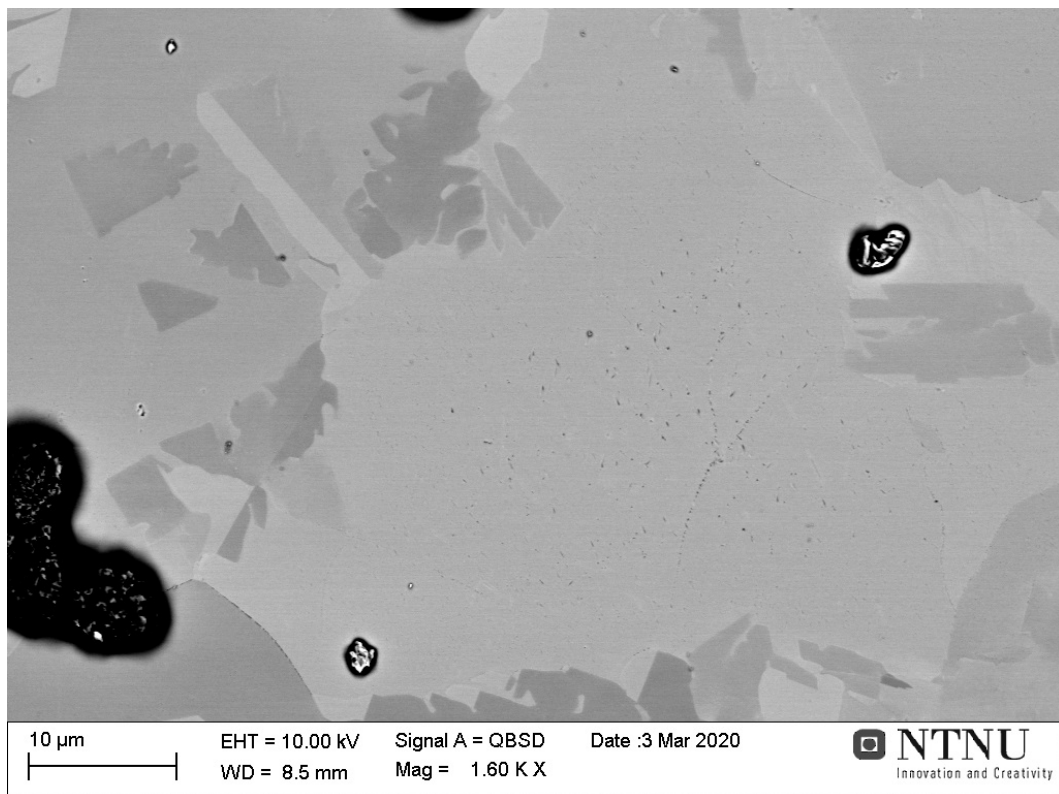
(a) BEI showing an overview of the micro structure
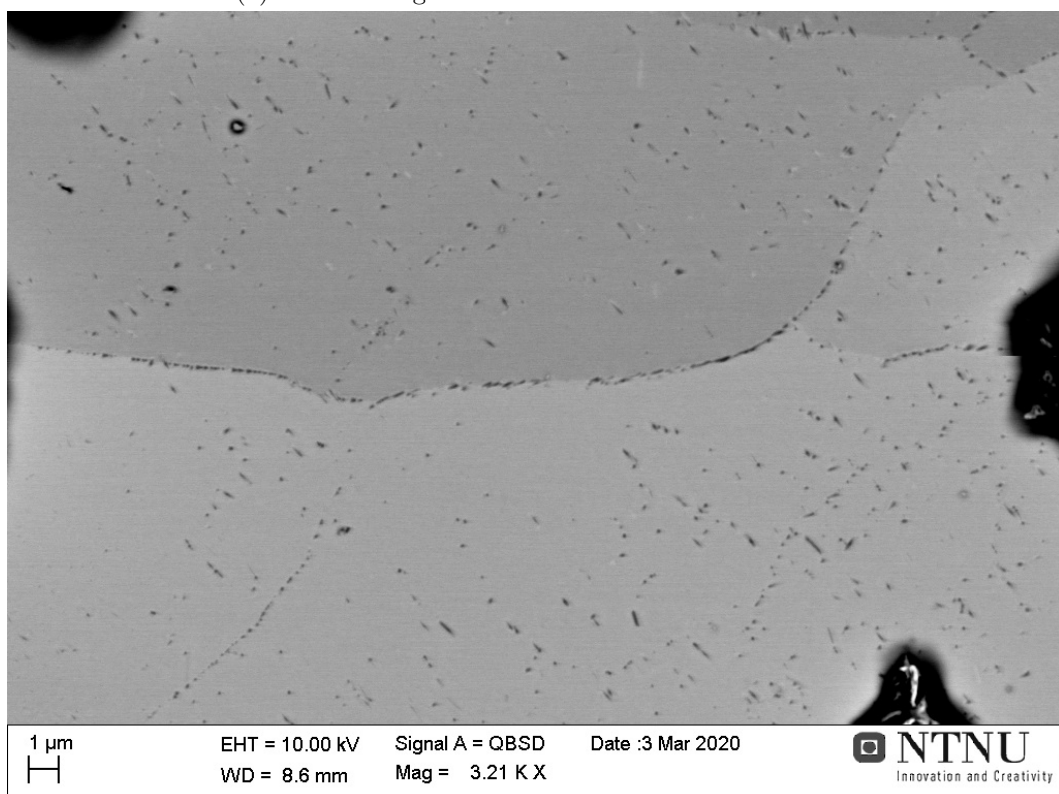
(b) BEI with increased magnification

Figure 4.30: Electron backscatter images showing the HAZ of WAAM2 for different magnifications
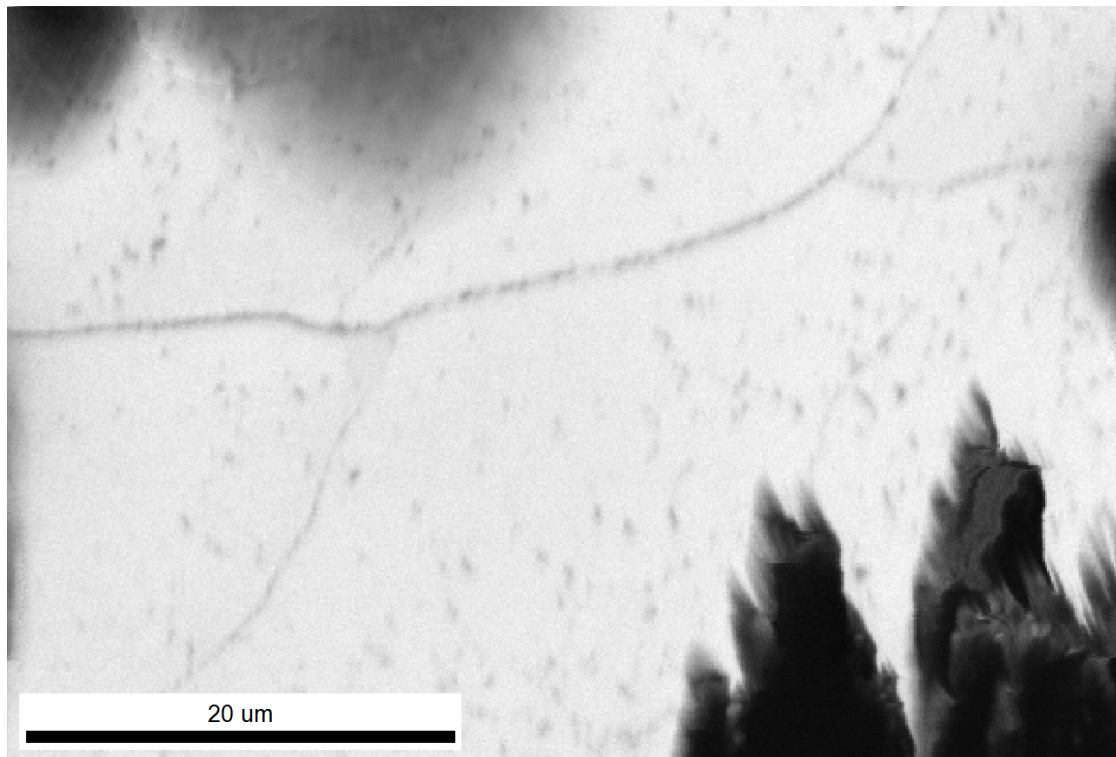
(a) IQ map, HI
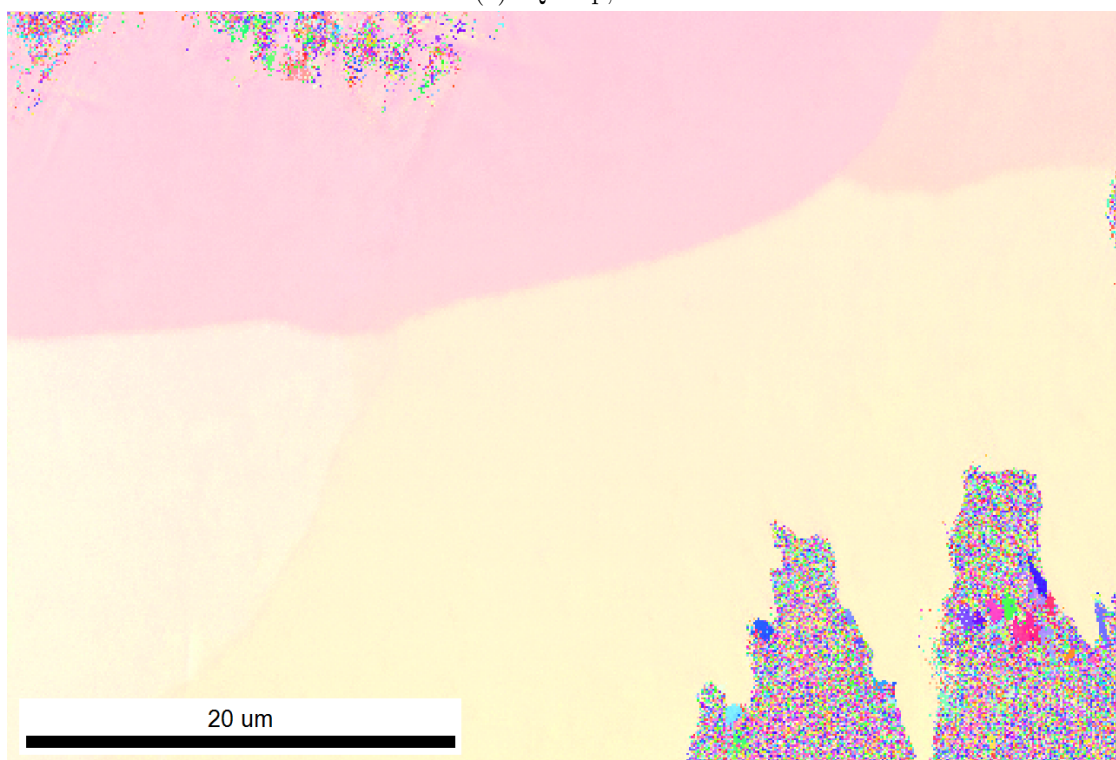
(b) IPF map, HI

Figure 4.31: IQ and IPF maps from HI of the same region of the HAZ shown in Figure 4.30b

4.3   Characterization of SD750C

As the WAAM2 sample did not contain any large χ-particles, it was necessary to make an effort in creating large χ-particles. As one of the target of this thesis is to examine which pattern processing recipe which is suitable for characterizing and quantification of χ, it was necessary to have a sample where EBSD patterns origin from χ were present. A SDSS sample was therefore heat treated in a way that potentially could lead to formation of χ-phase. In this section backscatter electron images and EPMA X-ray maps are first presented. Next, results from further pattern processing testing for DI are presented. Toward the end a comparison of the results from HI and DI is given.

4.3.1   BEIs and EPMA X-ray Maps

The SD750C sample was first examined using backscatter electron images and EPMA X-ray maps. This would give an indication in how the microstructure had evolved during the heat treatment. It was especially important to see if any potentially large χ-phase particles had been formed, which later could be examined with EBSD. In Figure 4.33 two BEIs are shown. The upper image gives an overview of the structure and the lower image is taken at a increased magnification. In Figure 4.32 EPMA X-ray maps for Mo, Cr and Ni are shown together with the BEI of the region. The EPMA characterization was performed at a region where bright particles and the characteristic lamellar structure were observed in the BEI.
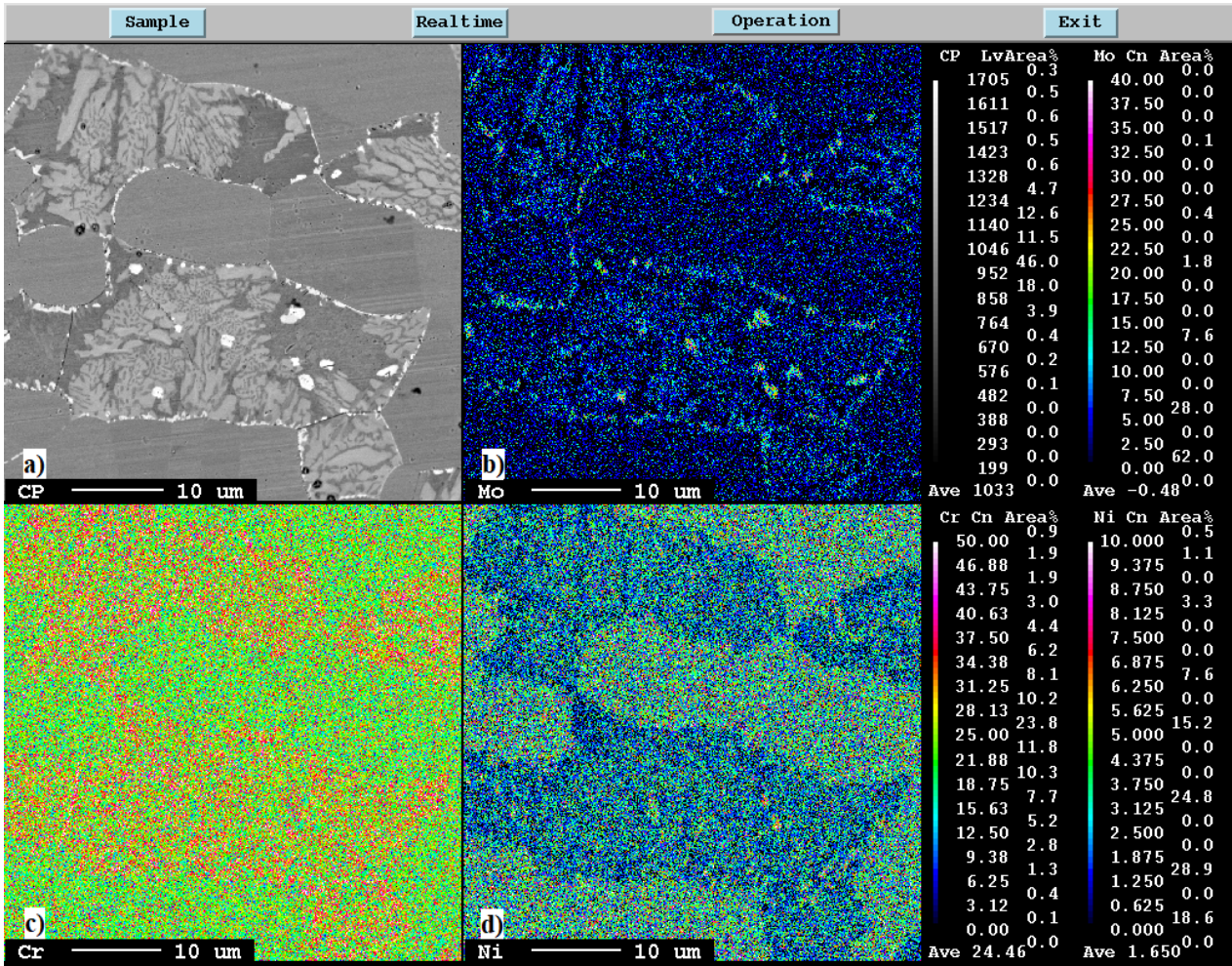
Figure 4.32: EPMA measurement of the the SD750C sample. a) Backscatter Electron Image, b) Molybdenum measurement, c) Chromium measurement, d) Nickel measurement
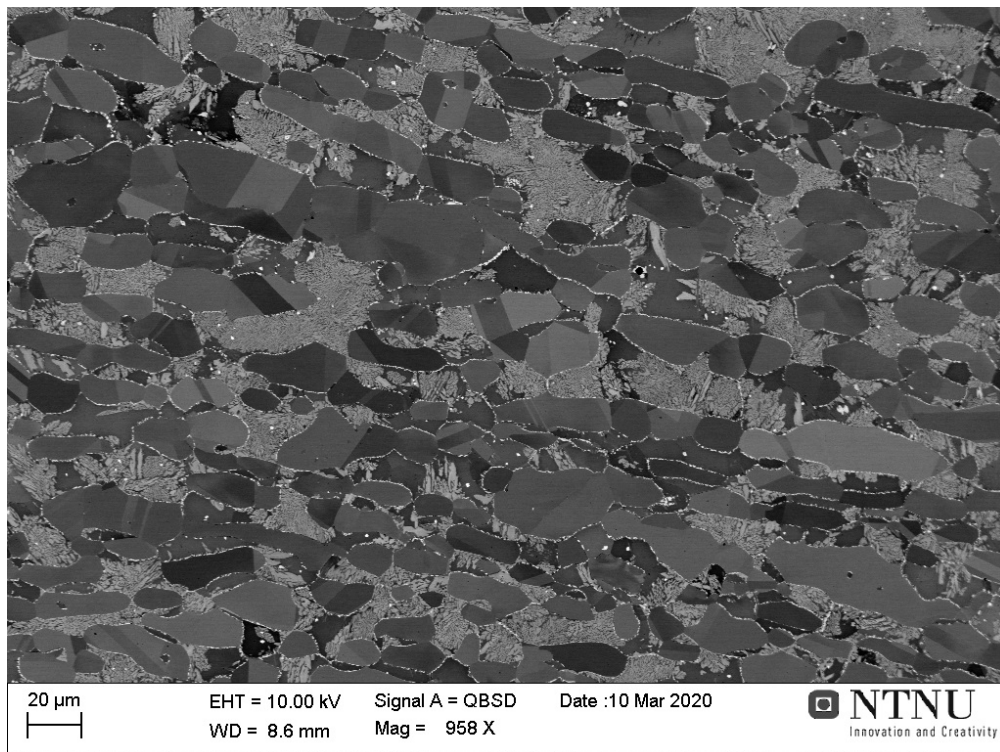
(a) BEI showing an overview of the micro structure
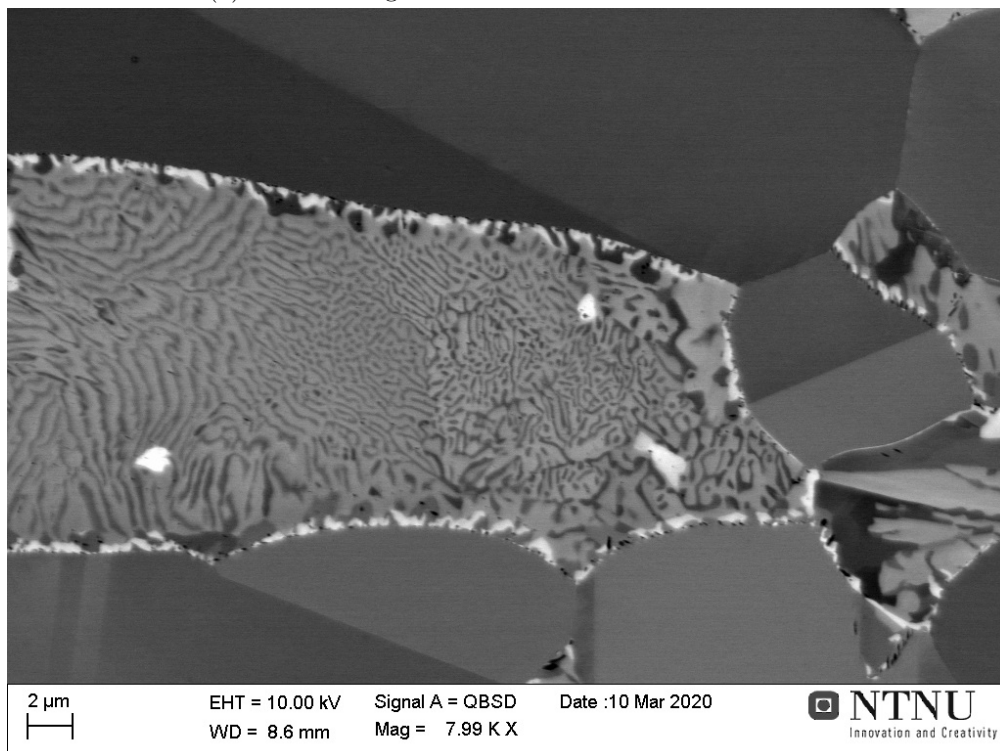
(b) BEI with increased magnification of a region with bright particles and a characteristic lamellar structure

Figure 4.33: Electron backscatter images of the SD750C sample of different magnifications

4.3.2 Tuning of the DI Pattern Processing Parameters, SD750C

A pattern file of 685 x 685 patterns (68.5 x 68.5 μm) was obtained when running EBSD pattern acquisition on the sample. The pattern file was first indexed using HI and a region of 100 x 100 patterns was cropped out from the larger file. The HI had indexed a relatively large χ-particle in this cropped region. In Figure 4.34 phase, IPF and IQ maps from HI of the cropped region are shown. The pattern intensity map and BEI of the region are also included.

Next, the 100 x 100 pattern file was indexed using DI. A [SDHAG] pattern processing recipe was applied using $w = 1/8$. The pattern file was indexed three times, where $n = 1, 2$ and 3 were applied. The obtained phase and IPF maps are presented in Figure 4.35. In Table 4.7 and 4.8 the phase fractions from HI and DI of the region are presented. In Figure 4.36 the minimum overall dot product values for each phase are presented, when applying $n = 1, 2$ and 3 for the DI.

To better see what effect the hi-pass parameter w may have on DI, the 100 x 100 pattern file was indexed seven times using different w-values. w-values from $1/64$ to 1 were used. $n = 2$ was used all the times. EMsoft version 4.3 was used for the DI this time. The obtained phase maps are shown in Figure 4.37, the phase fractions of each indexing run are presented in Table 4.9 and the minimum overall dot product values for each phase and for every indexing run are presented in Figure 4.38.

Since both EMsoft v.4.3 and v.5.0 were used, it could be usefully to see if there was any difference between the two versions. To study the difference between the versions the phase maps of the 100 x 100 pattern file indexed using $n = 2$ and both $w = 1/8$ and $w = 1/4$ for v.4.3 and v.5.0 are shown in Figure 4.39.

(a) Phase map

(b) IPF map

(c) IQ map

(d) Pattern intensity map
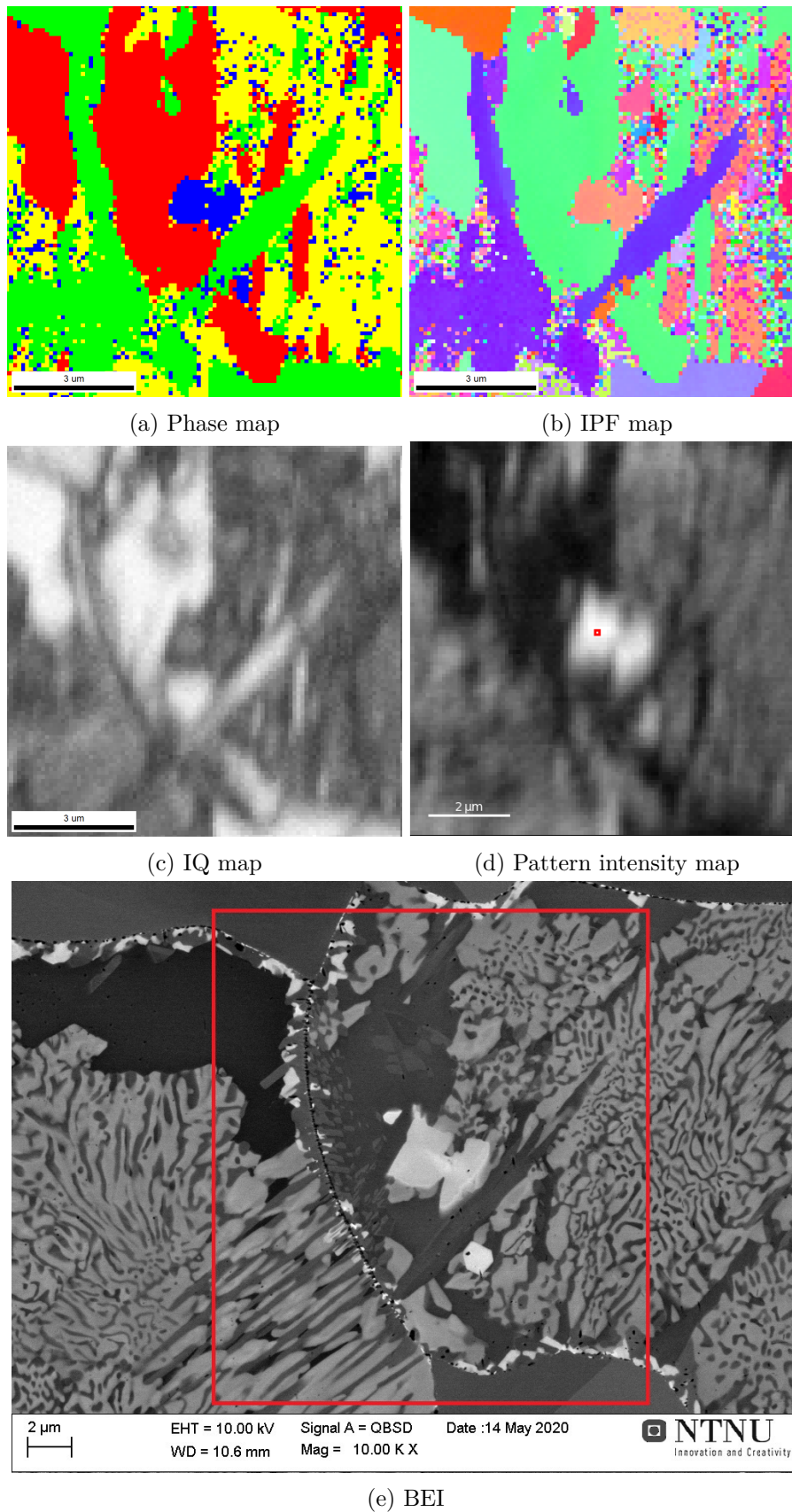
(e) BEI

Figure 4.34: a,b,c) EBSD maps from HI, d) Pattern intensity map and e) BEI of the ROI

(a) PM, $n = 1$ (b) IPF, $n = 1$

(c) PM, $n = 2$ (d) IPF, $n = 2$

(e) PM, $n = 3$ (f) IPF, $n = 3$
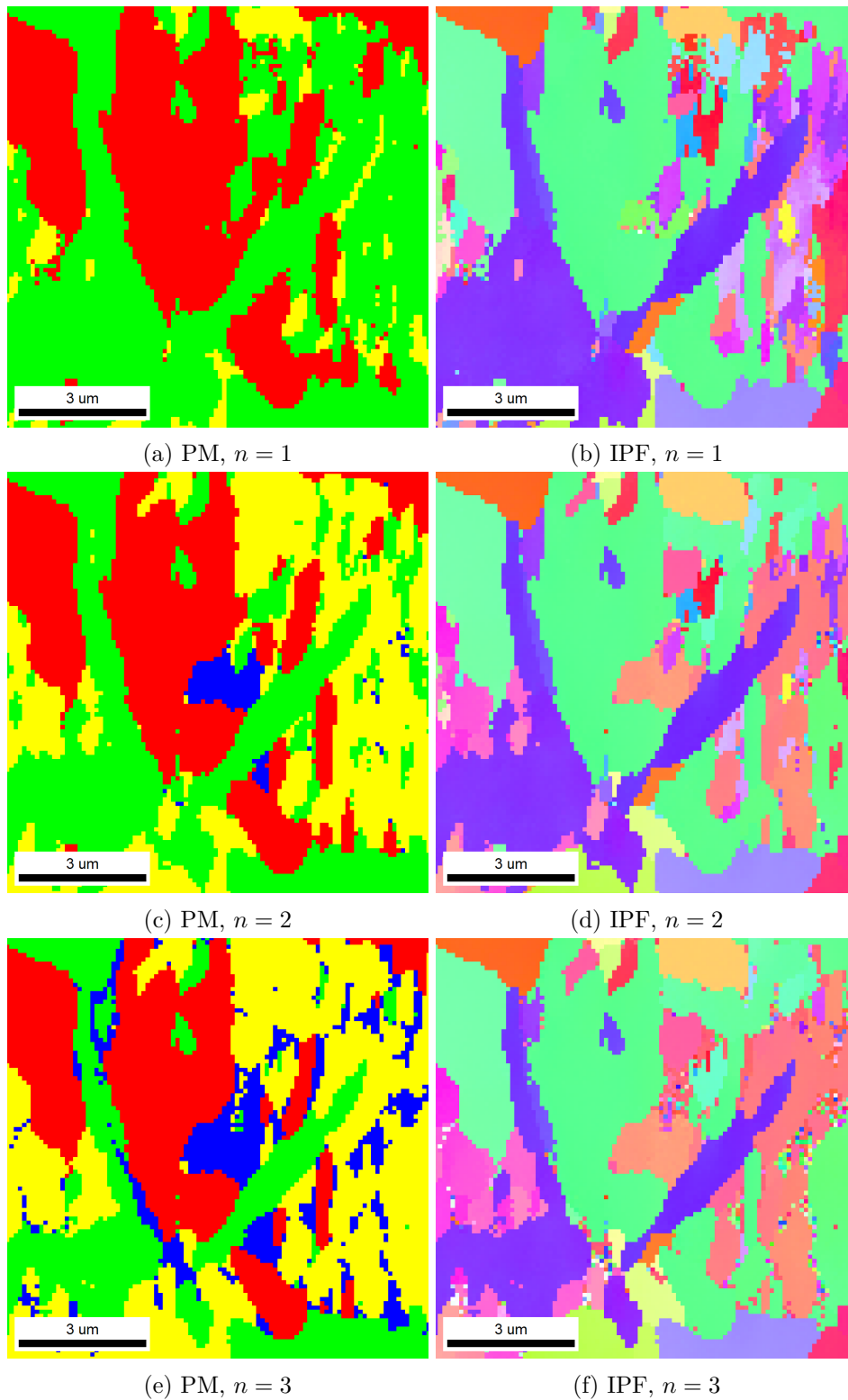
Figure 4.35: Phase and IPF maps from DI for multiple indexing runs of the same pattern file. A [SDHAG] pattern processing recipe is applied using $w = 1/8$ for all indexing runs. $n = 1, 2$ and 3 are used as input for the AHE n-parameter

Table 4.7: Phase fractions for the cropped pattern file from the SD750C sample when using the HI approach

Ferrite (α), %	Austenite (γ), %	Sigma (σ), %	Chi (χ), %
31.0	30.6	31.0	7.4

Table 4.8: Phase fractions of the cropped pattern file from the SD750C sample when using the DI approach. Fractions obtained when using $n = 1, 2$ and 3 as inputs are given

n-value	Ferrite (α), %	Austenite (γ), %	Sigma (σ), %	Chi (χ), %
1	37.65	54.83	7.52	0.00
2	31.87	34.33	31.49	2.31
3	26.74	22.58	38.99	11.69
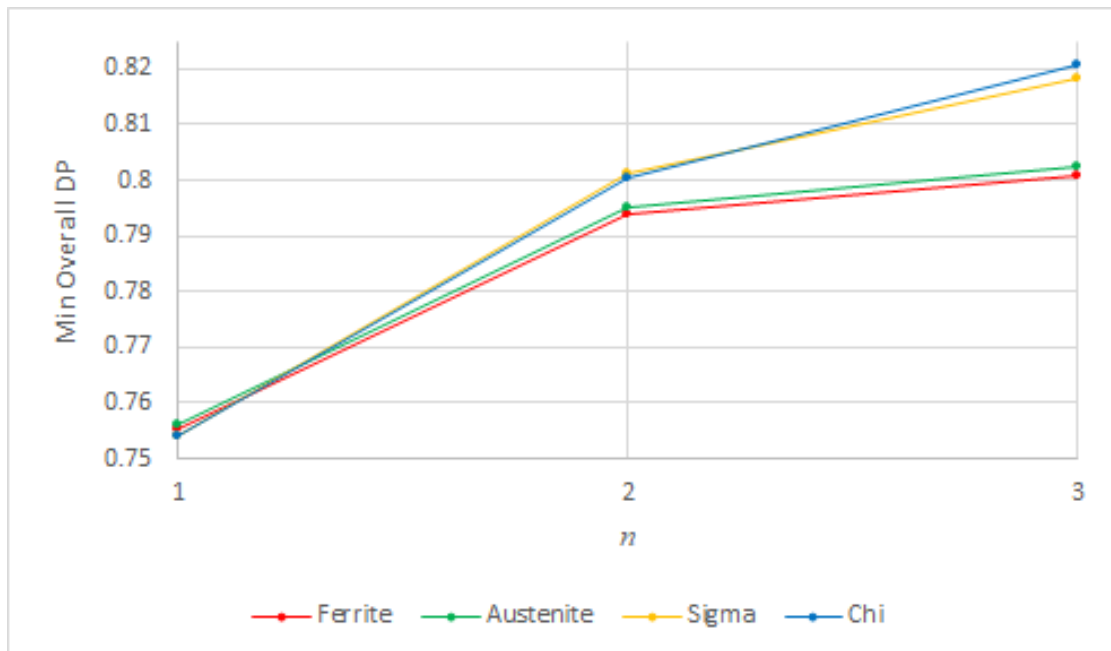
Figure 4.36: The minimum overall dot product value for each phase plotted against the AHE n-value. $w = 1/8$ for all patterns

(a) $w = 1/64$ (b) $w = 1/32$

(c) $w = 1/16$ (d) $w = 1/8$

(e) $w = 1/4$ (f) $w = 1/2$
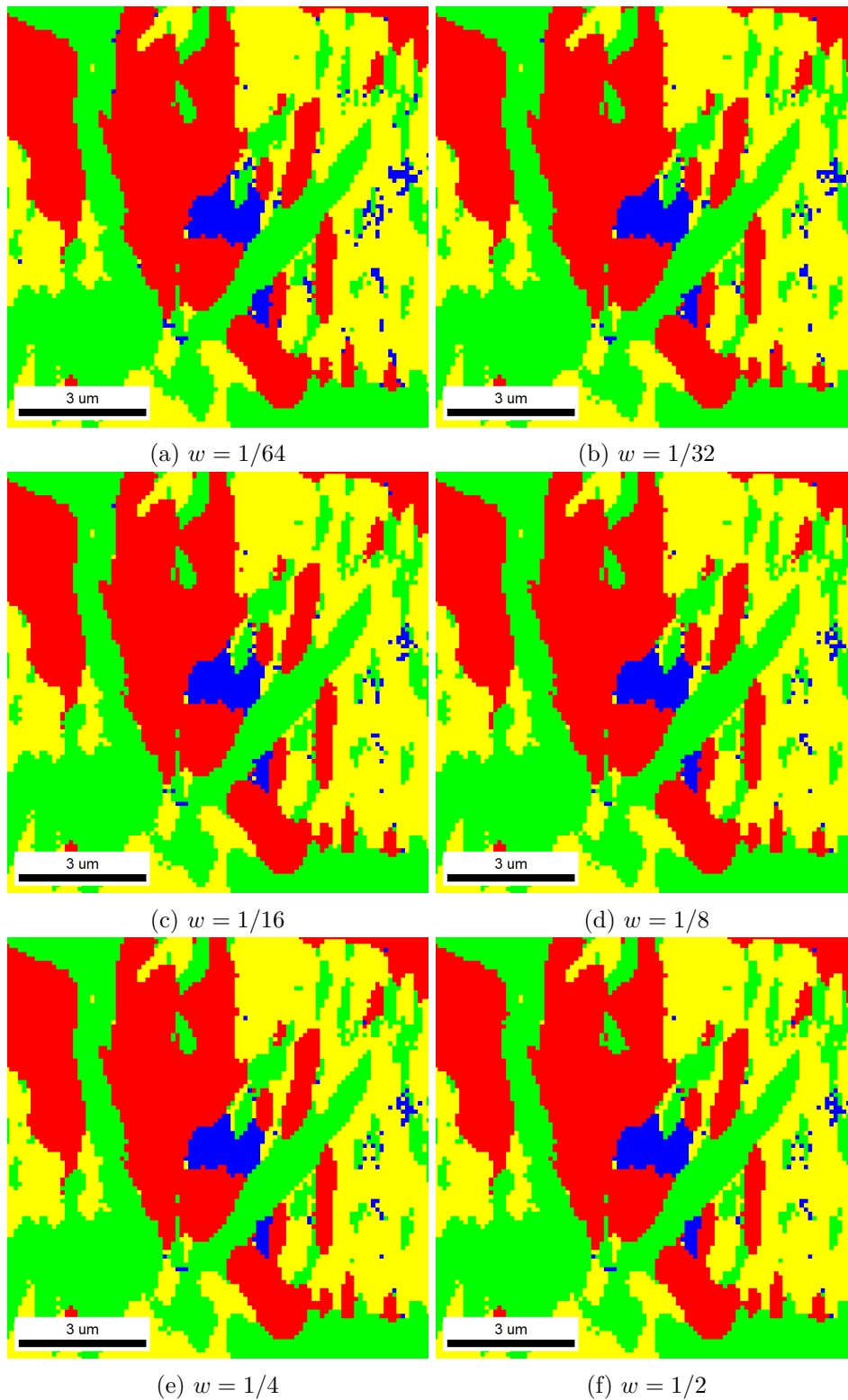
Figure 4.37: Phase maps from DI for multiple indexing runs of the cropped pattern file. A [SDHAG] pattern processing recipe is used when applying $n = 2$ for all indexing runs. Various w-values are used as input for the high-pass filtering. EMsoft version 4.3 was used for the DI

Table 4.9: Phase fractions of the cropped pattern file from the SD750C sample. Phase fractions for various applied high-pass filtering w-values are presented. EMsoft version 4.3 was used for the DI

w-value	Ferrite (α), %	Austenite (γ), %	Sigma (σ), %	Chi (χ), %
1/64	31.31	32.24	33.03	3.42
1/32	31.49	33.12	32.53	2.86
1/16	31.47	33.36	32.52	2.65
1/8	31.51	33.48	32.44	2.57
1/4	31.54	33.48	32.39	2.59
1/2	31.48	33.55	32.37	2.60
1	10.18	3.38	0.00	86.44
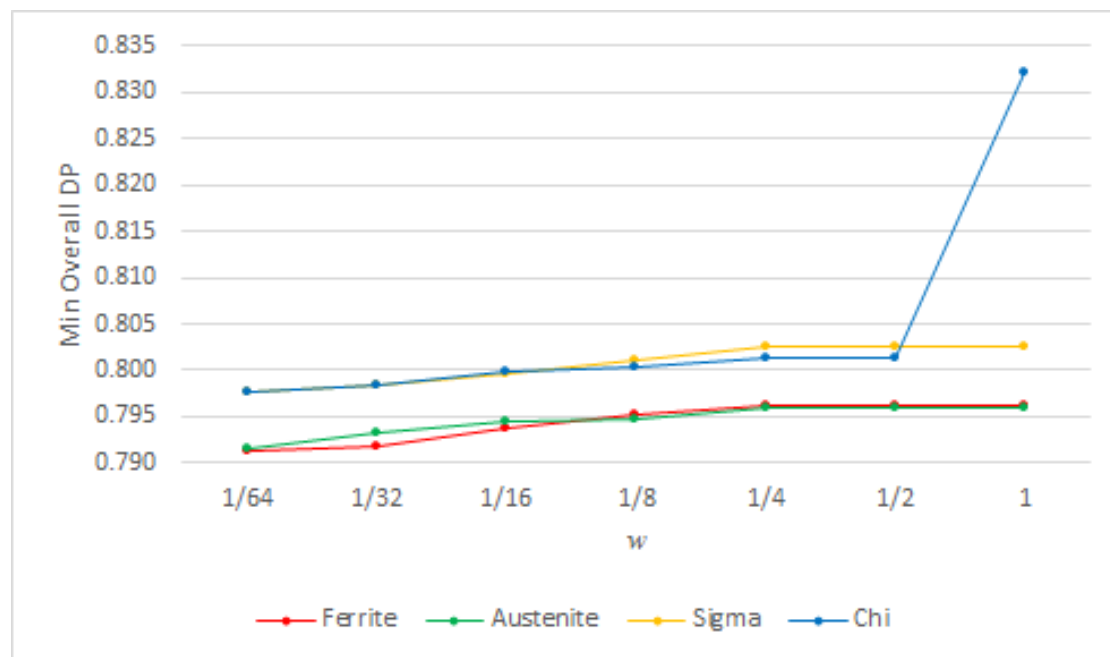
Figure 4.38: The minimum overall dot product value for each phase plotted against the high-pass filtering w-value. $n = 2$ are used for all cases. EMsoft version 4.3 was used for the DI

(a) EMsoft v.4.3, $w = 1/8$ (b) EMsoft v.4.3, $w = 1/4$

(c) EMsoft v.5.0, $w = 1/8$ (d) EMsoft v.5.0, $w = 1/4$
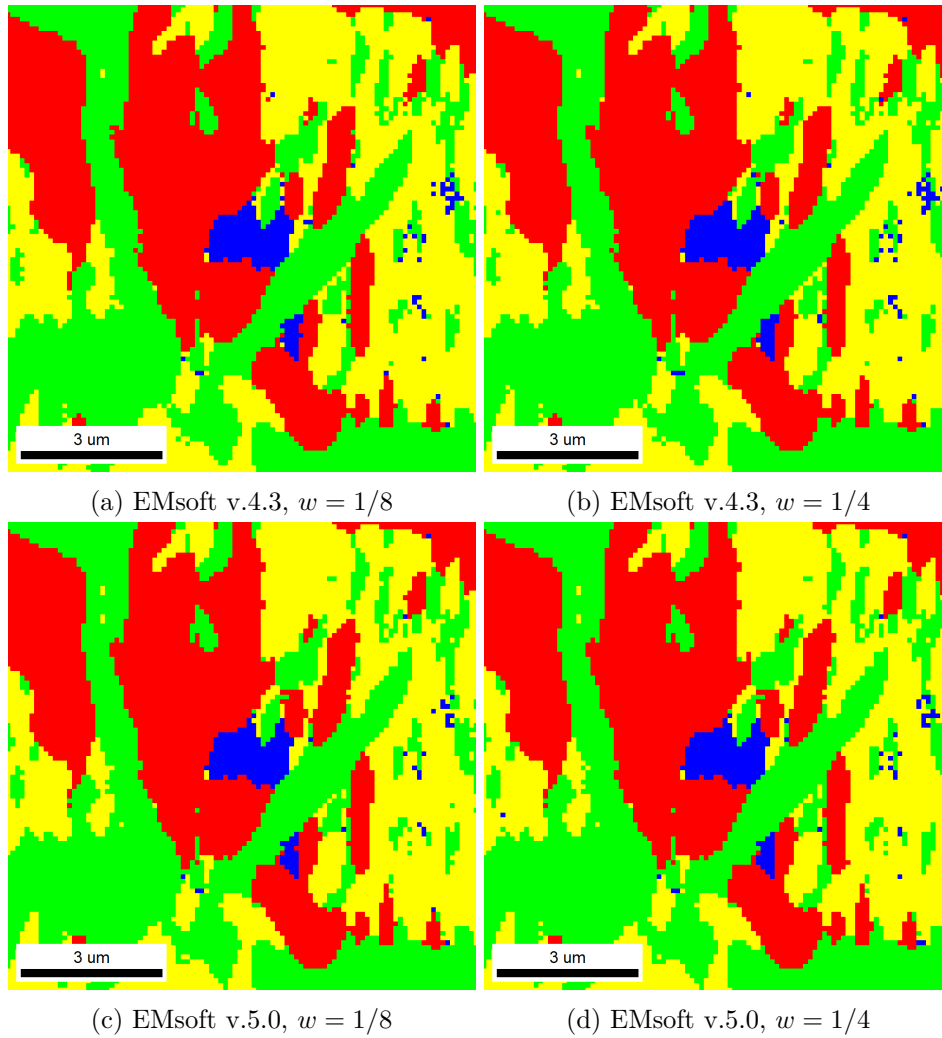
Figure 4.39: Comparison of the phase maps obtained from EMsoft version 4.3 and EMsoft version 5.0. $n = 2$ is used for all DI runs

To further assess the results of the dictionary indexing, some experimental patterns have been selected and are presented together with the simulated patterns of best match for the relevant phases. In Figure 4.40 the pattern locations in the phase map of $n = 2$ is given. In Figure 4.41 to 4.46 the patterns are shown. In Figure 4.47 the orientation similarity maps for the cropped pattern file are presented together with the DI phase map ($n = 2$) and the BEI of the corresponding region. In Figure 4.48 some experimental pattern examples are shown together with the corresponding simulated χ-pattern of best match. Here the obtained DP-value for χ to the patterns are also labeled.

(a) PM showing pattern locations   (b) Phase map with CI overlaid
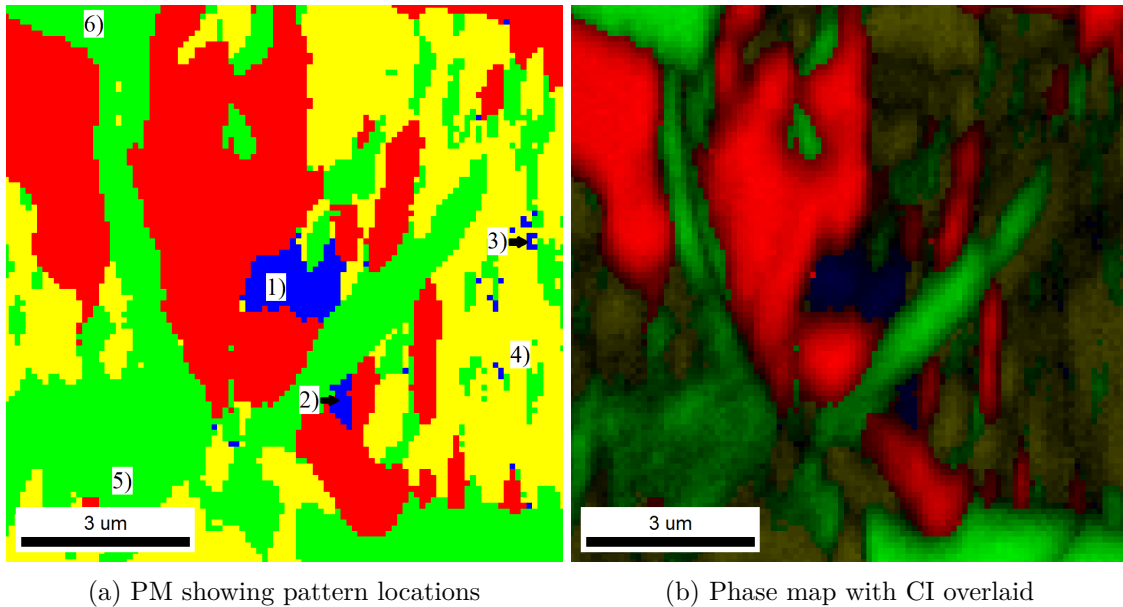
Figure 4.40: a) Phase map which is showing the location of the example patterns. To better see the difference in the pattern quality between the patterns in the pattern file, the phase map with CI overlaid is shown in b)

(a) [SD]   (b) [SDHA], $n = 2$ (c) avg. [SD]

(d) sim.pat α (e) sim.pat γ (f) sim.pat σ (g) sim.pat χ

Figure 4.41: Pattern 1), which is indexed as χ for $n = 2$. In a) and b) the experimental pattern is shown for different pattern processing recipes. In c) an averaged pattern from the same χ-indexed particle is shown. In d), e), f) and g) the simulated patterns of best match for α, γ, σ and χ are shown respectively. By comparing the experimental pattern to the simulated patterns, the indexing of χ seems to be correct

(a) [SD]   (b) [SDHA], $n = 2$ (c) avg. [SD]

(d) sim.pat α (e) sim.pat γ (f) sim.pat σ (g) sim.pat χ
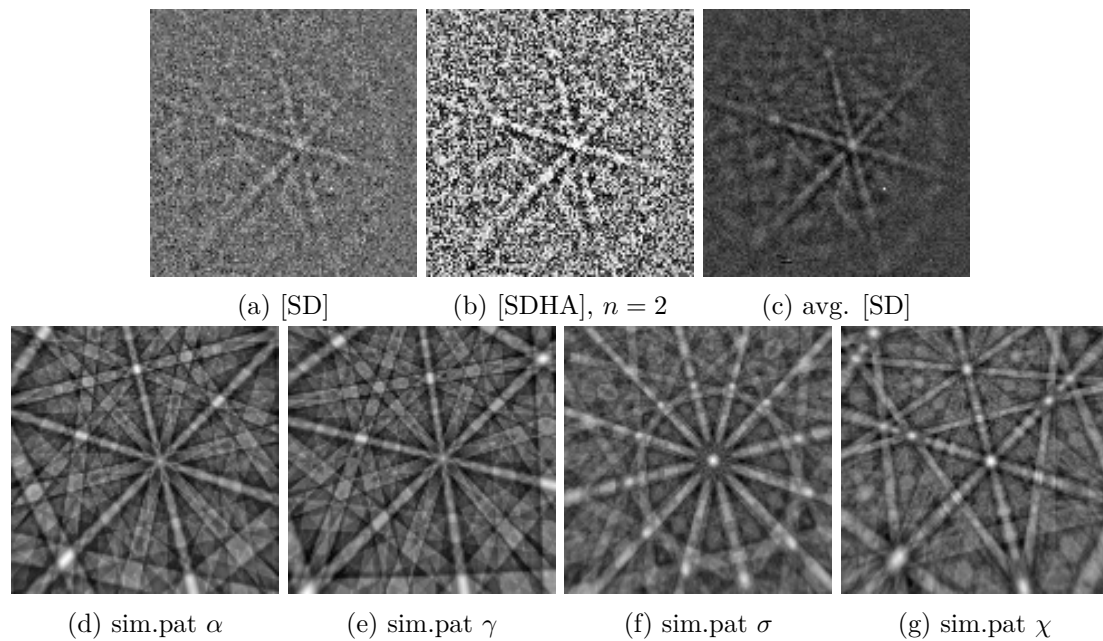
Figure 4.42: Pattern 2), which is indexed as χ for $n = 2$. In a) and b) the experimental pattern is shown for different pattern processing recipes. In Figure c) an averaged pattern from the same χ-indexed particle is shown. In d), e), f) and g) the simulated patterns of best match for α, γ, σ and χ are shown respectively. By comparing the experimental pattern to the simulated patterns, the indexing of χ seems to be correct

(a) [SD]   (b) [SDHA], $n = 2$

(c) sim.pat γ (d) sim.pat σ (e) sim.pat χ
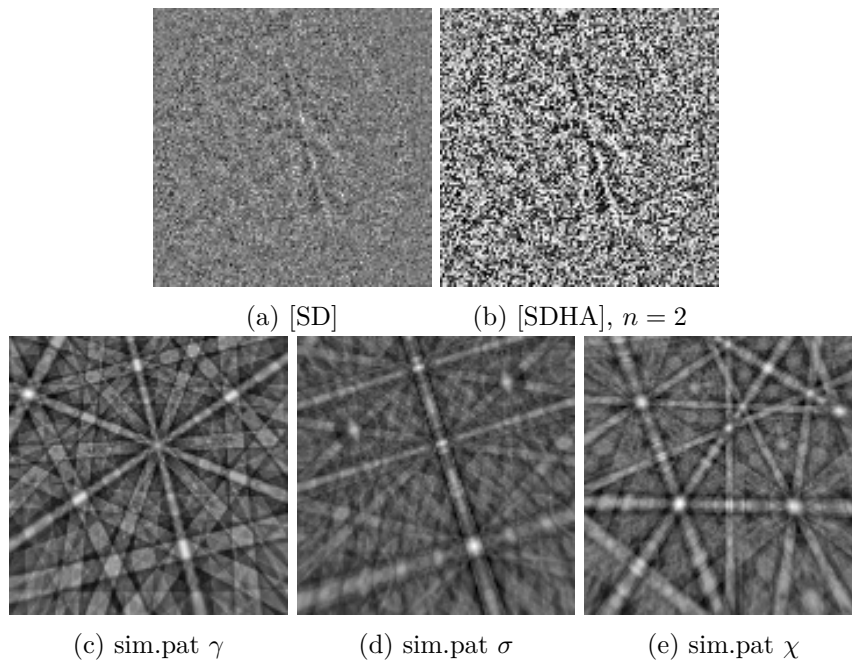
Figure 4.43: Pattern 3), which is indexed as χ for $n = 2$. In a) and b) the experimental pattern is shown for different pattern processing recipes. In c), d) and e) the simulated patterns of best match for γ, σ and χ are shown respectively. By comparing the experimental pattern to the simulated patterns, the indexing of χ seems to be incorrect. Based on the simulated patterns, either γ or σ should be the correct indexing

(a) [SD]   (b) [SDHA], $n = 2$

(c) sim.pat γ (d) sim.pat σ
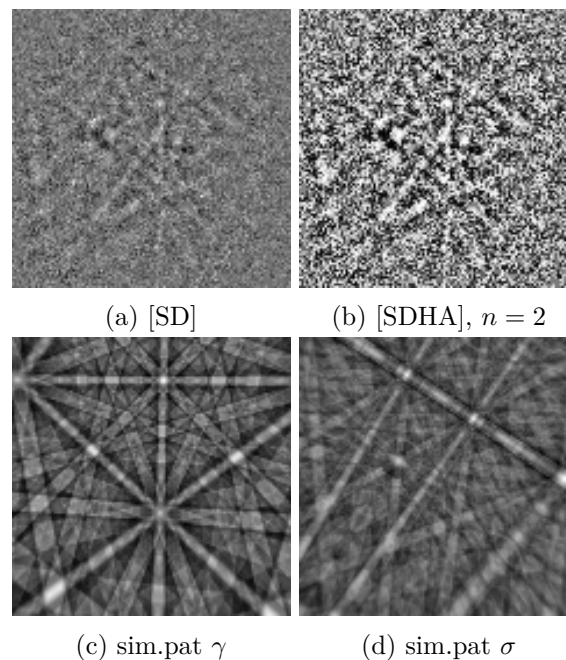
Figure 4.44: Pattern 4), which is indexed as σ for $n = 2$. In a) and b) the experimental pattern is shown for different pattern processing recipes. In c) and d) the simulated patterns of best match for γ and σ are shown respectively. By comparing the experimental pattern to the simulated patterns, features of both γ and σ are present in the experimental pattern

(a) [SD]   (b) [SDHA], $n = 2$

(c) sim.pat γ (d) sim.pat σ
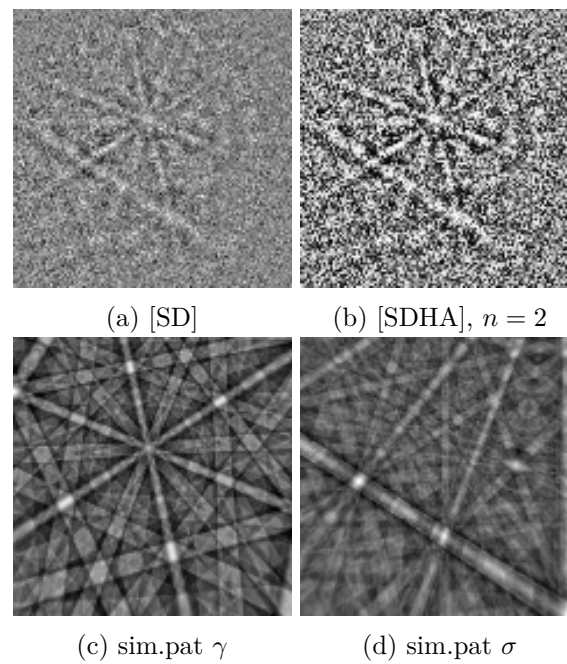
Figure 4.45: Pattern 5), which is indexed as γ for $n = 2$. In a) and b) the experimental pattern is shown for different pattern processing recipes. In c) and d) the simulated patterns of best match for γ and σ are shown respectively. By comparing the experimental pattern to the simulated patterns, features of both γ and σ are seen in the experimental pattern

(a) [SD]   (b) [SDHA], $n = 2$ (c) sim.pat γ
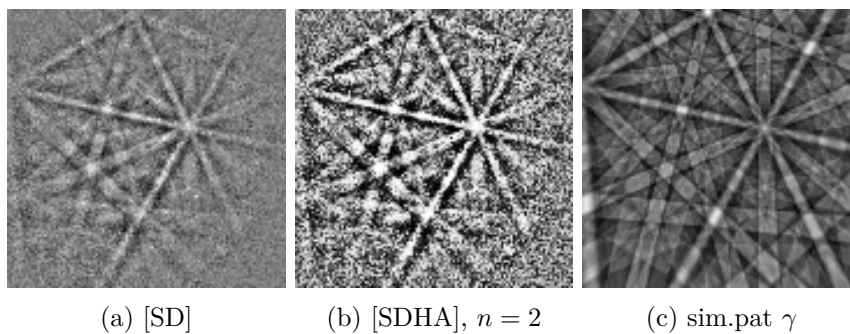
Figure 4.46: Pattern 6), which is indexed as γ for $n = 2$. In a) and b) the experimental pattern is shown for different pattern 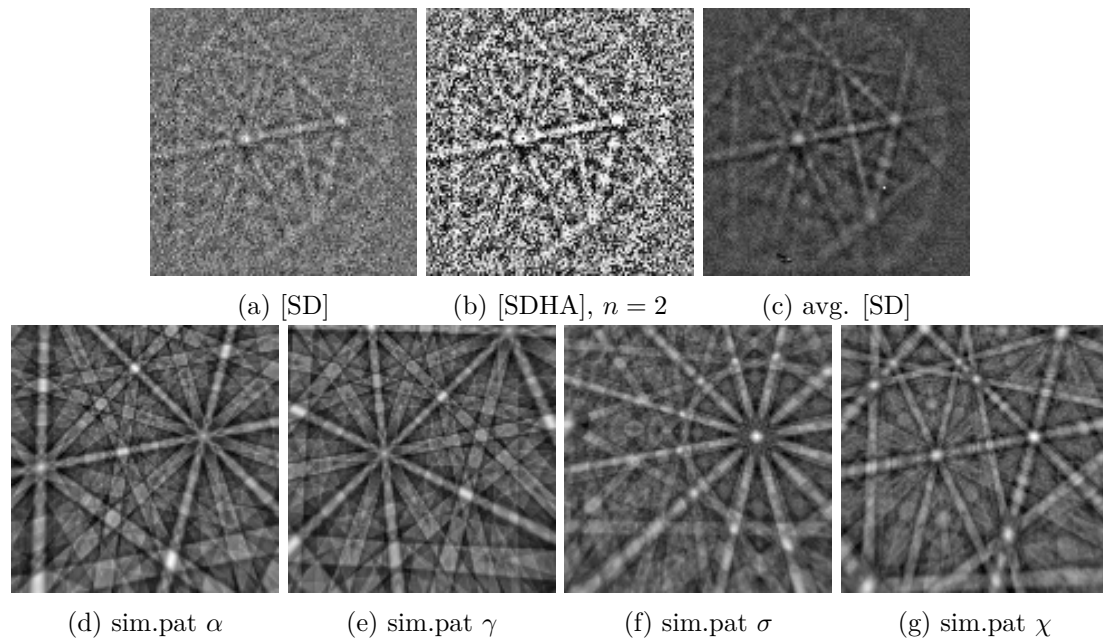processing recipes. In c) the simulated pattern of best match for γ is shown. By comparing the experimental pattern 6) to experimental pattern 5) in Figure 4.45, pattern 6) contains more γ-features and lesser noise

(a) PM, DI

(b) BEI

(c) OSM α

(d) OSM γ

(e) OSM σ

(f) OSM χ
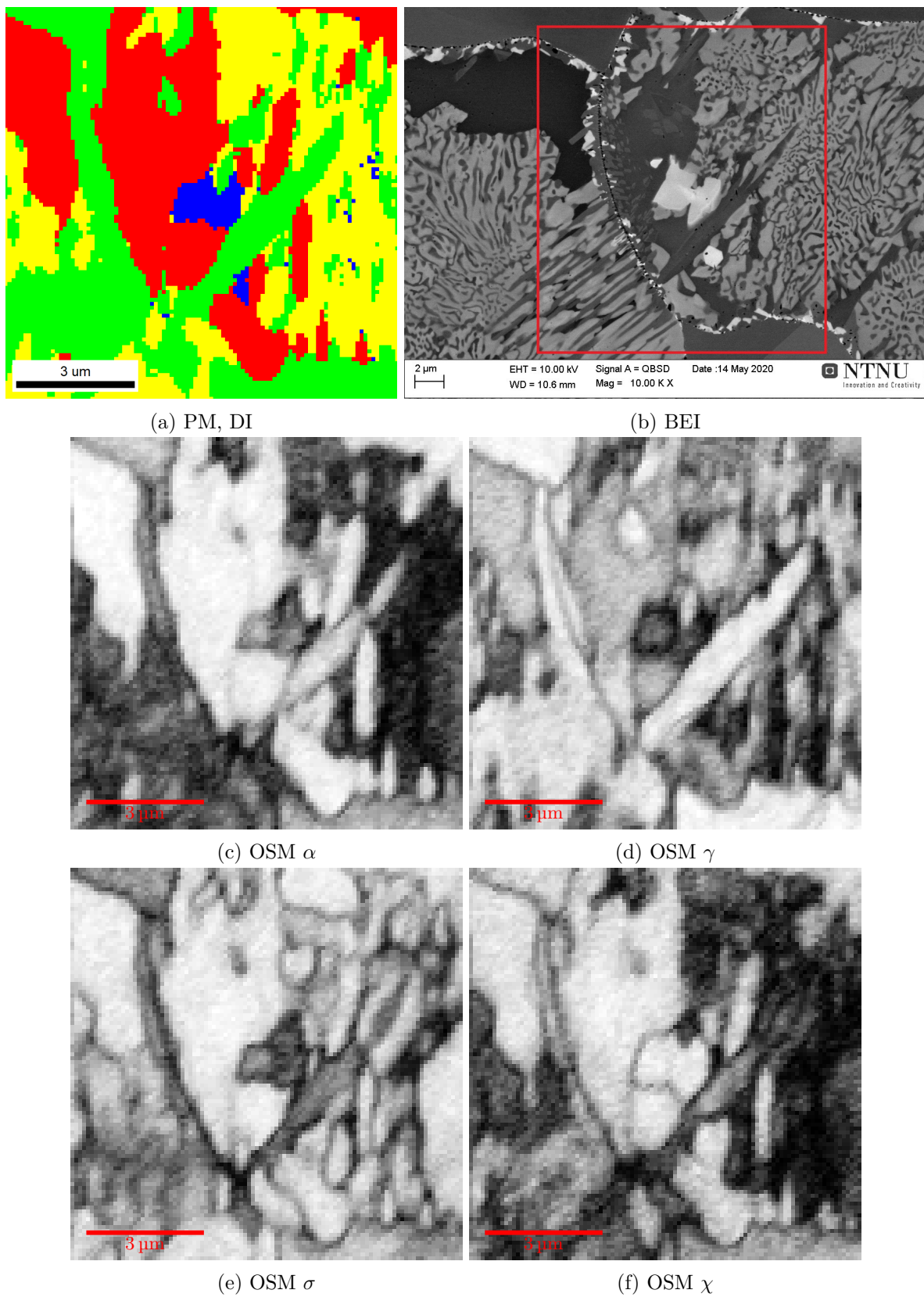
Figure 4.47: OSMs of the cropped pattern file from SD750C. The OSMs of α, γ, σ and χ are shown in Figure c) to f) respectively. In a) and b) the PM from DI ($w = 1/8$ & $n = 2$) and the BEI of the corresponding region are shown respectively

77

1) Worst match, χ 2) Best index, χ 3) Best match, χ

1) $DP = 0.800$, χ 2) $DP = 0.816$, χ 3) $DP = 0.818$, χ 3) $DP = 0.857$, α
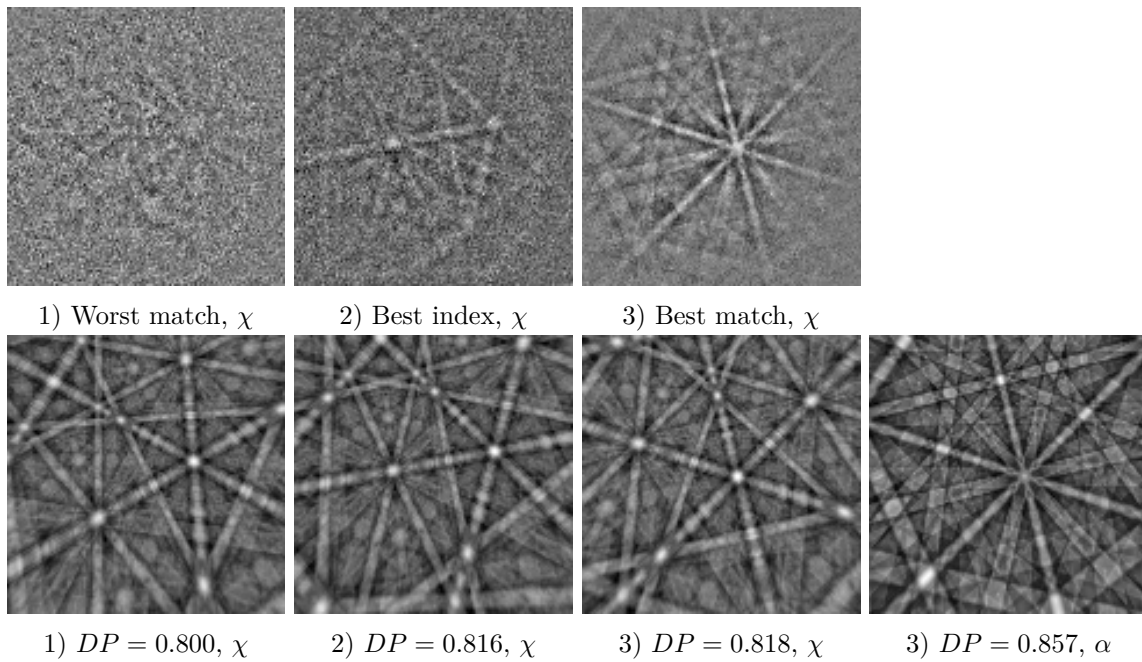
Figure 4.48: The upper row is showing three experimental patterns from the cropped pattern file of SD750C, having a [SD] pattern processing. The lower row shows simulated pattern of best match related to the experimental patterns. The obtained dot product values of the simulated patterns to their respectively experimental pattern, when using a [SDH$_{1/8}$A$_2$G] pattern processing recipe, are labeled under the simulated patterns. Experimental pattern 1) has the lowest χ DP-value of all the pattern in the pattern file. Pattern 2) has the highest χ DP-value among the patterns of which χ gets the best match (compared to α, γ and σ). Pattern 3) has the highest overall χ DP-value in the pattern file. However, the simulated α-pattern shown has a better match to this experimental pattern

4.3.3 Comparison of HI and DI, SD750C

To compare how the Hough indexing and dictionary indexing approaches perform on the SD750C sample, various EBSD maps from each approach is presented and compared here. The maps are from the 685 x 685 pattern file of this sample. For the DI a pattern processing recipe using $n = 2$ and $w = 1/8$ is applied. In Table 4.10 the phase fractions from HI and DI are given. In Figure 4.49 the BEI of the EBSD ROI is shown. The EBSD maps are presented in Figure 4.50 to 4.54.

Table 4.10: Phase fractions of the pattern file from the SD750C sample. Phase fractions from HI and DI are presented

Index approach	Ferrite (α), %	Austenite (γ), %	Sigma (σ), %	Chi (χ), %
HI*	18.0	65.0	15.0	2.0
DI	17.6	65.1	17.2	0.1

*An error in the rounding of the numbers leads to an uncertainty of $\pm 0.1\%$ in the HI data.
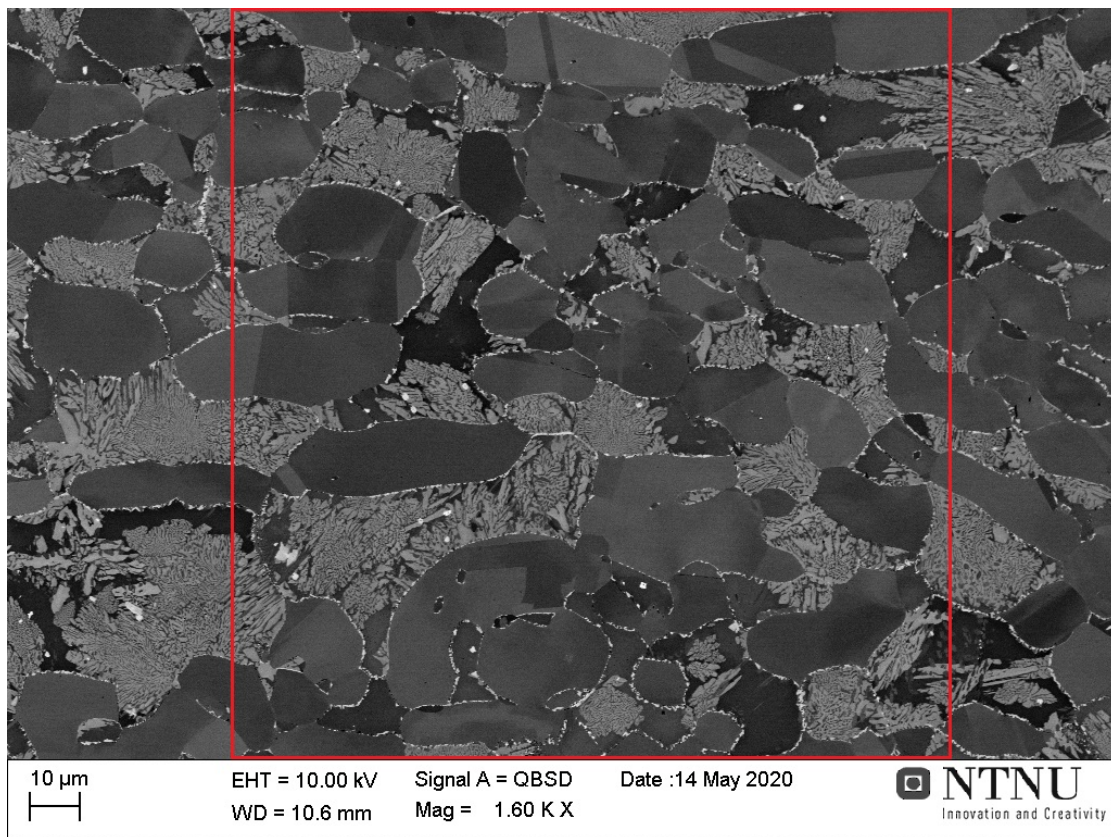
Figure 4.49: BEI of the SD750C sample
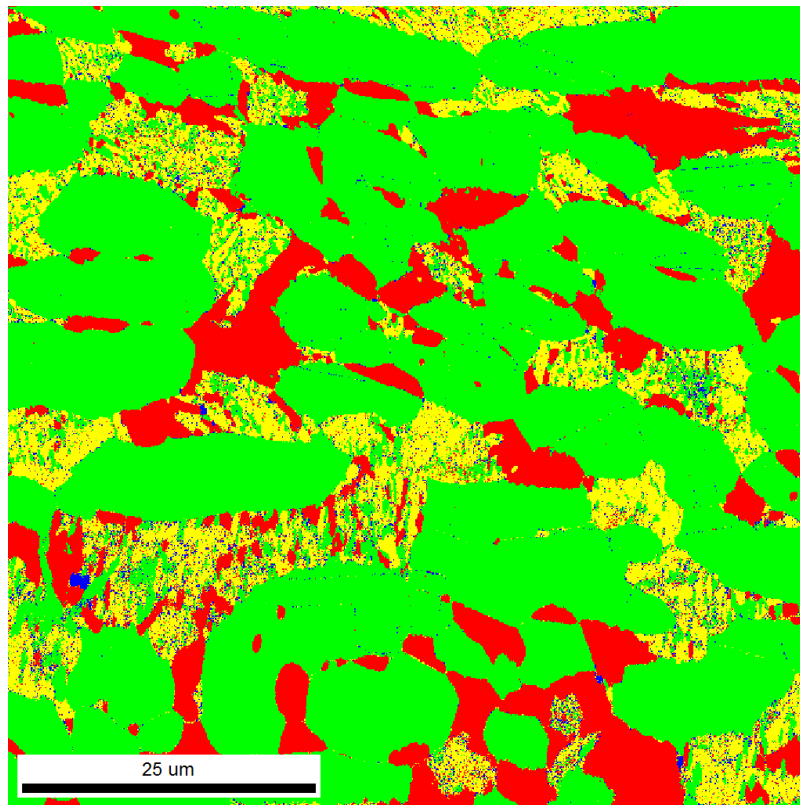
(a) PM, HI
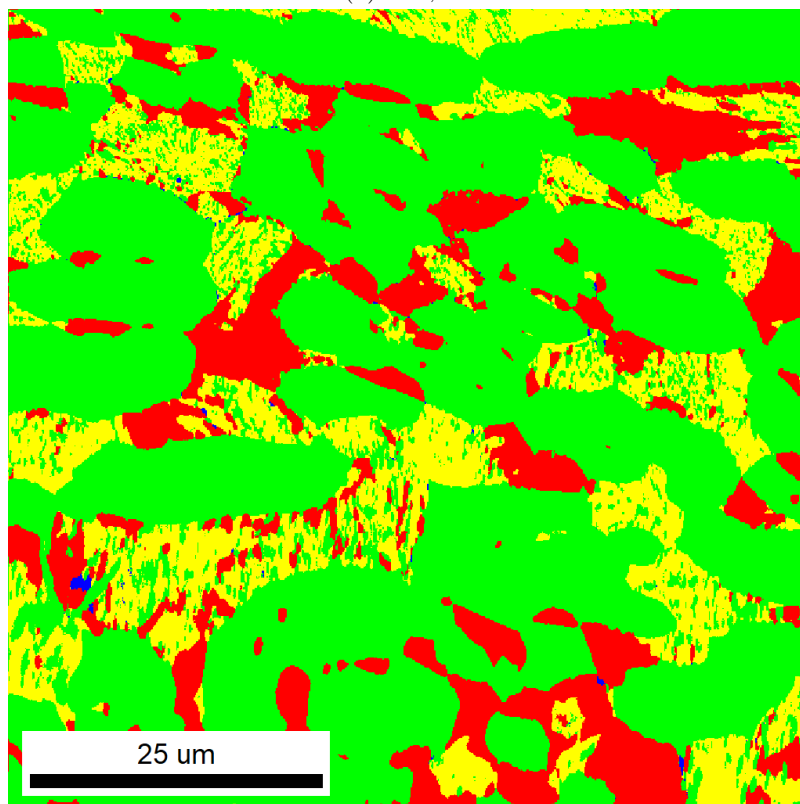
(b) PM, DI

Figure 4.50: Phase maps for the SD750C sample. a) PM from HI, b) PM from DI
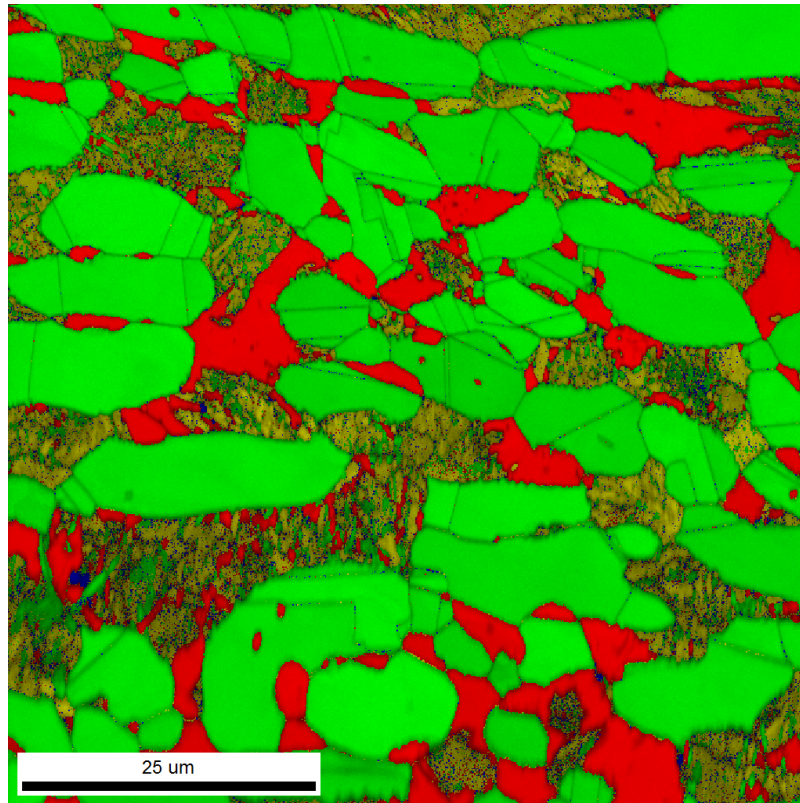
(a) HI
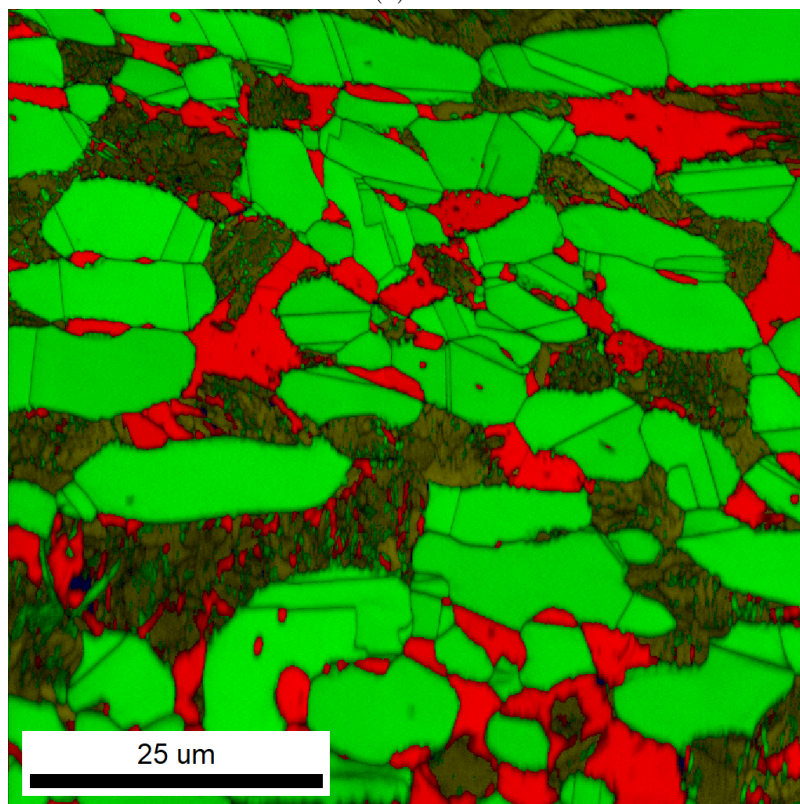
(b) DI

Figure 4.51: Phase maps with IQ (HI) or CI (DI) overlaid for the SD750C sample. a) Map from HI, b) Map from DI
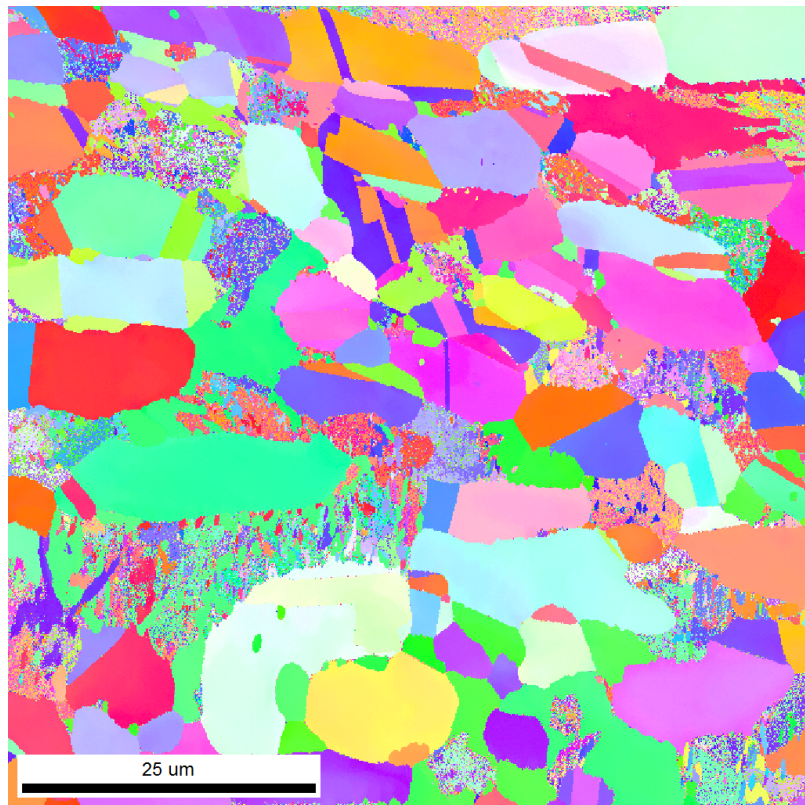
(a) IPF map, HI
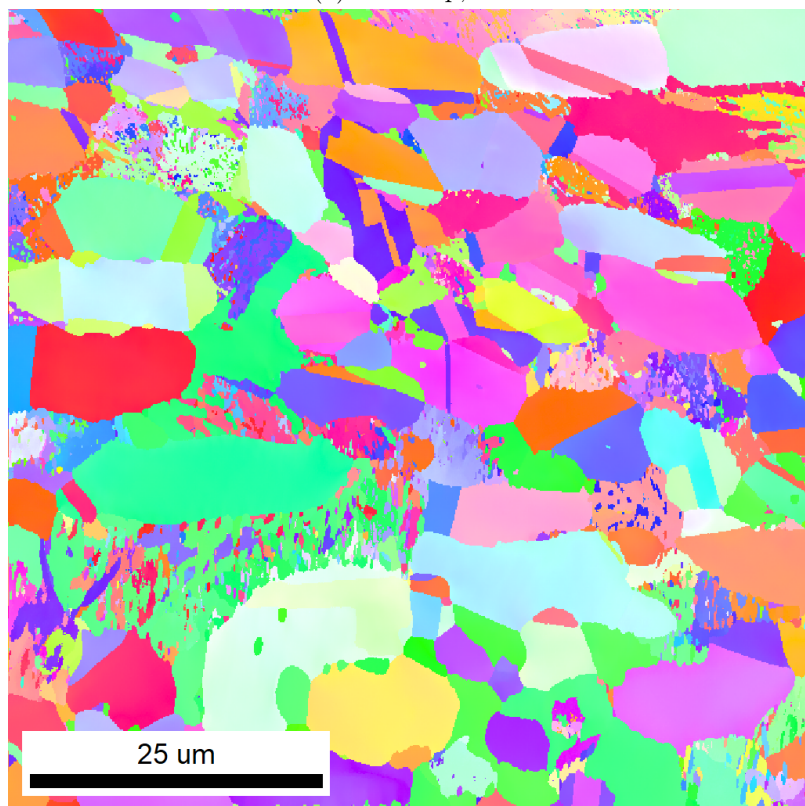
(b) IPF map, DI

Figure 4.52: IPF maps for the SD750C sample. a) Map from HI, b) Map from DI
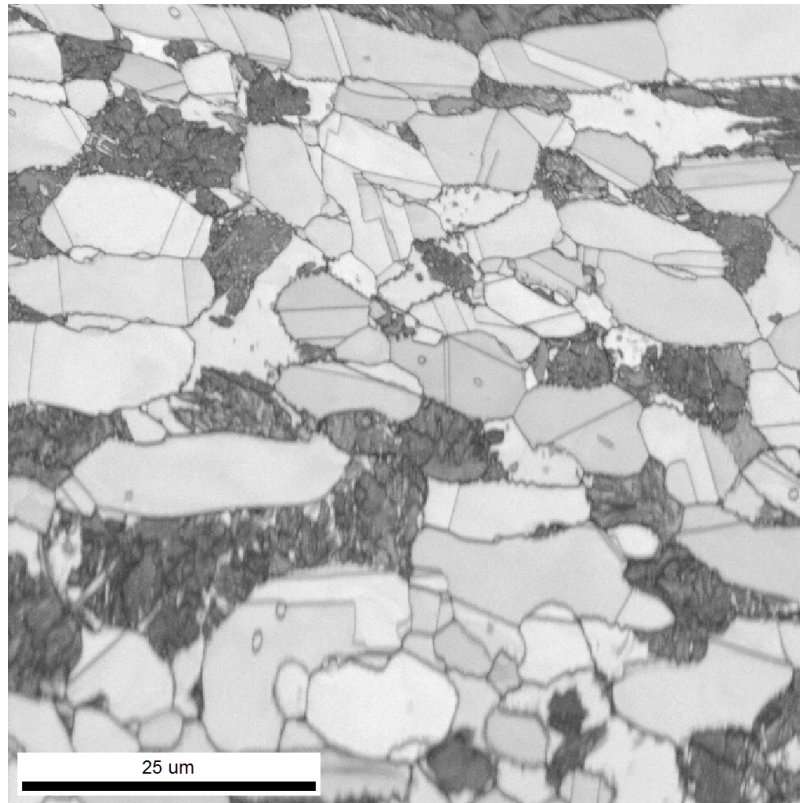
(a) IQ map, HI
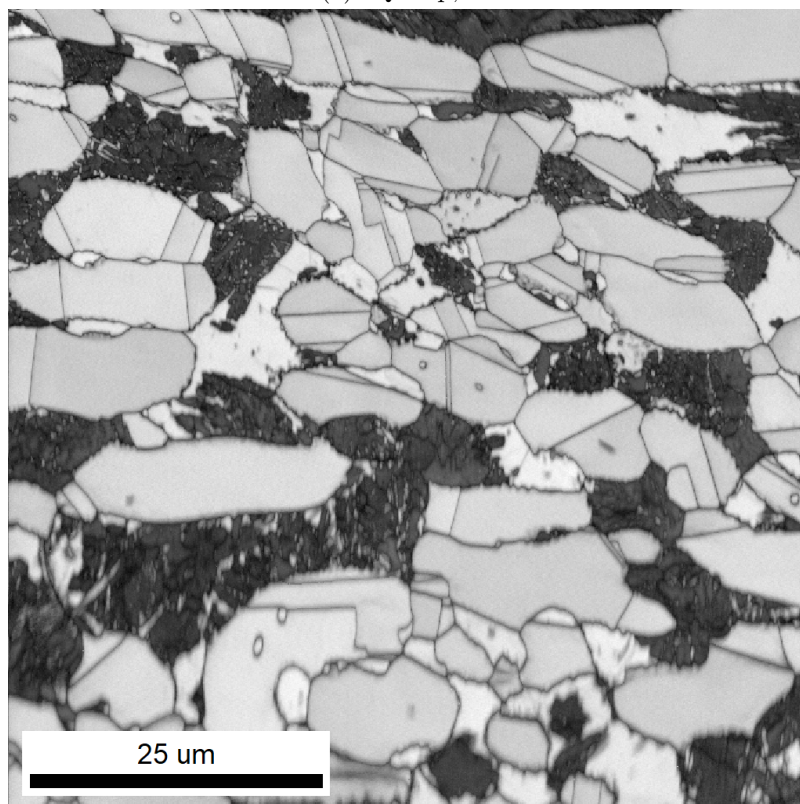
(b) CI map, DI

Figure 4.53: Pattern quality maps for the SD750C sample. a) IQ map from HI, b) CI map from DI

(a) PM, HI

(b) PM, DI

(c) IPF map, HI

(d) IPF map, DI

(e) IQ map, HI

(f) CI map, DI
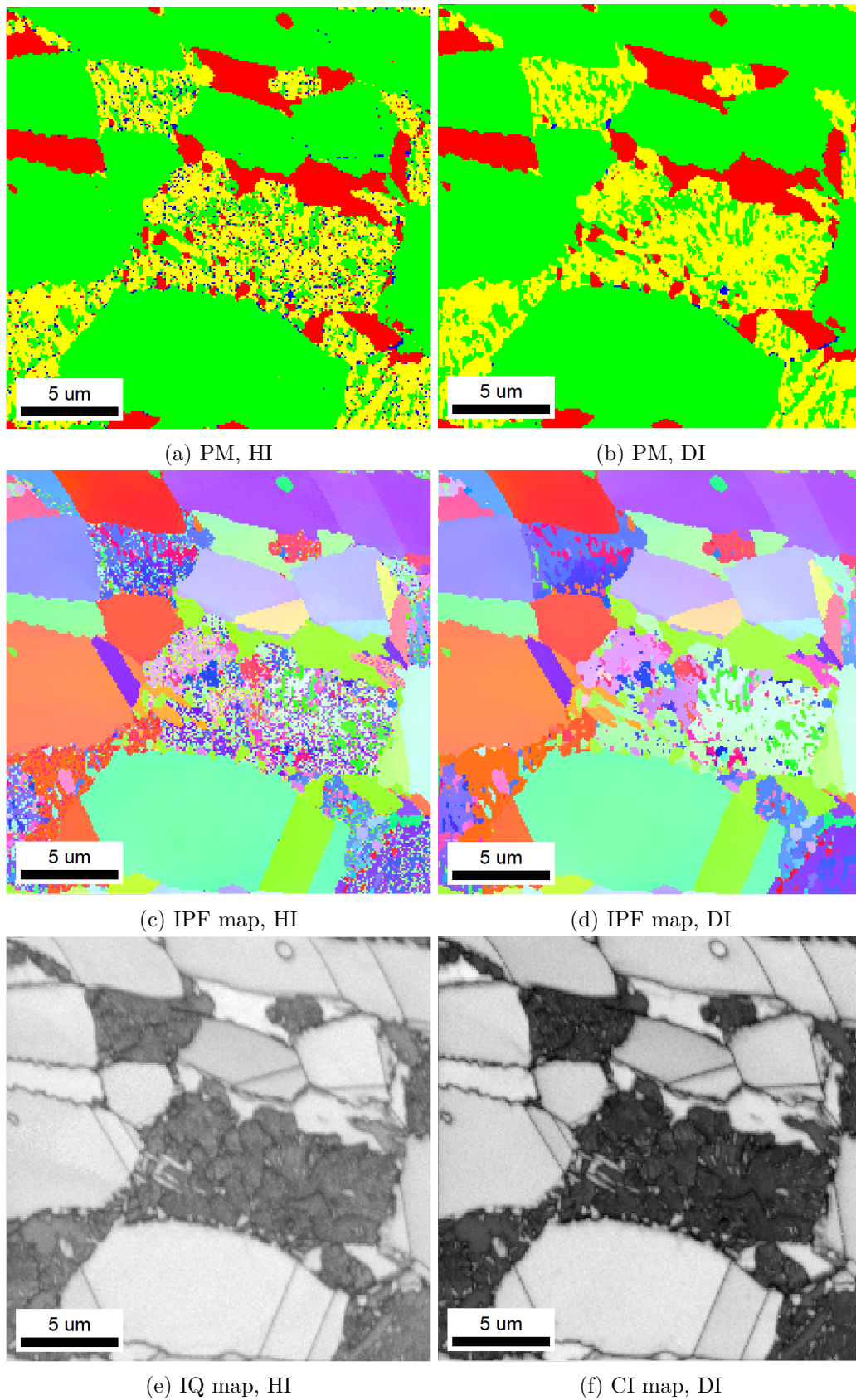
Figure 4.54: EBSD maps from HI and DI of increased magnification. The maps are from the top left corner of the SD750C pattern file

84

5 Discussion

In this section the obtained results are discussed. In section 5.1 the obtained optical microscopy images, BEIs and results from EPMA are commented. In section 5.2 the results from the pattern prosessing tuning with respect to the AHE n-parameter are discussed for every sample examined. A similar discussion for the dynamic correction and high-pass filtering w-parameter is given in section 5.3. In section 5.4 the backcatter electron images and the results from HI are compared to the obtained results from DI, when what is considered the best pattern processing for DI is used. Finally, some issues related to DI are discussed in section 5.5.

5.1 Optical Microscopy, Backscatter Electron Images and EPMA Results

To verify which phases that were expected to find in the studied samples, optical microscopy, backscatter electron imaging and/or EPMA were used together with EBSD when characterising the samples. WAAM2 was first studied using optical microscopy. The obtained images which show different zones in the sample were presented in Figure 4.15 and 4.16. Here, chromium nitrides were observed in the HAZ of the base plate, present both in the α-grain interiors and along α/α-grain boundaries. As both the γ-phase and the chromium nitrides appear white with the electropolishing applied, it is not easy to verify if chromium nitrides also have precipitated at α/γ-grain boundaries. However, in the literature this is stated as a potential site for chromium nitride formation as well [28]. To easier study the chromium nitride particles, backscatter electron imaging was used. Two BEIs were presented in Figure 4.30. Some of the particles formed in the α-grain interior are observed to have the rod-shape which Cr_2N has. However, CrN has probably not been formed as there is no observation of film-like regions [27, 29]. An effort was also made in studying the C_2N-particles using EBSD. Here HI was used. As no bmt file for Cr_2N was available, only α and γ were included as phases in the indexing. If any EBSD pattern would be dominated by a Cr_2N particle it was expected some distortion would be seen in the obtained IPF map. However, as Figure 4.31 shows, no distortion is seen in the IPF map. When comparing the obtained IQ map to the BEI in Figure 4.30b, it is possible to see the Cr_2N-particles are affecting the pattern quality where they are located. However, when studying some of the experimental EBSD patterns from the Cr_2N-particles sites, the patterns are only containing the same pattern features of the neighbour α-patterns of higher quality, but are having slightly more noise present. No unique pattern features which could be origin from Cr_2N are observed. It is reasonable to assume the Cr_2N present are too small to be studied using EBSD, at least with the EBSD parameters and equipment used for this thesis.

The optical microscopy images of WAAM2 also show that formation of σ-phase has occurred in the sample, as seen in the image of the 8th and 15th weld wires in Figure

4.15. However, σ-phase was not seen in the 1st weld wire (as seen in Figure 4.15d). In fact, when studying the sample in the optical microscope, the lower segment of the weld wall was observed to be free from σ-formation. However, no exact measurement of the length up from the lower end was done. As Cr_2N is formed in the HAZ of the base plate and σ is absent from the lower weld wires, the lower section of the sample is probably cooling faster than the intermediate weld wires, as σ-phase is formed by slow cooling and Cr_2N is formed by fast cooling [2, 27]. Although σ-phase is observed in the 15th wire, it seems like less σ-phase is being formed here with respect to the 8th wire. When trying to find σ-phase in the WAAM1 sample in the specialization project [8], examining the lower sections and the 15th weld wire, and not one of the wires in the middle of the weld wall was therefore not ideally. When further examining the WAAM1 sample with backscatter electron imaging, σ-phase was found both in the middle of the weld wall as well as in the 15th weld wire (shown in Figure 4.14). Although the σ-fraction present in the WAAM1 sample is low, the conclusion in the specialization project stating that the sample did not contain any σ-phase is therefore not correct [8].

When studying the 8th weld wire of WAAM2 with backscatter electron imaging, σ-phase is found as expected with respect to the optical microscopy results. However, it was not known beforehand if any trace of χ-phase would be found, as the electropolishing preparation for optical microscopy is not suitable for distinguishing σ and χ. As seen in the BEIs in Figure 4.27 and 4.19a, some smaller grains which appear brighter than the surrounding σ-phase are present. As χ has a higher fraction of Mo compared to σ ($\sim$14 % vs. $\sim$7 %), χ is expected to appear brighter due to Z-contrast [18]. As a way to verify if the bright grains were χ-phase, EPMA was used. Since Cr, Ni and Mo are having different fractions in the four phases α, γ, σ and χ, measuring the X-ray yield with respect to these element could potentially be used to distinguish the phases from each other [18]. However, when studying the obtained EPMA X-ray maps for the 8th wire, shown in Figure 4.18, very little information was gained. Although some of the small bright grains are present in the examined area, they are not distinguishing themselves from the surrounding phases in any of the maps. Their small sizes might be the reason behind this. On the other hand, σ can not be distinguished from α in any of the maps either. Only α/σ and γ phase areas are separated from each other in the maps. When point measurements where the intensity of characteristic X-rays with respect to Mo instead was performed, the measured mean X-ray intensity of the brighter grains was about twice the value of the σ-phase (as seen in Table 4.4). This reinforce the statement that these grains are of χ-phase.

Moving on to the SD750C sample, when studying the BEIs obtained for SD750C, the heat treatment at 750 °C for 2 hours has made significant changes to the microstructure. The microstructure before the heat treatment is supposed to look similar to the structure seen in the optical microscope image of the WAAM2 base plate, seen in Figure 4.15a. The SD750C sample is of the same base plate material as the WAAM2 base plate. While

the round γ grains seen in Figure 4.33 remain intact, a large portion of the α-phase has transformed into lamellar σ and γ. Also, smaller grains which appear brighter than the σ-phase are present. However, compared to the case in WAAM2, the grains believed to be χ-phase are present in a larger size and quantity. The χ-phase is observed inside remaining and transformed α-grains as well as along both α/α and α/γ grain boundaries. While the largest χ-grain observed in the BEI of WAAM2 in Figure 4.27 has a maximum cross section of about 1 μm, this value for the largest χ-grain, seen in the BEI of SD750C in Figure 4.34e, is at least 3.5 μm. The EPMA X-ray measurement map of SD750C for Mo, shown in Figure 4.32, also has higher intensity values for areas where the χ-phase is seen in the corresponding BEI.

5.2   The Effect of AHE on Dictionary Indexing

As previously mentioned, the used pattern processing recipe applied for DI in the specialization project gave mis-indexing of χ-phase [8]. It was therefore necessary to make changes to the pattern processing to see what effect it would have. The applied adaptive histogram equalization [40] was early considered a main candidate causing the χ mis-indexing. In Winkelmann (2018) [43] it is stated that AHE should be used as a mild pattern processing as possible. AHE can change the intensity distribution in the patterns considerably if not used properly and an intensity massage will affect agreement with pattern simulations. The kernel size should be larger than the Kikuchi features, preventing a rescale of the intensity in the Kikuchi band profile [43].

5.2.1   WAAM1

Using $n = 5$ as input for the AHE number of regions parameter, which was applied in the specialization project [8], could therefore already lead to way too small kernel sizes. However, EMsoft does not directly offer the user to turn off the AHE. This made it reasonable to initially test $n = 1$ as input, where a single kernel is used on the whole pattern for the AHE. When applying $n = 1$ the processing is equal to an ordinary histogram equalization. $n = 5$ was initially applied as it is recommended by Jackson et al. [4]. Two of the pattern files acquired in the specialization project [8], having a considerable high fraction of mis-indexed χ-phase, were selected for the testing. The results of the re-indexing using $n = 1$ were presented in section 4.1.1 and 4.1.2. For both pattern files the mis-indexed χ-phase is removed when using $n = 1$. Even for the pattern file of the electropolished surface, which had a high fraction of indexed χ-phase for poor quality α-patterns, seems to have no problems indexing the patterns correctly when $n = 1$ is instead applied. In section 4.1.1 some testing regarding the dynamic background correction and high-pass filtering was also performed. These results are commented in section 5.3. In the experimental pattern examples, presented in Figure 4.5 to 4.6 and in Figure 4.11 to 4.13, it is possible to see that the mis-indexing of χ occurs for patterns of poor quality. Even though the quality is poor, the simulated patterns

of best match make it easy to see what phase the experimental pattern is origin from. By studying the processed patterns when $n = 1$ and $n = 5$ are used, it is possible to see some differences in the intensity distribution. However, for the human eye all the Kikuchi pattern features are visible for both patterns. To judge the pattern processing by studying the patterns themselves is therefore not necessarily that straight forward. Although using $n = 1$ instead of $n = 5$ removed the mis-indexed χ, applying $n = 5$ gets a higher average dot product compared to applying $n = 1$ (as seen in Table 4.2). This implicates using a slightly higher n-value above 1 but below 5 might be a better n-value to use, to obtain a higher average dot product value but still suppressing mis-indexing. However, since σ and χ were not present in the two pattern files examined so far, further testing could not reveal what processing would be suitable for correct indexing of these phases. Further testing was therefore first performed on the next sample, WAAM2.

5.2.2   WAAM2

When moving to the WAAM2 sample, σ-phase and what is believed to be very small grains of χ-phase are observed in the backscatter electron images (e.g. in Figure 4.17a). As potentially both σ and χ were present in the sample, further testing with respect to the AHE n-parameter was performed, where $n = 1 - 5$ and 10 were tested. This gave an overview in how the resulting indexing evolves with increasing n. By studying the phase maps and obtained phase fractions given in Figure 4.20 and Table 4.5, an increasing n-value is favoring indexing of σ and χ-phase as their phase fractions are increasing. For σ the phase fraction reaches an top for $n = 4$. χ is first indexed when using $n = 3$, but has a rapid increase in the indexed phase fraction when moving to $n = 4$ and 5.

When studying the IPF maps in Figure 4.20f and 4.20h from where χ-phase is indexed, mis-indexing seems to occur. The orientation which is getting the best match is typically changing from pixel to pixel withing the χ-indexed phase areas. Further, the χ-phase does not appear where it was expected to be indexed with respect to the BEI in Figure 4.19a. However, the final confirmation of χ mis-indexing is seen in the Figure 4.26, where an experimental pattern indexed as χ for $n = 3$ is presented together with the simulated patterns of best match for γ, σ and χ. As no unique χ-features appear in the pattern, and most of the features present are not found in the simulated χ-pattern but in the simulated γ and σ-patterns, the mis-indexing is confirmed.

When comparing the phase maps in Figure 4.20 to the backscatter electron image of the same region in Figure 4.19a, σ-phase is only indexed for areas where it is expected to be found with respect to the BEI. When studying some of the experimental EBSD patterns to the simulated pattern of best match for σ (shown in Figure 4.23 to 4.25), the indexing of σ is verified to be correct. However, if features of different phases are present in the experimental pattern, σ seems to be less likely in receiving the best match when $n = 1$ is used. When $n = 2$ or 3 is used instead, σ seems to be more favored. In the example shown in Figure 4.25, σ first gets indexed when $n = 3$ is used, when being

indexed as α for $n = 1$ and 2. If the indexing of σ is correct for this example is might more controversial with respect to what the human eye sees. The pattern features of α seems to be more dominating compared to experimental pattern features matching the simulated σ-pattern of best match. However, when studying the IPF maps of $n = 2$ and 3 in Figure 4.20d and 4.20f, the pixels indexed as σ for $n = 3$ but as α or γ for $n = 2$ are all having the same resulting orientation with neighbour σ-indexed pixels. This is not the case when χ-phase is mis-indexed. Mis-indeing of σ was only clearly observed to occur when χ is removed from the dot product file merging and $n > 3$ is used.

To further understand what really happens when different n-values are used for the AHE, the maximum, minimum and mean dot product data for each phase was plotted as a function of the n-value, as seen in Figure 4.21. Here, only the patterns each phase gets the best match for (for the given n-value) are considered. For all four phases these three values increase with increasing n-value, but the growth has a rapid diminish when going from $n = 1$ to $n = 5$. The trend in the obtained data was not as expected, as an increasing n-value seems to be favorable for all four phases. Even the minimum DP-values for α and γ are increasing, despite their phase fractions are decreasing with increasing n-value. However, these values can be considered inaccurate when $n > 2$ as mis-indexed χ-phase is present for areas previously being indexed as α and γ. The mis-indexed pixels could be tracked and thus the actual minimum DP-value for α and γ could be found, as if the mis-indexing never occurred. However, if these experimental patterns consist of features from multiple grains, a reference state had to be used to know which solution that should be used for the given pattern. To choose a reference state would in practice need a conclusion in which n-parameter input was the better. However, such a conclusion could not be made yet.

To examine if the overall lowest dot product value of each phase would better reflect the changes occurring with increasing n-value applied to the AHE, these values were plotted as a function of n for all four phases. The plot is seen in Figure 4.22. The trend in these data seemed to better reflect the trend seen in the indexed phase fraction. For $n = 1$ the value of α and γ are having a slightly higher value than σ and χ. α and γ get a DP-value of 0.755, σ gets 0.754 and χ gets 0.752. However, when moving to $n = 2$, σ has the highest minimum overall DP-value with a value of 0.804. The value of α and γ increases to 0.796, but is now not having the maximum value. At the same time the fraction indexed σ increases while the fractions for α and γ are lowered. Although no pattern is indexed as χ for $n = 2$, based on the DP-value of 0.802 χ gets, it is likely a pattern dominated by EBSD features origin from a χ-grain would be indexed as χ if being present in the pattern file. When moving to $n = 3$ the gap in minimum overall DP-value, between α and γ at the lower end and σ and χ at the upper end, increases further. This matches the change in phase fractions seen. As mis-indexing of χ first appear for $n = 3$, the boost it receives from the pattern processing probably is too large at this stage. For α and γ it seems to be no benefits in increasing n to a value above 3, as

the overall minimum DP-value reaches its peak at this n-value. The peak of σ is reached for $n = 4$, which also is when the indexed phase fraction for σ is at its maximum.

5.2.3   SD750C

For the SD750C sample it was more likely that χ-phase would be indexed. The χ-grains observed had a larger size in this sample compared to the grains observed in WAAM2. When performing further testing with respect to the AHE n-value, only $n = 1, 2$ and 3 were used for this sample as it already was known mis-indexing of χ would appear for $n = 3$. However, it was still not confirmed if using either $n = 1$ or 2 would be successful in indexing χ-patterns as χ. The cropped pattern file from SD750C, containing 100 x 100 patterns, did have two χ-grains present in the phase map from HI, as seen in Figure 4.34. The patterns being associated with the two χ-grains also receive similar plane normal solution in the IPF map from HI. This is not seen for any other regions where multiple χ-indexed patterns are connected to each other. The pattern intensity map and the backscatter electron image, seen in Figure 4.34, both support the indexing of χ for the areas where the two grains are located.

The phase and IPF maps obtained from running DI on the cropped pattern file of SD750C, using $n = 1, 2$ and 3 as input for the AHE n-parameter, were presented in Figure 4.35. The obtained phase fractions were given in Table 4.8. When using $n = 1$, no χ-phase is indexed at all. When moving to $n = 2$, χ is indexed for the two grains previously mentioned and for some few isolated pixels. The fraction of σ is also increasing from 7.52 % to 31.40 %. When moving to $n = 3$, χ is indexed for multiple new locations neither supported by the pattern intensity map nor the BEI. The new χ-indexed regions also appear disordered in the IPF map. χ is therefore assumed to be mis-indexed for these locations. To verify if the two grains seen in the PM for $n = 2$ actually contained features of χ-patterns, the simulated χ-patterns of best match were compared to the experimental patterns of the grains, as seen in Figure 4.41 and 4.42. As seen, these patterns are indexed correct. All or most of the features in the experimental patterns are common to the corresponding simulated χ-patterns. This is seen even clearer in the patterns which are created by averaging multiple patterns from the same grain. However, the more isolated pixels indexed as χ are probably all mis-indexed. An example is shown in Figure 4.43, where the clearest feature of the experimental pattern is not found in the simulated χ-pattern. This indicate mis-indexing of χ may occur when applying $n = 2$ too, but applying $n = 2$ seems to be the only real option for precise dictionary indexing when χ-phase being present. $n = 1$ does not allow indexing of χ, but $n = 3$ leads to a high mis-indexing rate of χ-phase. However, if this applies to when other EBSD parameters are used, e.g. other EBSD pattern acquisition parameters, is not known.

When looking closer to γ and σ, some of the area the phases appear seems to be in common. This is also seen in the backscatter image in Figure 4.34, where σ and γ form a lamellar structure. As σ and ternary γ are formed from α in the eutectoid reaction

given in Equation 3, the coexistence observed is expected [2]. When moving from $n = 1$ to $n = 3$, σ seems to gradually become more favored for the common regions of γ and σ, as seen in the phase maps in Figure 4.35. When studying some pattern examples from where the lamellar structure is observed in the BEI, it is possible to observe features of both γ and σ being present in the experimental patterns, when comparing them to the simulated patterns of best match for the two phases. Two such examples were given in Figure 4.44 and 4.45. As comparison, an experimental pattern of high quality indexed as γ was given in Figure 4.46. This pattern is from a region where the lamellar structure is not observed. Also, when studying the orientation similarity maps given in Figure 4.47, both γ and σ manage to get high near match similarity index η-values for regions where the lamellar structure is observed. α and χ both get poorer η-values for these regions. Although only γ or σ can get indexed for a single pixel, this does not mean the other phase is absent from the interaction volume of the incident beam when acquiring the EBSD patterns.

5.3   The Effect of Dynamic Correction and High-pass Filtering on DI

When testing applied pattern processing recipes, in order to remove mis-indexed χ-phase the adaptive histogram equalization n parameter was early revealed to be the main reason behind the mis-indexing. However, what effect changing the high-pass filtering parameter w or turning off the dynamic background subtraction would have was unknown. It would be an advantage to use a combination of these corrections, which would give the best results in terms of a low mis-indexing, or just a higher mean dot product value.

As recommended values for the high-pass parameter, $w = 0.05 = 1/20$ is stated to be reasonable in the `EMEBDDI`-input scripts for EMsoft DI. However, in Jackson et al. (2019) $w = 0.125 = 1/8$ (together with $n = 5$) is stated to typically result in a high indexing rate for DI [4]. By a mistake, $w = 0.025 = 1/40$ instead of $w = 0.125 = 1/8$ was used for the WAAM1 transition zone, vibration polished surface pattern file in the specialization project [8]. However, as shown in this thesis, this change in w-value has only a minor impact on the end result compared to the impact of changing the n-value.

When running the first re-indexing of the transition zone pattern file, $n = 1$ was applied together with $w = 1/40$. However, two separate indexing runs were performed, where the difference between the parallels were if the dynamic background correction was turned on or off. The resulting phase fractions were presented in Table 4.1 and the EBSD maps in Figure 4.2 to 4.4. The difference in keeping the dynamic background subtraction on or off is marginal when it comes to the obtained phase fractions. The phase and IPF maps also look quite similar, where only some few changes may be seen in the grain boundary regions. The real difference is seen in the CI maps. When the dynamic correction was turned off the obtained DP-values seemed to be highly dependent on the grain orientation, as different grains receive different shades of gray. Some surface defects

visible in the CI maps also appears clearer in the CI map when the dynamic correction is turned off. When the dynamic correction is applied the CI map ends up looking more similar to the IQ map of HI. While there are some local differences in the obtained DP-value within the grains, the average DP-value of each grain appear to have similar values. When the dynamic correction is turned off the grain boundary patterns seems to get similar DP-values as the grain interior patterns. When applying the dynamic correction the DP-value of the grain boundary patterns are not receiving as high DP-values as the grain interior patterns. The grain boundaries therefore appear clearer in the CI map when dynamic correction is applied. As the average DP-value obtained when applying the dynamic correction was the greatest, as shown in Table 4.2, keeping the dynamic correction on is considered the best processing when $w = 1/40$ is used. To study what effect changing the w-value would cause, two additional re-indexing runs using when applying $w = 1/8$ were performed. As seen in Table 4.2, the mean DP-value increases when the dynamic correction is applied, but decreases when not applied. As seen in Figure 2.9, lowering the w-value increases the impact of the high-pass filtering. When already applying dynamic correction, a subsequent high-pass filtering of high correction therefore seems to have a negative effect on the DI. However, when dynamic correction is not applied, the high-pass filtering seems to be more beneficial when using a lower w-value. A w-value lower than the values tested here might be more beneficial to use when not using dynamic correction. However, this was not tested.

A more in-dept testing of the effect changing the applied w-value when also using dynamic background correction was performed on the cropped pattern file of SD750C. Seven w-values were tested, ranging from $w = 1/64$ to $w = 1$ having a factor $1/2$ as step size. As seen in Figure 4.38, the minimum overall dot product data increases for all four phases when the applied w-value is increasing. The gap between σ/χ at the upper end and α/γ at the lower end seems to not differ to much. The exception is for $w = 1$ where the DP-value for χ has increased to a relative high value compared to the three other phases. When studying the phase maps in Figure 4.37 the fraction of mis-indexed χ seems to be higher for the lower w-values. In Table 4.9 the fraction of χ reaches a minimum for $w = 1/8$. Although the overall minimum DP-values for all phases are greater for $w = 1/4$, a slightly better phase balance may occur for $w = 1/8$. As the DI high-pass filtering testing was performed using EMsoft v.4.3 for the cropped pattern file from SD750C, the obtained phase maps of EMsoft v.4.3 for $w = 1/8$ and $w = 1/4$ were compared to the equivalent phase maps of EMsoft v.5.0 (shown in Figure 4.39). Based on the phase maps, EMsoft v.5.0 seems to have a lower fraction mis-indexed χ for both w-inputs. Also, EMsoft v.5.0 seems to have the lowest mis-indexing of χ for $w = 1/8$.

5.4   Results from HI, DI and BEI Compared

Two large pattern files have been indexed using both HI and DI, the pattern file of WAAM2 and SD750C. The comparison between HI and DI for the two pattern files were

presented in section 4.2.4 and 4.3.3. The pattern files differ in how far the transformation of α into σ and γ has progressed for the examined samples.

For the pattern file of WAAM2 both $n = 2$ and $n = 3$ were applied for the DI, as these gave different fractions of σ-phase. Beside the obvious mis-indexing of e.g. χ along grain boundaries, the phase map of HI seems to look more similar to the DI phase map of $n = 3$ than $n = 2$ with respect to the σ-features being present. Several of the σ-phase areas seen in the phase maps for HI and DI ($n = 3$) are missing in the phase map for DI ($n = 2$). As $n = 3$ was used, χ could not be included in the DI as it would cause χ mis-indexing as seen earlier. Since no χ was indexed for $n = 2$, which at this point was known for being a pattern processing leading to correct indexing of EBSD patterns origin from a χ-grain, applying $n = 3$ could therefore be applied in this case to promote the indexing of σ. When running DI for the pattern file from SD750C, it was known from the test indexing runs that χ-phase would be present. Applying $n = 3$ and excluding χ from the indexing was therefore not an option. Only $n = 2$ could be used as input for the AHE-parameter. When comparing the obtained phase maps from HI and DI for the SD750C pattern file, this lack of σ-details seems to be absent for the phase map when using $n = 2$ this time. If $n = 2$ can be used without missing details seen in the phase map of HI, applying $n = 3$ is not necessarily needed. As shown earlier in this thesis, when using different n-values, the phase fraction of indexed σ increases with respect to n as EBSD patterns containing features of multiple phases favors σ over α and γ. When quantifying the fraction of σ in a sample, a safe approach would be to find the highest possible σ-fraction as this is the unwanted phase in the sample. Favoring indexing of σ for samples, where the fraction of σ regardless of pattern processing is low, may therefore be beneficial. The explanation why $n = 3$ had to be used for the WAAM2 sample, but only $n = 2$ for the SD750C sample could be related the to the poorer focus achieved when running the pattern acquisition for WAAM2 compared to SD750C. At least the mis-indexing of e.g. χ along α/γ grain boundaries is not that common in the HI maps from SD750C as for WAAM2. Also, a larger working distance was used for the pattern acquisition of SD750C resulting in a better projection of the pattern onto the detector. As example, the σ-pattern from WAAM2 in Figure 4.23 seems to not have an optimal projection of the pattern center as the pattern features in the lower part of the pattern does not appear as clear as in the upper part. This is not the case for the γ-pattern from SD750C seen in Figure 4.46. The difference in pattern center position on the detector is confirmed by the average y^*-pattern center coordinate calculated from the recorded calibration patterns used by OIM Data Collection. Average $y^* = 72.18\%$ for SD750C, but 75.55% for WAAM2, where the value correspond to the relative y-position on the detector.

When comparing the results of DI to the results of HI, it is clearly seen that DI is successfully in obtaining much better results. The largest differences are seen in the phase and IPF maps from SD750C. While both indexing approaches have no problems

in indexing patterns from α and γ grains, a large difference is seen where the lamellar structure of γ and σ is located. As an example, the phase map of HI contains multiple mis-indexed pixels inside the σ zones, causing a lot of disturbance. In the IPF maps even more disturbance is present as the HI software alternates between various orientations for the same σ grains. This is not the case for DI where the solution is consistent, making it possible to study the grains present inside the lamellar structure. All the mis-indexing gives false phase fraction numbers, as seen in Table 4.10. For α and γ the relative change is not that big. For χ on the other hand there is a 95% decrease in indexed phase fraction when going from HI to DI. Compared to DI, HI is a poor option for phase quantification of heavy transformed duplex steels, when it comes to the quality of the results. The benefits of using DI is on the other side much smaller for a sample where only α and/or γ phases are present. The HI approach is as earlier stated typically multiple times faster to execute than DI, making it convenient to use for qualitative examinations of acquired pattern files, or when the pattern quality always is at a high level.

When comparing the obtained phase maps from DI to the backscatter electron images showing the same regions, the phase maps seems to be missing several details. Examples can be seen in Figure 4.47 where the phase map from DI of the cropped pattern file for SD750C is shown together with its corresponding BEI. The χ-phase formed at the grain boundaries are not seen in the phase map, and the fine lamellar structure of γ and σ appear more coarse. What must be kept in mind when studying and comparing these figures is the differences in the interaction volume for EBSD and backscatter electron imaging. In Fernandez et al. (2016) [52] the lateral, longitudal and depth resolution for EBSD in steel is by Monte Carlo simulations estimated to have the values 20 nm, 75 nm and 16 nm, respectively. However, these values are based on an aperture of 120 μm, when the aperture used for EBSD in this thesis was 300 μm. As larger apertures lead to larger beam cross sections, the lateral and longitudal resolutions are expected to be poorer for this thesis. However, it was assumed an EBSD pattern acquisition step size of 0.1 μm = 100 nm, as applied for this thesis, still would be reasonable to apply without causing to much overlap in the interaction volume of neighbour electron beam incident points, if any at all. The values used for the tilt angle and acceleration voltage in the simulation are the same values used for EBSD in this thesis [52]. For backscatter electron imaging the electron beam is hitting the sample in a 0°angle. The penetration depth the backscatter electrons are escaping the sample from is greater for plane sample than for a tilted sample. For Ag, which has a lower penetration depth than Fe, the backscatter electron penetration depth to capture 90 % of the total backscatter electrons may be estimated to a value of 80 nm. The backscatter image may therefore unveil details which are located at a depth bellow the EBSD depth resolution [53].

5.5   Phase Match Balance Issue for Dictionary Indexing

So far through this thesis the pattern processing recipe for dictionary indexing has been argued for being the problem behind the mis-indexing, occurring in the specialization project [8] as well in this thesis. When all the four phases α, γ, σ and χ are present in the ROI of an EBSD pattern file, only an AHE n-parameter value of 2 seems to work, when applying the pattern processing recipe earlier described. However, when looking closer on some of the obtained dot product data for some of the experimental pattern, it should also be discussed if the EMsoft software itself is contributing to the mis-indexing. When studying the experimental pattern examples related to χ, shown in Figure 4.48, the poorest overall DP for χ of the cropped pattern file from SD750C has a value of 0.800. As the DP-values are normalized from 0 to 1, this should in principle indicate a quite good match was occurring. The experimental pattern on the other hand is of very poor quality, which was expected to result in a much lower DP. The pattern which is both indexed as χ and has the highest match receives a DP of 0.816, which contains multiple features all matching the corresponding simulated pattern. These results indicate that the background of the EBSD patterns is the most important factor when determining the dot product value a dictionary pattern receives when being matched to an experimental pattern. The additional increase in the DP-value for matching features in the experimental pattern seems to play a lesser role. This high match to an experimental pattern containing noise only does not necessary cause complications. Instead of being normalized between 0 and 1, the dot products are now effectively normalized between e.g. 0.800 and 1 instead. When indexing for a single phase only, it is reasonable to assume the dictionary patterns origin from the same master pattern always are well balanced to each other with respect to the minimum overall DP-value. In that case they all would receive the same DP-value to a pattern containing noise only. When indexing for multiple phases, this balance seems not to be preserved. Evidence of this occurring is seen in Figure 4.36. Both for $n = 2$ and $n = 3$ the minimum DP-values for χ and σ are above the values for α and γ. When applying $n = 3$, if e.g. the additional match α gets for matching pattern features in an experimental pattern is not high enough to exceed the minimum dot product match χ receives, the pattern will eventually be indexed as χ, although χ matches the experimental pattern features to a lesser degree. The results from using $n = 2$ for the DI in general seems to indicate the phase match balance is good. However, the pattern example from SD750C in Figure 4.43 shows χ manage to get a better match to this experimental pattern, even though γ and σ matches the pattern feature present better. Some tests were performed, where matching results for the four phases were resulting from different pattern processing recipes. As example, the dot product file merge was performed when the DP-files of α and γ obtained when using $n = 3$ were combined with the DP-file of σ and χ obtained when using $n = 2$. This was tested for the cropped pattern file from SD750C using a [SDH$_{1/8}$AG] pattern processing recipe. Based on Figure 4.36, the gap in the minimum

dot product between the phases would diminish. However, this ended in α and γ being too favored compared to σ and χ. All other tests where DP-files of various pattern processing recipes were combined were not successful in obtaining a better phase match balance.

6   Conclusion

In this thesis multiple SDSS-samples have been studied, where the samples had different contents of secondary phases being present. The main focus was to tune the EBSD pattern processing recipe for DI to prevent mis-indexing from occurring. To verify which pattern processing was the best to use, the results from dictionary indexing was compared to the results from other characterization methods. When the optimal pattern processing recipes for DI was found, the results of HI and DI could finally be compared. From the results and discussion the following conclusions arise:

- EMsoft dictionary indexing (version 5.0) is greatly influenced by a change in the adaptive histogram equalization number of regions parameter, n. With respect to the parameters and equipment used for EBSD in this thesis, setting $n = 2$ is the only viable option when including all four phases α, γ, σ and χ in the dictionary indexing. When χ-phase is absent, $n = 3$ may also be viable in order to favor the indexing of σ-phase.

- When applying both dynamic background subtraction and high-pass filtering to the EBSD patterns prior to dictionary indexing, a high value should be applied for the high-pass w-parameter to reduce the effect of high-pass filtering pattern correction. Applying $w = 1/8$ seems to be reasonable.

- Cr_2N-particles seen in the optical microscopy and backscatter electron images were not detected when being examined with EBSD. As the Cr_2N-particles are of a small size, they are difficult to detect with EBSD.

- When indexing EBSD patterns of low quality for regions where α has gone through phase transformation, forming χ or lammelar γ/σ, the results from HI and DI greatly differ. HI mis-indexing frequently occur for these regions, while the results from DI are having a high quality and reliability.

- For granular α and γ EBSD patterns of high quality the difference in results from HI and DI is low.

- The backscatter electron imaging, EBSD and EPMA characterisation techniques were all capable of detecting χ-grains of large sizes. However, due to differences in the interaction volume the backscatter images were typically showing more finer details than the two other techniques.

7 Further Work

To further improve the Dictionary indexing approach and make it a more frequently applied indexing approach, the following points for further work are suggested:

- Test what effect a neighbor pattern averaging and re-indexing (NPAR) for EBSD patterns would have when indexing pattern files from SDSS-samples containing secondary phases [54].

- Perform more research with respect to DI and the issue of phases not being proper balanced to each other. As example, the effect of changing the EBSD pattern acquisition resolution, speed, exposition time and/or gain could be studied.

- With the release of EMsoft version 5.1, test the updated *EMsoftWorkbench* user interface for Dictionary indexing [55]. A user interface for DI would lower the threshold for new users, give the approach a wider appeal and a more frequently usage.

- Compare the obtained results of DI to results from other characterization techniques, e.g. Transmission Kikuchi Diffraction (TKD) [56].

References

[1] R. W. Revie, editor. *Uhlig's Corrosion Handbook (3rd Edition)*, chapter 52. Duplex Stainless Steels, pages 695 – 706. John Wiley & Sons, 2011.

[2] M. Pohl, O. Storz, and T. Glogowski. Effect of intermetallic precipitations on the properties of duplex stainless steel. *Materials Characterization*, 58(1):65 – 71, 2007.

[3] R. A. Schwarzer, D. P. Field, B. L. Adams, M. Kumar, and A. J. Schwartz. *Electron Backscatter Diffraction in Materials Science*, chapter 1 Present State of Electron Backscatter Diffraction and Prospective Developments, pages 1–20. Springer, 2009.

[4] M. A. Jackson, E. Pascal, and M. De Graef. Dictionary indexing of electron back-scatter diffraction patterns: a hands-on tutorial. *Integrating Materials and Manufacturing Innovation*, 8(2):226–246, Jun 2019.

[5] M. Haukali. EBSD Characterization of the Microstructural Development of σ- and χ-phase in Super Duplex Stainless Steels Subjected to Long Term Heating. Project report in TMT4500, Norwegian University of Science and Technology, 2018.

[6] M. Haukali. In situ EBSD investigation of the nucleation and growth of intermetallic phases in a SDSS. Master's thesis in TMT4905, Department of Materials Science and Engineering, NTNU - Norwegian University of Science and Technology, 2019.

[7] J. Kleppen. Mikrostrukturutvikling i superdupleks rustfritt stål med identifisering av σ-fase ved hjelp av optimalisert bruk av EBSD. Project report in TMT4500, Department of Materials Science and Engineering, NTNU - Norwegian University of Science and Technology, 2017.

[8] V. R. Østerhus. EBSD Characterization of an Additative Manufactured Super Duplex Stainless Steel Sample Using the Hough Indexing and Dictionary Indexing Approaches. Project report in TMT4500, Department of Materials Science and Engineering, NTNU - Norwegian University of Science and Technology, 2019.

[9] S. W. Williams, F. Martina, A. C. Addison, J. Ding, G. Pardal, and P. Colegrove. Wire + arc additive manufacturing. *Materials Science and Technology*, 32(7):641–647, 2016.

[10] G. Posch, K. Chladil, and H. Chladil. Material properties of cmt—metal additive manufactured duplex stainless steel blade-like geometries. *Welding in the World*, 61(5):873–882, Sep 2017.

[11] F. Hejripour, F. Binesh, M. Hebel, and D. K. Aidun. Thermal modeling and characterization of wire arc additive manufactured duplex stainless steel. *Journal of Materials Processing Technology*, 272:58 – 71, 2019.

[12] I. A. Ibrahim, S. A. Mohamat, A. Amir, and A. Ghalib. The effect of gas metal arc welding (gmaw) processes on different welding parameters. *Procedia Engineering*,

41:1502 – 1506, 2012. International Symposium on Robotics and Intelligent Sensors 2012 (IRIS 2012).

[13] K. Yoon-Jun. Phase transformations in cast dupex stainless steels. *Retrospective Theses and Dissertations*, 1175, 2004.

[14] R. W. Revie, editor. *Uhlig's Corrosion Handbook (3rd Edition)*, chapter 51. Austenitic and Ferritic Strainless Steels, pages 657 – 693. John Wiley & Sons, 2011.

[15] K. Migiakis and G. D. Papadimitriou. Effect of nitrogen and nickel on the microstructure and mechanical properties of plasma welded UNS S32760 super-duplex stainless steels. *Journal of Materials Science*, 44(23):6372–6383, Dec 2009.

[16] J. K. Solberg. *Teknologiske metaller og legeringer*. Norwegian university of science and technology, 2014.

[17] International Molybdenum Association. Practical guidelines for the fabrication of duplex stainless steels. Technical report, International Molybdenum Association, 2014.

[18] K. W. Chan and S. C. Tjong. Effect of secondary phase precipitation on the corrosion behavior of duplex stainless steels. *Materials*, 7:5268–5304, 2014.

[19] R. N. Gunn, editor. *Duplex Stainless Steels*. Woodhead Publishing, 1st edition, 1997.

[20] R. Cervo, P. Ferro, and A. Tiziani. Annealing temperature effects on super duplex stainless steel UNS S32750 welded joints. I: microstructure and partitioning of elements. *Journal of Materials Science*, 45(16):4369–4377, Aug 2010.

[21] L. Pezzato, M. Lago, K. Brunelli, M. Breda, and I. Calliari. Effect of the heat treatment on the corrosion resistance of duplex stainless steels. *Journal of Materials Engineering and Performance*, 27:1–10, 06 2018.

[22] I. Zucato, M. C. Moreira, I. F. Machado, and S. M. G. Lebrão. Microstructural characterization and the effect of phase transformations on toughness of the UNS S31803 duplex stainless steel aged treated at 850 °C. *Materials Research*, 5(3):385–389, 2002.

[23] N. Llorca-Isern, H. López-Luque, I. López-Jiménez, and M. V. Biezma. Identification of sigma and chi phases in duplex stainless steels. *Materials Characterization*, 112:20 – 29, 2016.

[24] D. M. Escriba, E. Materna-Morris, R. L. Plaut, and A. F. Padilha. Chi-phase precipitation in a duplex stainless steel. *Materials Characterization*, 60(11):1214 – 1219, 2009.

[25] J. S. Kasper. The ordering of atoms in the chi-phase of the iron-chromium-molybdenum system. *Acta Metallurgica*, 2(3):456 – 461, 1954.

[26] J. Kleppen. Mikrostrukturutvikling i superdupleks rustfritt stål og effekten av prøvepreparering på identifisering og kvantifisering av sigmafase gjennom EBSD-karakterisering. Master's thesis in TMT4905, Department of Materials Science and Engineering, NTNU - Norwegian University of Science and Technology, 2018.

[27] N. Pettersson, R. F. A. Pettersson, and S. Wessman. Precipitation of Chromium Nitrides in the Super Duplex Stainless Steel 2507. *Metallurgical and Materials Transactions A*, 46:1062–1072, January 2015.

[28] A. J. Ramirez, J. C. Lippold, and S. D. Brandi. The Relationship between Chromium Nitride and Secondary Austenite Precipitation in Duplex Stainless Steels. *Metallurgical and Materials Transactions A*, 34:1575–1597, 2003.

[29] T.-H. Lee, S.-J. Kim, and S. Shin, E. Takaki. On the crystal structure of Cr_2N precipitates in high-nitrogen austenitic stainless steel. *Acta Crystallographica Section B*, 61:137–144, 2005.

[30] S. Hereñú, M. G. Moscato, I. Alvarez, and A. F. Armas. The Influence of Chromium Nitrides Precipitation on the Fatigue Behavior of Duplex Stainless Steels. *Procedia Engineering*, 74:179 – 182, 2014. XVII International Colloquium on Mechanical Fatigue of Metals (ICMFM17).

[31] J. Hjelen. *Scanning elektron-mikroskopi*. SINTEF, Avdeling for metallurgi og Metallurgisk institutt, NTH, 1986.

[32] R. Reichelt. *Science of Microscopy*, volume I, chapter 3. Scanning Electron Microscopy, pages 133–272. Springer, 2008.

[33] A. Winkelmann, C. Trager-Cowan, F. Sweeney, A. P. Day, and P. Parbrook. Many-beam dynamical simulation of electron backscatter diffraction patterns. *Ultramicroscopy*, 107(4):414 – 421, 2007.

[34] S. Zaefferer, N.-N. Elhami, and P. Konijnenberg. *Phase Transformations in Steels: Diffusionless Transformations, High Strength Steels, Modelling and Advanced Analytical Techniques*, chapter 18 Electron backscatter diffraction (EBSD) techniques for studying phase transformations in steels, pages 557–560. Elsevier Science & Technology, 2012.

[35] F. Brisset. Electron backscatter diffraction basics and applications. 2010.

[36] Y.-H. Chen, S. U. Park, D. Wei, G. Newstadt, M. Jackson, J. P. Simmons, M. De Graef, and A. O. Hero. A Dictionary Approach to Electron Backscatter Diffraction Indexing. *Microscopy and Microanalysis*, 21(3):739–752, 2015.

[37] M. De Graef. EMsoft. https://github.com/EMsoft-org/EMsoft/wiki, Last edited: 09.03.2019, accessed at internet: 06.12.2019.

[38] M. De Graef. Public EMsoft repository. https://github.com/EMsoft-org/EMsoft, accessed at internet: 06.12.2019.

[39] M. De Graef. EMsoft. http://vbff.materials.cmu.edu/EMsoft/, accessed at internet: 06.12.2019.

[40] K. Marquardt, M. De Graef, S. Singh, H. Marquardt, A. Rosenthal, and S. Koizuimi. Quantitative electron backscatter diffraction (EBSD) data analyses using the dictionary indexing (DI) approach: Overcoming indexing difficulties on geological materials. *American Mineralogist*, 102:1843–1855, 2017.

[41] D. J. Dingley, S. I. Wright, and M. M. Nowell. Dynamic Background Correction of Electron Backscatter Diffraction Patterns. *Microscopy and Microanalysis*, 11(502):528–529, 2005.

[42] T. Tanaka and A. Wilkinson. Pattern Matching Analysis of Electron Backscatter Diffraction Patterns for Pattern Centre, Crystal Orientation and Absolute Elastic Strain Determination – accuracy and precision assessment. *Ultramicroscopy*, 202:87–99, 2019.

[43] A. Winkelmann. Basics of Kikuchi Pattern Processing. https://xcdskd. readthedocs.io/en/latest/pattern_processing/kikuchi_pattern_processing.html, 2018. Accessed at internett: 09.04.2020.

[44] E. D. Pisano, S. Zong, B. M. Hemminger, M. DeLuca, R. E. Johnstton, K. Muller, M. P. Braeuning, and S. M. Pizer. Contrast Limited Adaptive Histogram Equalization image processing to improve the detection of simulated spiculations in dense mammograms. *Journal of Digital Imaging*, 11(193), 1998.

[45] A. M. Reza. Realization of the Contrast Limited Adaptive Histogram Equalization (CLAHE) for Real-Time Image Enhancement. *Journal of VLSI signal processing systems for signal, image and video technology*, 38:35–44, 2004.

[46] R. W. G. Wyckoff. *Crystal Structures*, volume 1. Interscience Punlishers, 2 edition, 1963.

[47] E. J. Kramer, P. Haasen, and R. W. Cahn, editors. *Materials science and technology: a comprehensive treatment*, volume 1: Structure of solids. Wiley-VCH, 2005.

[48] H. L. Yakel. Atom distributions in sigma phases. I. Fe and Cr atom distributions in a binary sigma phase equilibrated at 1063, 1013 and 923 K. *Acta Crystallographica Section B*, 39(1):20–28, 1983.

[49] H. W. Ånes and T. Bergh. KikuchiPy.

https://zenodo.org/record/3842021/export/hx#.Xt4HKxZS92U, accessed at internet: 30.03.2020.

[50] S. M. Pizer, E. P. Amburn, J. D. Austin, R. Cromartie, A. Geselowitz, T. Greer, B. T. H. Romeny, J. B. Zimmerman, and K. Zuiderveld. Adaptive histogram equalization and its variations. *Computer Vision, Graphics, and Image Processing*, 39(3):355–368, 1987.

[51] J. Tjemsland, H. W. Ånes, A. Krogen, and J. A. Støvneng. Image Filtering using Discrete Fourier Transform.
https://nbviewer.jupyter.org/urls/www.numfys.net/media/notebooks
/image_filtering_using_fourier_transform.ipynb#Filtering, Last edited: 22.03.2018, accessed at internet: 13.06.2020.

[52] S. F. Bordín, S. Limandri, J. M. Ranalli, and G. Castellano. EBSD spatial resolution for detecting sigma phase in steels. *Ultramicroscopy*, 171, 2016.

[53] J. Goldstein, D. E. Newbury, J. R. Michael, N. W. M. Ritchie, J. H. J. Scott, and D. C. Joy. *Scanning Electron Microscopy and X-Ray Microanalysis*, chapter 1 and 2, pages 1 – 28. Springer Nature, 2018.

[54] S. I. Wright, M. M. Nowell, S. P. Lindeman, P. P. Camus, M. De Graef, and M. A. Jackson. Introduction and comparison of new EBSD post-processing methodologies. *Ultramicroscopy*, 159:81–94, 2015.

[55] M. De Graef. EMsoft - What's coming in 5.1? https://github.com/EMsoft-org/EMsoft#whats-coming-in-51, accessed at internet: 11.06.2020.

[56] G. C. Sneddon, P. W. Trimby, and J. M. Cairney. Transmission Kikuchi diffraction in a scanning electron microscope: A review. *Material Science and Engineering R*, 110:1–12, 2016.

A Performing Dictionary Indexing Using EMsoft

In this section, a description in how the indexing of the EBSPs in EMsoft was executed, is given. The description may be used as a beginner guide for EMsoft as well. On the pages where the scripts are given, the changed entry values are marked with red or blue color boxes. For running EMsoft, Jackson et al. (2019) [4] was used as the guide, and contains more details than covered here. For more information or guidelines, the official EMsoft webpage can be used:

http://vbff.materials.cmu.edu/emsoft/

The EMlab at NTNU also has some information on the use of EMsoft, where more information and guidelines can be found:

https://www.ntnu.no/wiki/display/imtlab/EMsoft

This guide was written when EMsoft 5.0 was the newest available version, but still in development. The guide covers both version 4.3 and 5.0 of EMsoft, which both were used when writing this master thesis. Since EMsoft is in continuous development, some of the steps here may change for newer versions. Some of the steps can also be quite time consuming to run and may require a big portion of the computer's capacity (CPU, GPU and/or RAM) in order to run withing reasonable time. In case any of the Namelist template files are missing in the downloaded version of EMsoft, they can also be found online at EMsoft's GitHub web page:

https://github.com/EMsoft-org/EMsoft/tree/develop/NamelistTemplates

A.1 Generating Crystal Structure File

The first step needed in running an EMsoft indexing is generating crystal structure files (`.xtal` files) for all phases which are going to be indexed. This step is only necessary to run if no `.xtal` files are available for the phases which are going to be indexed.

- In Visual Studio Code enter the directory where you want to save your xtal files which are going to be generated
  (e.g. `PS C:\Users\Ola\Documents\EMsoft\EMdata\Crystal_data\ferrite`.)

- Run the command line `EMmkxtal` to call the EMmkxtal program, which is used to generate the `.xtal file`. The program will ask for the following inputs:

  - Crystal system: A list of the available crystal systems appear. Select the number assigned to the correct crystal system of the phase (e.g. select `1` (cubic) for ferrite since ferrite has BCC crystal structure) [16].

  - Lattice parameters: enter the a, b, and c lattice parameters in the unit of nm. If some of them are equal to each other, you only have to enter the values of a and c, or a only.

  - Space group: A list of available space groups appear with an assigned number.

Select the number assigned to the correct space group of the phase (e.g. select `229` (Im-3m) for ferrite.)

– Atomic number: select an atomic number of an element present in the phase.

– Give the selected element one of its asymmetric atom positions. The site occupation parameter f and the Debye-Waller factor B_{iso} in the unit of nm^2 for this element in this position must also be given. The values must be typed as a string with the format: X,Y,Z,f,B_{iso} (e.g. `0,0,0,1.0,0.005`).

– Repeat the two previous steps until all relevant elements present in the phase are included in all lattice positions they occupy.

– Output file name: e.g. `ferrite.xtal` for ferrite.

– Source: enter the reference of the data. Use single quotes around the string (e.g 'Pearson's Handbook; Peng et al. 1996').

A.2   Monte Carlo BSE Simulation

The next step is to create an HDF5 file that contains the energy, depth and directional histograms of the BSEs used in the EBSD Master Pattern Simulation (see section A.3).

- Create a file for the Monte Carlo simulation:

  – Enter the directory where you want to create the file
  (e.g. `PS C:\Users\Ola\Documents\EMsoft\EMdata\Crystal_data\ferrite`).

  – Create the file by entering the command `EMMCOpenCL -t`. The created file will by default be called `EMMCOpenCL.template`.

  – Rename the file and change the file name ending from `.template` to `.nml` (e.g. `emmcopencl_ferrite.nml`). On Windows this can be done by right-clicking the file and rename it.

- Open the Monte Carlo simulation file in Visual Studio Code and fill in the file names and parameters so they match the parameters used in the EBSD pattern acquisition. See the next page for entries that are relevant to change. Entries which must be changed are all marked in red. Remember to save the file before continuing with the next step.

- Start the Monte Carlo simulation by running the command
  `EMMCOpenCL path_to_nml_file\myEMMCOpenCL.nml`
  (e.g. `EMMCOpenCL C:\Users\Ola\Documents\EMsoft\EMdata\Crystal_data\ferrite\emmcopencl_ferrite.nml`).

Monte Carlo BSE Simulation Script

```
&MCCLdata
!  only bse1, full or Ivol simulation
mode = 'full' !  'bse1' or 'full', 'Ivol',
!  name of the crystal structure file
xtalname = 'ferrite/ferrite.xtal',
!  for full mode:  sample tilt angle from horizontal [degrees]
sig = 70.0,
!  for bse1 mode:  start angle
sigstart = 0.0,
!  for bse1 mode:  end angle
sigend = 30.0,
!  for bse1 mode:  sig step size
sigstep = 2.0,
!  sample tilt angle around RD axis [degrees]
omega = 0.0,
!  number of pixels along x-direction of square projection
   [odd number!]
numsx = 501,
!  number of incident electrons per thread
num_el = 10,
!  GPU platform ID selector
platid = 1,
!  GPU device ID selector
devid = 1,
!  number of work items (depends on GPU card; leave unchanged)
globalworkgrpsz = 150,
!  total number of incident electrons and multiplier (to get more than
   2^(31)-1 electrons)
totnum_el = 2000000000,
multiplier = 1,
!  incident beam energy [keV]
EkeV = 20.D0,
!  minimum energy to consider [keV]
Ehistmin = 10.D0,
!  energy binsize [keV]
Ebinsize = 1.0D0,
!  maximum depth to consider for exit depth statistics [nm]
depthmax = 100.D0,
!  depth step size [nm]
```

```
depthstep = 1.0D0,
!  should the user be notified by email or Slack that the program has
   completed its run?
Notify = 'Off',
!  output data file name; pathname is relative to the EMdatapathname
   path !!!
dataname = 'Crystal_data/ferrite/ferrite_mc_mp_20kv.h5'
/
```

A.3   EBSD Master Pattern Simulation

By running the EBSD master pattern simulation, a master pattern will be stored both as square Lambert projections and stereograpic projections in a new group in the original HDF5 file generated by the EMMCOpenCL program in the previous step.

- Enter the directory where you want to create the master pattern simulation parameter file
  (e.g. EMMCOpenCL C:\Users\Ola\Documents\EMsoft\EMdata\
  Crystal_data\ferrite).

- Create the parameter file by the command "EMEBSDmaster -t". The two files which by default are called "EMEBSDmaster.template" and "BetheParameters.template" are created.

- Rename and change the file name ending from ".template" to ".nml"
  (e.g. ebsdmaster_ferrite.nml).

- Open the master pattern parameter file in Visual Studio Code and change the relevant parameters. Input examples are given on the next page. The parameters to change are marked with red, and the parameter which should be changed is marked with blue. This includes the "energyfile" location (red) which is the Monte Carlo h5-file generated in last step and the "nthreads" (blue). The number of threads, "nthreads" parameter, should be set to the number of cores available in your system. It is possible to look up how many cores a Windows computer has by opening the Task Manager and selecting the Performance tab.

- Run the EBSD Master Pattern simulation by calling on the "EMEBSDmaster" program with the EBSD master pattern parameter file as input (e.g. EMEBSDmaster ebsdmaster_ferrite.nml).

EBSD Master Pattern Simulation Script

```
&EBSDmastervars
!  smallest d-spacing to take into account [nm]
dmin = 0.05,
!  number of pixels along x-direction of the square master pattern
   (2*npx+1 = total number)
npx = 500,
!  lattitudinal grid type:  'Lambert' or 'Legendre'
latgridtype = 'Lambert',
!  name of EMMCOpenCL output file to be used to copy the MC data from
   for this master pattern run;
!  This can be used to perform multiple master pattern runs starting
   from the same MC data set without
!  having to rerun the MC computation.  Leave this variable set to
   'undefined' if not needed.
copyfromenergyfile = 'undefined',
!  name of the energy statistics file produced by EMMCOpenCL program;
   relative to EMdatapathname;
!  this file will also contain the output data of the master program
energyfile = 'Crystal_data/ferrite/ferrite_mc_mp_20kv.h5',
!  number of OpenMP threads
nthreads = 4,
!  do you wish to receive a notification (Email or Slack) when the
   program completes ?
Notify = 'Off',
!  restart computation ?
restart = .FALSE.,
!  create output file with uniform master patterns set to 1.0
   (used to study background only)
uniform = .FALSE.,
/
```

A.4 Preparation of Experimental EBSD Pattern File for Indexing

When performing static and dynamic background subtraction prior to EMsoft indexing, the open-source Python library *KikuchiPy* is used. As this guideline is written, KikuchiPy v.0.2 is the newest version available and this guide may therefore apply to later versions. For information about installation of KikuchiPy or more in-dept guidelines, visit KikuchiPy's homepage: https://kikuchipy.org/en/stable/

In Anaconda Navigator (Anaconda3) launch JupyterLab in an environment having KikuchiPy installed. Once JuyterLab is opening, open a new Python launcher. First, run the command

```python
%matplotlib qt5
import kikuchipy as kp
```

which is used for the setup. Next, load the experimental EBSD pattern file into python with the command

```python
s = kp.load(" path_to_experimental_patterns ")
```

where the patterens will be stored in the variable `s`. Run the static background subtraction with the command

```python
s.remove_static_background(operation='subtract', relative=True)
```

Dynamic background subtraction is is performed with the command

```python
s.remove_dynamic_background(operation='subtract')
```

Store the corrected pattern file with the command below. EMsoft version 4.3 does not accept the NORDIF ".dat" pattern file type and the file should therefore be saved as the ".h5" file format. EMsoft version 5.0 accepts both ".dat" and ".h5" files.

```python
s.save(" path_to_saving_location / name_of_the_static_background
_corrected_pattern_file . file_format ").
```

In Python more options are also available. It is possible to plot the pattern file before or after the pattern correction(s) with the command

```python
s.plot()
```

A pattern intensity map as well as the pattern for the currently viewed pixel are opened in two new separate windows.

A.5   Dictionary Indexing

For dictionary indexing, every phase is indexed in a separate step. First enter the directory where you want to store the indexing "EBSDDI.nml" setup file (e.g. PS C:\Users\Ola\Documents\EMsoft\EMdata\patterns\SDSS_sample\emsoft \ferrite). Run the command "EMEBSDDI -t" to create a new setup file for indexing. Rename the created "EMEBSDDI.template" file to something suitable, and change the name ending to ".nml" (e.g. ebsddi_ferrite.nml). Create a ebsddi.nml-file for every phase to be indexed. On the next page an example of the setup of the ebsddi.nml-file is shown. Parameters which must be changed are marked in red and parameters which may be changed are marked in blue.

Dictionary Indexing Script

```
&EBSDIndexingdata
!  The line above must not be changed
!
!  The values below are the default values for this program
!
!#####################################################################
!  INDEXING MODE
!#####################################################################
!
!  'dynamic' for on the fly indexing or 'static' for pre calculated
   dictionary
indexingmode = 'dynamic',
!
!#####################################################################
!  DICTIONARY PARAMETERS: COMMON TO 'STATIC' AND 'DYNAMIC'
!#####################################################################
!
!  do you want Email or Slack notification when the run has completed?
Notify = 'Off',
!  width of data set in pattern input file
ipf_wd = 186,
!  height of data set in pattern input file
ipf_ht = 139,
!  define the region of interest as x0 y0 w h; leave all at 0 for full
   field of view
!  region of interest has the point (x0,y0) as its upper left corner
```

```
    and is w x h patterns
ROI = 0 0 0 0,
!  X and Y sampling step sizes
stepX = 0.1,
stepY = 0.1,
!  number of top matches to keep from the dot product results nnk = 50,
!  the following option has been disabled starting version 4.3
!  number of top matches to use for orientation averaging (<nnk)
!  nnav = 20,
!  number of top matches to use for Orientation Similarity Map
   computation (<nnk)
nosm = 20,
!  number of top matches to use for Indexing Success Map computation
   (<nnk)
nism = 5,
!  Indexing Success threshold angle (degrees)
isangle = 1.5,
!  to use a custom mask, enter the mask filename here; leave undefined
   for standard mask option
maskfile = 'undefined',
!  mask or not
maskpattern = 'n',
!  mask radius (in pixels, AFTER application of the binning operation)
maskradius = 240,
!  hi pass filter w parameter; 0.05 is a reasonable value
hipassw = 0.125,
!  number of regions for adaptive histogram equalization
nregions = 2,


!####################################################################
!  ONLY SPECIFY WHEN INDEXINGMODE IS 'DYNAMIC'
!####################################################################
!
!  number of cubochoric points to generate list of orientations
ncubochoric = 100,
!  distance between scintillator and illumination point [microns]
L = 4692.24,
!  tilt angle of the camera (positive below horizontal, [degrees])
thetac = 0,
!  CCD pixel size on the scintillator surface [microns]
delta = 70.0,
```

```
!  number of CCD pixels along x and y
numsx = 120,
numsy = 120,
!  pattern center coordinates in units of pixels
xpc = -0.0672,
ypc = 28.8408,
!  angle between normal of sample and detector
omega = 0.0,
!  minimum and maximum energy to use for interpolation [keV]
energymin = 10.0,
energymax = 20.0,
!  the following option has been disabled starting version 4.3
!  spatial averaging method ('y' or 'n' ;can't be used with
   approximate energy average)
!  spatialaverage = 'n',
!  incident beam current [nA]
beamcurrent = 150.0,
!  beam dwell time [micro s]
dwelltime = 100.0,
!  binning mode (1, 2, 4, or 8)
binning = 1,
!  intensity scaling mode 'not' = no scaling, 'lin' = linear,
    'gam' = gamma correction
scalingmode = 'gam',
!  gamma correction factor
gammavalue = 0.33,
!
!##################################################################
!  INPUT FILE PARAMETERS: COMMON TO 'STATIC' AND 'DYNAMIC'
!##################################################################
!
!  name of datafile where the patterns are stored; path relative to
   EMdatapathname
exptfile = 'patterns/SDSS_sample/Pattern_static_corrected.h5',
!  input file type parameter:  Binary, EMEBSD, TSLHDF, TSLup2,
   OxfordHDF, OxfordBinary, BrukerHDF, NORDIF
inputtype = 'EMEBSD',
!  here we enter the HDF group names and data set names as individual
   strings (up to 10)
!  enter the full path of a data set in individual
   strings for each group, in the correct order,
```

```
!  and with the data set name as the last name; leave the remaining
   strings empty (they should all
!  be empty for the Binary and TSLup2 formats)
HDFstrings = 'Scan 1' 'EBSD' 'Data' 'patterns' '' '' '' '' '' '',
!
!########################################################################
!  OTHER FILE PARAMETERS: COMMON TO 'STATIC' AND 'DYNAMIC'
!########################################################################
!
!  temporary data storage file name ; will be stored in
   $HOME/.config/EMsoft/tmp
tmpfile = 'EMEBSDDict_tmp.data',
keeptmpfile = 'n',
!  output file ; path relative to EMdatapathname
datafile = 'patterns/SDSS_sample/emsoft/ferrite/dp_ferrite.h5',
!  ctf output file ; path relative to EMdatapathname
ctffile = 'undefined',
!  the following option has been disabled starting version 4.3
!  average ctf output file ; path relative to EMdatapathname
!  avctffile = 'undefined',
!  ang output file ; path relative to EMdatapathname
angfile = 'patterns/SDSS_sample/emsoft/ferrite/dp_ferrite.ang',
!  euler angle input file
eulerfile = 'undefined'
!########################################################################
!  ONLY IF INDEXINGMODE IS STATIC
!########################################################################
!
dictfile = 'undefined',
!
!########################################################################
!  ONLY IF INDEXINGMODE IS DYNAMIC
!########################################################################
!
!  master pattern input file; path relative to EMdatapathname
masterfile = 'Crystal_data/ferrite/ferrite_mc_mp_20kv.h5',
!
!########################################################################
!  IF REFINEMENT IS NEEDED ...
!########################################################################
!
```

```
!  enter the name of the nml file for the EMFitOrientation program
refinementNMLfile = 'undefined',
!
!#####################################################################
!  SYSTEM PARAMETERS: COMMON TO 'STATIC' AND 'DYNAMIC'
!#####################################################################
!
!  number of dictionary files arranged in column for dot product on
   GPU (multiples of 16 perform better)
numdictsingle = 192,
!  number of experimental files arranged in column for dot product on
   GPU (multiples of 16 perform better)
numexptsingle = 192,
!  number of threads for parallel execution
nthreads = 4,
!  platform ID for OpenCL portion of program
platid = 1,
!  if you are running EMEBSDDI, EMECPDI, EMTKDDI, then define the
   device you wish to use
devid = 1,
!  if you are running EMEBSDDImem on multiple GPUs, enter their
   device ids (up to eight) here; leave others at zero
multidevid = 0 0 0 0 0 0 0 0,
!  how many GPU devices do you want to use?
usenumd = 1,
/
```

The parameters highlighted in red are further explained here. More information can be found in Jacson et al. (2019) [4].

- `ipf_wd` and `ipf_ht` are the width and height in pixels of the dataset obtained when running EBSD on the chosen area. The height and width can be found in the Setting.txt file generated when running EBSD with the NORDIF software (on Zeiss Ultra at the EMlab of the Material science department, NTNU). Under "[Area]" in the "Number of samples" slot `ipf_ht` and `ipf_wd` are given as "(ipf_ht)x(ipf_wd) #"

- `stepX` and `stepY` are the sampling step sizes used for the EBSD run. When using the NORDIF software on Zeiss Ultra, these are always equal to each other. In case there should be any doubt about what step size which has been used, this can also be found in the "Setting.txt" file.

- `thetac`, the tilt angle of the camera is equal to 0 for the detector at the Zeiss Ultra previous mentioned.

- `delta`, δ is the detector's pixel size. $\delta = 70$ μm for the UF1100 (UltraFast (1100 fps) detector connected to the Zeiss Ultra previous mentioned.

- `numsx`, N_x^s and `numsy`, N_y^s are the number of pixels on the detector along the x and y direction. The value of `numsx` and `numsy` equals the resolution selected for the acquisition settings for the EBSD run. The resolution can be checked in the "Setting.txt" file from the NORDIF software, and `numsx` and `numsy` always have the same value for Zeiss Ultra's detector.

- `L` is the distance between the detector's scintillator and the illumination points on the sample in μm, and `xpc` and `ypc` are the pattern center coordinates in units of pixels on the detector. In order to calculate these, x*, y* and z* must first be retrieved from the EDAX TSL OIM software. `L`, `xpc` and `ypc` are calculated for each calibration pattern collected before the EBSD run (typically 5), which all have unique x*, y* and z* values. The average value of `L`, `xpc` and `ypc` for the calibration patterns are in the end calculated and used as the `L`, `xpc` and `ypc` given to EMsoft. The formulas for calculating `L`, `xpc` and `ypc` are given below. Note the difference in calculating `xpc` for EMsoft version 4.3 and version 5.0.

$$
\begin{aligned}
x_{pc} &= N_x^s(x^* - 1/2); && \text{(for EMsoft version 4.3)} \\
x_{pc} &= -N_x^s(x^* - 1/2); && \text{(for EMsoft version 5.0)} \\
y_{pc} &= N_x^s y^* - N_y^s/2; && \\
L &= N_x^s \delta z^*.
\end{aligned}
\tag{9}
$$

- In `exptfile` insert the path to the experimental pattern file to be indexed. In `inputtype` the input file type parameter which corresponds to the `exptfile` must

XII

be selected. For ".h5" files select `'EMEBSD'`, for ".dat" files select `'NORDIF'`.

- In `HDFstrings` the path to "patterns" for files stored in the ".h5" file type must be given. The path can be found by opening the experimental file with the HDFview software. For HDFview version 3.1.0 the path will by default be equal to the example above.

- In `datafile` insert the the path to where the dot product file from the indexing is going to be stored, as well as the name of the file. The file name ending must be a valid HDF5-file ending, e.g. ".h5". This file is used for further processing of the data from the indexing. The dot product file can also be opened in HDFview to study the average dot product map (ADP) and image quality (IQ) map for the experimental patterns. A confidence index (CI) map and an orientation similarity map (OSM), which both are unique for the indexed phase are also available here.

- In `angfile` insert the the path to where the ".ang" file from the indexing is going to be stored, as well as the name of the file. This file can be directly opened with the TSL OIM Analysis software to view the result for the single indexed phase. However, it may be desirable to run the Orientation Refinement step for a better end-result. When indexing for multiple phases, the Dot Product Merge step must also be executed.

- In `masterfile` the path to the master pattern file, for the phase to be indexed, must be defined.

A.6   Orientation Refinement

By running the orientation refinement step a more accurate orientation for each pixel may be achieved. To run the orientation refinement, a template file must first be created. In the directory where you want to create the file, run the command "EMFitOrientation -t" to create an orientation refinement file. Rename the file to something suitable and change the file type to ".nml" (e.g. FitOrientation_ferrite.nml"). The orientation refinement is run with the command "EMFitOrientation FitOrientation_ferrite.nml". Below an example of the setup of the script is shown. The parameters which must be changed are marked in red and the parameters which may be changed are marked in blue. In `dotproductfile` must the path to and the name of the dot product file to be refined be specified. The refinement program also demands the user to create a ctf file and temporarly data file, so `ctffile` and `tmpfile` need an input. More information about how this step works can be found in Jacson et al. (2019) [4].

Orientation Refinement Script

```
&RefineOrientations
!  number of parallel threads to use for refinement run
nthreads = 4,
!  name of input dot product HDF5 file
dotproductfile = 'patterns/SDSS_sample/emsoft/ferrite/dp_ferrite.h5',
!  name of ctf output file for refined orientations
ctffile = 'patterns/SDSS_sample/emsoft/ferrite/refined_ferrite.nml',
!  name of temporary file for pre-processed patterns
!  (will override the temporary file name defined in the dot product
   file)
tmpfile = 'EMEBSDDict_tmp.data',
!  modality ('EBSD' or 'ECP')
modality = 'EBSD',
!  keep the pre-processed patterns all in memory?
inRAM = .FALSE.,
!  how many items from the top matches list do you want to check for the
   refinement?
matchdepth = 1,
!  refinement method:
!  'SUB' : refinement by hierarchical sub-sampling of cubic grid in
   cubochoric space
!  'FIT' : fit by "bound optimization by quadratic approximation"
   (BOBYQA) in homochoric space (generally faster than SUB)
```

```
method = 'FIT',
!  ===================================
!  if method == 'SUB'
! number of hierarchical iterations
niter = 1,
!  number of points sampled around given point [(2*nmis+1)^3]
nmis = 1,
!  ===================================
!  if method == 'FIT'
! max step size to take in homochoric space during the refinement
step = 0.03,
!  In FIT mode, this program can also include pseudo-symmetric variants
   in the list of starting orientations to refine.
!  Pseudo-symmetric variant Euler triplets or axis-angle pair(s) are
   stored in the PSvariantfile.
!  format:  first line 'ax', second line number of axis-angle pairs,
   then one pair per line (unit vector, angle last in degrees)
!  or format:  first line 'eu', second line number of Euler triplets,
   then one triplet per line (in degrees)
PSvariantfile = 'undefined',
!  ===================================
/
```

A.7   Dot Product File Merge

The final step in a multi-phase indexing is the dot product file merging. A template for the script is created with the command "EMdpmerge -t", and the name should as usual be changed (e.g. dp_merge.nml). The script is run with the command "EMdpmerge dp_merge.nml". In the example below the parameters which must be changed are marked in red. In `usedp`, `'original'` is selected if the original dot product data is used, or `'refined'` if the refined dot product data is used. The obtained ".ang" file is equivalent to the ".osc" file obtained when indexing with TSL OIM. ".ang" files can be read by TSL OIM Analysis in order to view the various maps available from indexed EBSP data.

Dot Product File Merge Script

```
&dpmerge
!  The line above must not be changed
!
!  The values below are the default values for this program
!
!  two to five dot product file names to be merged
   [relative to EMdatapathname]
dotproductfile = 'patterns/SDSS_sample/emsoft/ferrite/dp_ferrite.h5'
    'patterns/SDSS_sample/emsoft/austenite/dp_austenite.h5' '' '' '',
!  name of color file for phase map; accepts .tiff or .bmp extension
!  the color will be scaled in intensity by the value of the maximum
   dot product
phasemapname = 'patterns/SDSS_sample/emsoft/dpmerge_refined.tiff',
!  the available colors are 1:red, 2:green, 3:blue, 4:yellow, 5:cyan,
   6:fushia, and 7:white
!  define the color for each phase (up to 5) by entering the numbers
   (leave 0 if not used)
phasecolors = 1 2 0 0 0,
!  output .ctf file name
ctfname = 'undefined',
!  output .ang file name
angname = 'patterns/SDSS_sample/emsoft/dpmerge_refined.ang',
!  dot products to use:  'original' or 'refined'
usedp = 'refined',
!  indxing mode:  'DI' or 'SI'
indexingmode = 'DI',
/
```

XVI